SANDIA REPORT
SAND2009-8037
Unlimited Release
Printed February 2010

Sweep-Twist Adaptive Rotor Blade: Final Project Report

Knight & Carver Wind Group
2423 Hoover Avenue
National City, CA 91950

Technical Manager, Tom Ashwill
Sandia National Laboratories
P.O. Box 5800
Albuquerque, NM 87123

Prepared by
Sandia National Laboratories
Albuquerque, New Mexico 87185 and Livermore, California 94550

Sandia is a multiprogram laboratory operated by Sandia Corporation,
a Lockheed Martin Company, for the United States Department of Energy's
National Nuclear Security Administration under Contract DE-AC04-94AL85000.

Issued by Sandia National Laboratories, operated for the United States Department of Energy by Sandia Corporation.

Available to DOE and DOE contractors from

U.S. Department of Energy
Office of Scientific and Technical Information
P.O. Box 62
Oak Ridge, TN 37831

Telephone: (865) 576-8401
Facsimile: (865) 576-5728
E-Mail: reports@adonis.osti.gov
Online ordering: http://www.osti.gov/bridge

Available to the public from

U.S. Department of Commerce
National Technical Information Service
5285 Port Royal Rd.
Springfield, VA 22161

Telephone: (800) 553-6847
Facsimile: (703) 605-6900
E-Mail: orders@ntis.fedworld.gov
Online order: http://www.ntis.gov/help/ordermethods.asp?loc=7-4-0#online

SAND2009-8037
Unlimited Release
Printed February 2010

SWEEP-TWIST ADAPTIVE ROTOR BLADE:

FINAL PROJECT REPORT

Knight & Carver Wind Group
2423 Hoover Avenue
National City, CA 91950

Sandia Technical Manager: Tom Ashwill

ABSTRACT

Knight & Carver was contracted by Sandia National Laboratories to develop a Sweep Twist Adaptive Rotor (STAR) blade that reduced operating loads, thereby allowing a larger, more productive rotor. The blade design used outer blade sweep to create twist coupling without angled fiber. Knight & Carver successfully designed, fabricated, tested and evaluated STAR prototype blades. Through laboratory and field tests, Knight & Carver showed the STAR blade met the engineering design criteria and economic goals for the program. A STAR prototype was successfully tested in Tehachapi during 2008 and a large data set was collected to support engineering and commercial development of the technology. This report documents the methodology used to develop the STAR blade design and reviews the approach used for laboratory and field testing. The effort demonstrated that STAR technology can provide significantly greater energy capture without higher operating loads on the turbine.

ACKNOWLEDGEMENTS

The following is a list of some major contributors to the success of this effort. It remains incomplete, since there were so many people that had an indelible impact on this effort.

Gary Kanaby : Project Manager : Knight & Carver Wind Group
Kevin Jackson : Principal Investigator : Dynamic Design Engineering
Mike Zuteck : Principal Investigator : MDZ Consulting
Case van Dam : Aerodynamics, Performance, Acoustics : UC Davis
D.M. Hoyt : Finite Element Structural Analysis : NSE Composites
Doug Graesser : Finite Element Structural Analysis : NSE Composites
Scott Larwood : Aeroelastic Response & Loads : UC Davis
Rafay Navaid : Blade Design Specifications : Knight & Carver
Rick Santos: Aeroelastic Response & Loads, Fatigue Testing : Santos Wind Engineering
Conrad Lococo : Prototype Tooling Fabrication : Knight & Carver
Leo Martinez : Material Testing, Prototype Fabrication & Static Testing : Knight & Carver
Manny Buenrostro : Prototype Blade Fabrication : Knight & Carver
Wally Thompson : Prototype Blade Fabrication : Knight & Carver
Eric Jacobson : Static and Field Testing : Jacobson Technical Services
Scott Hughes : Fatigue Testing : National Renewable Energy Laboratory
Jeroen van Dam : Fatigue Testing : National Renewable Energy Laboratory
Darren Rahn : Fatigue Testing : National Renewable Energy Laboratory
Todd Dobbins : Field Testing : Terra Gen Power
Paul McGrew : Field Testing : Terra Gen Power
Dean Landon: Field Testing : Terra Gen Power
Darren Kelly : Field Testing : Terra Gen Power

We would also like to acknowledge the tremendous support provided by Sandia Labs and the Department of Energy staff during the term of this effort. Our success in this project was intimately tied with the pragmatic and flexible guidance provided to Knight & Carver and to the whole development team by Tom Ashwill and other members of the Sandia wind energy team.

TABLE OF CONTENTS

LIST OF FIGURES

LIST OF TABLES

EXECUTIVE SUMMARY

The STAR blade development program has been successfully completed. Field testing demonstrated that the Sweep Twist Adaptive Rotor more than achieved the project goal of 5-8% greater energy capture without higher operating loads on the turbine.

Knight & Carver was contracted by Sandia National Laboratories to develop a sweep-twist adaptive blade (STAR) that reduced operating loads, thereby allowing a larger, more productive rotor. The blade design used outer blade sweep to create twist coupling without angled fiber. Knight & Carver successfully designed, fabricated, tested and evaluated a blade prototype. Through laboratory and field tests, Knight & Carver showed the STAR blade met the engineering design criteria and economic goals for the program.

The STAR project began in the fourth quarter of 2004 and proceeded in several main stages. The first year initially produced parametric studies for the best materials and manufacturing methods to use for this blade development effort. Also, the first year was used to prepare engineering design calculations and models, which resulted in a prototype blade specification that was released in the Spring of 2005. The first prototype blade was fabricated and static tested early in 2006. Some modifications to the blade design were implemented and the field test and fatigue test prototype blades were fabricated in the Fall of 2007. The blades were installed on the test turbine in Tehachapi during the Winter of 2007. Field test began in April 2008 and was completed that Summer. Fatigue testing at NREL started in the Summer of 2008 and was completed early in 2009.

- Preliminary Studies 2004
- Prototype Design 2004-2005
- Prototype Fabrication 2006-2007
- Prototype Testing 2007-2009

Note: This report is a public version of a cost-shared contract. Wind protected data was not included in this version.

The STAR blade was successfully tested in Tehachapi during the spring of 2008 and a large data set was collected to support engineering and commercial development of the technology.

The STAR rotor was extensively tested over a period of three months (April 2008 through June 2008) at a site in the Tehachapi Mountain area of California. During the test period measurements were collected to measure performance and operating loads for the STAR prototype rotor operating on a Zond 750 kW turbine, as shown in Figure 1.1.

Figure 1.1 Photographs of Zond 750 test turbine with STAR prototype blades.

The power performance improvement of the STAR rotor was somewhat greater than predicted by the increase in the swept area alone.

- The Zond 750 power curve for the baseline 48 meter diameter version (Z48) was generated using the best performance of three turbines in Group 2 (RP-05, RP-06, and RP-07). These turbines operated in a low turbulence location on the site. Data points selected as the best of this group are well matched with a baseline Z48 meter performance model, which provides validation of the modeling approach. The baseline Z48 blades were conventional in design and 23.2 meters in length.

- The actual measured power output using the 26.2 m STAR blades was somewhat better than predicted by the 54 meter performance model in the region below 10 m/s, as shown in Figure 1.2 and significantly above the baseline in the operating range from 2 to 14 m/s.

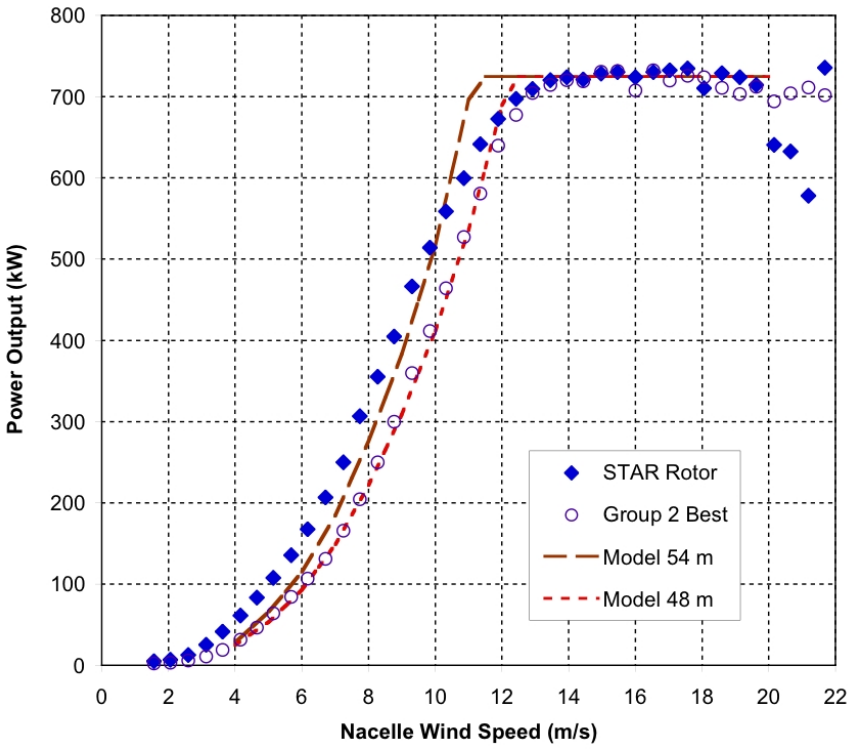

Figure 1.2 STAR and best of group 2 power output as a function of nacelle measured wind speed.

The STAR rotor increased average energy capture by 10-12% as compared to baseline Z48 turbines.

- Figure 1.3 shows power output for the STAR rotor as compared to the average for four baseline turbines (Group 1) operating at the field test site.
- The baseline turbines were organized into two groups. Group 1 was comprised of four ridgeline turbines with high energy capture.
- June 2008 operating data were evaluated when all of four Group 1 turbines were online generating power simultaneously with the STAR rotor.
- This analysis showed that the STAR rotor improved energy capture by 12%.

Turbine Group 1	Energy (kWh)	Compare
RP-01	243009	101%
RP-02	236301	99%
RP-04	237148	99%
RP-08	242496	101%
Average	239738	100%
STAR	268711	112%

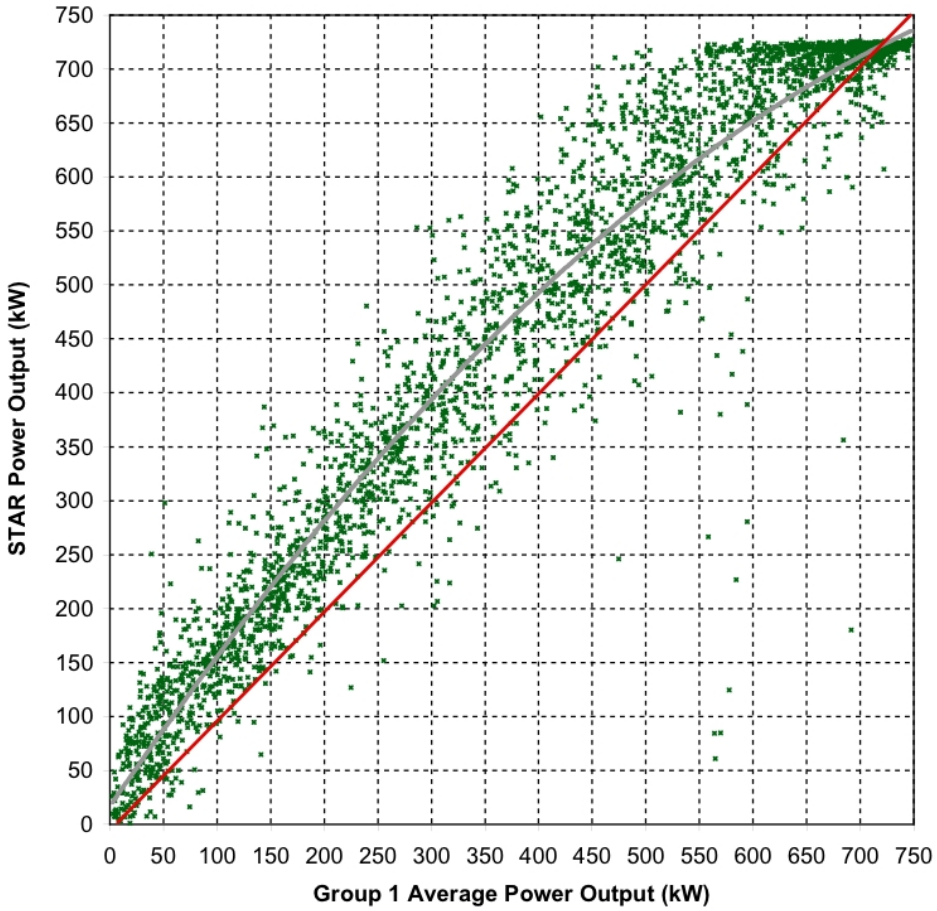

Figure 1.3 STAR power output as compared to Group 1 average power output with all turbines online.

The maximum blade loads recorded during testing were well below the design value used to certify the Zond Z48 turbine. The measured loads were equivalent to those measured on other Zond turbines at sites in Minnesota and Iowa.

- Over 400 hours of blade root strain gage bending measurements were collected over a wide range of operating conditions.
- Maximum values for the root bending moment were recorded for each ten minute record, representing over 2400 individual data points.
- The blade root flatwise load maxima were rank ordered from highest to lowest.
- The maximum recorded values were safely below the design maximum operating load, as shown in Figure 1.4.

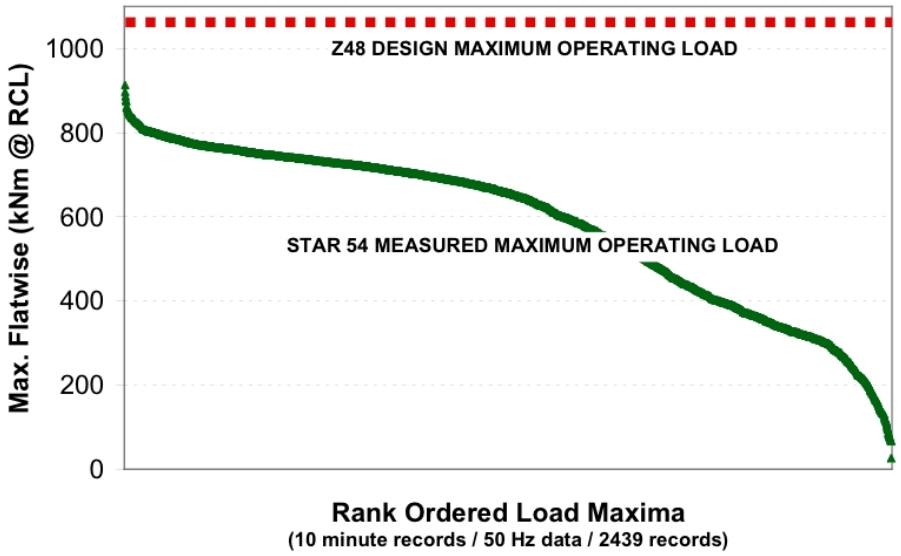

Figure 1.4 Measured maximum flatwise bending moment compared to design loads.

Laboratory fatigue testing validated the STAR blade structure under the application of loads representative of a full design operating lifetime.

- The STAR fatigue test blade successfully completed a load sequence that represented 20 years of design operation without damage.

At the time this report was prepared, the STAR prototype blades had operated in commercial production mode from April 2008 through November 2009 without incidents. Energy production increases from the STAR blades make it the best performing Zond turbine at the site.

Figure 1.5 Illustration of the STAR prototype turbine.

1 INTRODUCTION

1.1 Project Goal

In 2004 the United States Department of Energy Wind Energy Research Program began an effort to develop wind technology that will allow wind systems to compete in regions of low wind speed. The scope of work for the Component Development portion involved the design, fabrication and testing of a component expected to improve the performance, reliability or cost of wind turbines suitable for low-wind-speed sites.

Knight & Carver was contracted by Sandia National Laboratories to develop a sweep-twist adaptive blade (STAR) that reduced operating loads, thereby allowing a larger, more productive rotor. The blade design used outer blade sweep to create twist coupling without angled fiber. The project began with the development of a Project Work Plan that described the details of the contract effort and guided the work activities. Knight & Carver then designed, fabricated, tested and evaluated a blade prototype. Through laboratory and field tests, Knight & Carver showed the STAR blade met the design criteria and goals.

1.2 Project Timeline

The STAR project began in the fourth quarter of 2004 and proceeded in several main stages. The first year initially produced parametric studies for the best materials and manufacturing methods to use for this blade development effort. Also, the first year was used to prepare engineering design calculations and models, which resulted in a prototype blade specification that was released in the Spring of 2005. The first prototype blade was fabricated and static tested early in 2006. Some modifications to the blade design were implemented and the field test and fatigue test prototype blades were fabricated in the Fall of 2007. The blades were installed on the test turbine in Tehachapi during the Winter of 2007. Field test began in April 2008 and was completed that Summer. Fatigue testing started in the Summer of 2008 and was completed early in 2009.

- Preliminary Studies 2004
- Prototype Design 2004-2005
- Prototype Fabrication 2006-2007
- Prototype Testing 2007-2009

1.3 Report Organization

The report is organized into eight sections. Unless otherwise noted the work presented in this report was developed as part of the STAR blade project effort.

Section 1 begins with this Introduction and is followed by a Project Summary.

Section 2 reviews the engineering process used to develop the STAR blade and the work conducted to develop the prototype tooling and blades. Section 2 also provides an overview of the laboratory and field testing efforts.

Section 3 provides a review of wind turbine blade design issues and discusses some of the tradeoffs that were considered during the development of the STAR blade.

Section 4 discusses manufacturing process options that were considered in developing the STAR blade.

Section 5 provides details of the various engineering design studies that were conducted during the project. This includes design of the STAR airfoil series, calculation of the design loads, and structural analysis results.

Section 6 reviews laboratory static testing at Knight & Carver, fatigue testing at NREL, and field performance and load testing on a prototype turbine in Tehachapi.

2 PROJECT SUMMARY

2.1 Blade Design

2.1.1 Conceptual Design

Conceptual blade design began with an initial rotor target diameter of 56 meters. This rotor size was selected based upon extension of earlier work on the sweep twist concept and prior experience with the Z-750. The baseline turbine can adjust pitch from feather (90°) to run pitch (0°) as needed to control power. The 750 kW generator operates at variable speed between 20 and 32 rpm.

Four different Sweep Twist Adaptive Blade (STAR) planforms were prepared for evaluation. All of the blades had equivalent IEC Class III extreme loads. Figure 2.1 shows the swept STAR 1 blade and Table 2.1 provides a summary of the four planforms. The initial rotor performance calculations were reviewed and the sweep-twist calculations were modified to feed twist back into the distributed thrust.

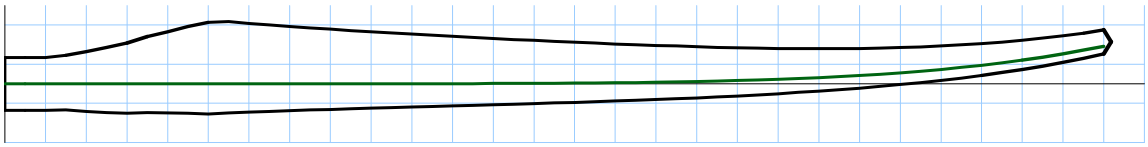

Figure 2.1 Initial swept blade planform for the STAR blade.

Table 2.1 Conceptual design planform summary table.

Blade Type	Blade Length (m)	Planform Area (m2)	Rotor Diameter (m)	Swept Area (m)	Specific Power (W/m2)	Blade Tip Speed		Gust Load at Run Pitch		
						Z48 (m/s)	Z50 (m/s)	12 m/s (kN)	14 m/s (kN)	16 m/s (kN)
STAR 1	26.000	36.2	53.636	2259	332	95.8	90.7	156	192	224
STAR 2	26.682	37.1	55.000	2376	316	98.2	93.0	167	203	232
STAR 3	27.182	38.7	56.000	2463	305	100.0	94.7	170	207	238
STAR 4	27.182	38.7	56.000	2463	305	100.0	94.7	166	202	233

The first blade planform, designated as STAR 1, was initially selected because it provided a maximum rotor power coefficient which was near optimum values (52%) as shown in Figure 2.2.

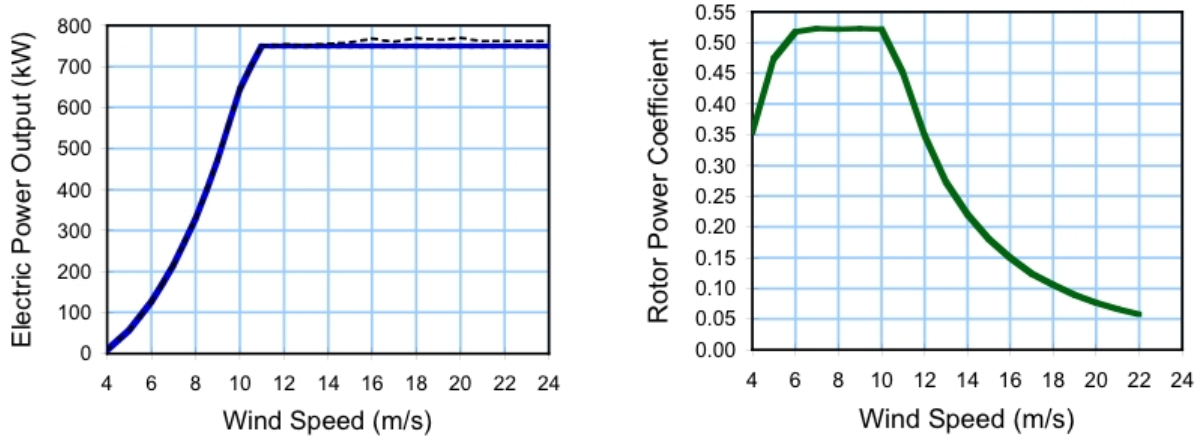

Figure 2.2 Power curve and rotor power coefficient for the STAR blade starting planform.

2.1.2 Preliminary Design

At the conclusion of the conceptual design phase STAR 3 was selected as the starting point for preliminary design, because this design provided the best annual energy capture. The preliminary planform design effort modified the STAR 3 design and a revised blade, designated as STAR 5, was used as the starting point for structural modeling. The STAR 5 blade design used the same primary materials as conceptual design, namely a high efficiency glass unidirectional fabric for the spar caps, with blade shell panels and shear webs composed of double bias (DB) glass fabric over balsa coring. The initial structural material choices were replaced by uni-directional roving for the spar caps, with foam coring for both the shell panels and shear webs. The shear web skins were DB fabric, but the skins included a combination of DB fabric and spanwise oriented unidirectional fabric to increase the overall stiffness to weight of the blade, while improving its torsional response.

Knight & Carver performed tests on a variety of candidate materials during the preliminary design phase. This testing showed that some, but not all unidirectional fabrics were suitable for following the curvature of the outer blade. The work also provided the engineering design team with knowledge of the maximum curvature that was allowable before manufacturing became problematic. Laminate impregnation by pulling wetted roving through a metal die was also found to be an excellent choice for building the curved spar cap.

2.1.3 Detailed Design

A number of structural design iterations were conducted during detailed design of the blade designated as STAR 6. The engineering approach relied heavily on the use of section analysis during this phase of work. A range of design iterations were completed to assess the effect of the very large number of structural and geometric variations needed to converge to a design that would meet the key driving criteria of twist response, deflection, and deadweight moment. While well established in many previous design projects, it was known that section analysis cannot capture certain aspects of structural response where 3D effects play a role. To assess whether these limitations were significant for the sweep twist design, a separate finite element model (FEM) was also created to evaluate such effects. In addition, the FEM provides an independent check of bending and twisting response, far more detailed stress maps, and a more sophisticated evaluation of panel buckling behavior. Another primary function of the FEM was to “fine tune” the section analysis process.

To provide an efficient means of comparison, the FEM used the same material properties as the section analysis design process. Since the methods are quite different, there were certain necessary differences in details, judged to be of no real significance. Also, to reduce effort spent modeling details not of significance to the sweep twist response, the inboard 15% of the blade was not modeled in the FEM.

The agreement between section analysis and FEM was excellent in flatwise bending under the rated power operating load case. Flatwise and edgewise stiffnesses (EIs) derived from the FEM bending response agree well with those derived from section analysis. Estimating the magnitude of the twist response was an area where convergence was difficult.

The STAR blade was designed using a stressed-shell constructed from E-glass and epoxy resin. The blade shells were made from biaxial fabric with unidirectional spar caps. The coring material was PVC foam. The STAR 6 blade used a single shear web design, curving as necessary to follow the spar cap. The single shear web improved torsional flexibility, which was important for this concept to properly shed operating loads.

The blade shell and shear web molds were designed with temperature control to assure proper resin viscosity and for post curing of the laminate. The molds were designed to incorporate thermal control using water or air circulating in a jacket behind the mold surface.

2.1.4 Initial Prototype Design

Knight & Carver began discussions with Euros, a blade engineering and manufacturing firm in Germany, to purchase technology and tooling for manufacturing a conventional 750 kW wind turbine blade during the detailed design phase. The Euros EU50 blade was certified by DEWI (Deutsches Windenergie Institut) and had design features that fit the Zond turbine, as shown in Table 2.2. This blade was found to be an excellent match for the Zond 750 turbines. The Z750 fleet had serial blade design defects and large numbers of blades were needed to replace existing failed blades. K&C subsequently purchased the North American rights to manufacture the EU51 blade family and set up a production facility in South Dakota to fabricate blades for the Z48 and Z50 turbines.

Table 2.2 Euros EU50 blade design parameters.

GENERAL		
Rotor diameter (approx.)	(m)	50
Rated power	(kW)	750
Power control		Pitch
Nominal wind speed	(m/s)	11.1
Nominal tip speed	(m/s)	75
Materials		Glass/Epoxy
Mass	(t)	2.20
AERODYNAMICS		
Airfoils		EUROS, DU, NACA64
Design tip speed ratio		7.5
Max. power coefficient		0.49
GEOMETRY		
Blade length	(m)	24.50
Max. Chord	(m)	2.40
Twist	(deg)	11.5
Blade area	(m^2)	39.1

The blade molds that Knight & Carver purchased from Euros were segmented into sections. The STAR 6 planform design was modified so that it incorporated the root section of the Euros blade and the designation was changed to STAR 7. Figure 2.3 shows the STAR 7 blade

planform as dimensioned from the blade root mounting flange. The STAR 7 design remained 56 meters in diameter, with the blades mounting to the hub flange at a radius of 816 mm. The airfoils were aligned on the chord line at a chordwise position of about 30% from the leading edge. In the root area the axis shifts from 30% to 50% to adapt to the root circle. The molds and external profile of the root section (mounting flange to 11.75 m span) were identical in both the Euros and STAR 7 blades. STAR 7 retained the curved main and tip sections that had been developed in earlier design phases.

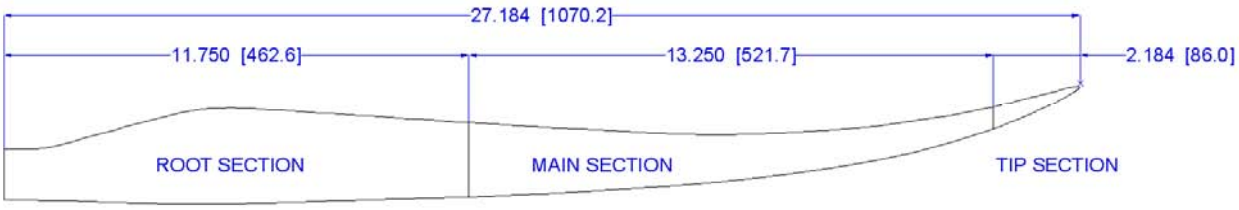

Figure 2.3 STAR 7 blade planform drawing.

2.2 Prototype Tooling and Blades

2.2.1 Blade Pattern

Blade tooling fabrication was completed by Knight & Carver at their factory in San Diego. Knight & Carver purchased EU-51 blade tooling from Euros and had it shipped to their facilities in California. The Euros tooling was refurbished and used to build the STAR blade mold root section. The STAR blade main and tip sections were matched to the EU-51 blade pattern at the 11.75 meter radial position.

The blade pattern was created using airfoil templates that were uniformly spaced and covered by wooden battens, as shown in Figure 2.4. The space between battens was filled and sanded until a smooth surface was obtained as shown in Figure 2.5. Once the pattern was completed, Knight & Carver fabricated two skin molds, which were used to fabricate the STAR blades.

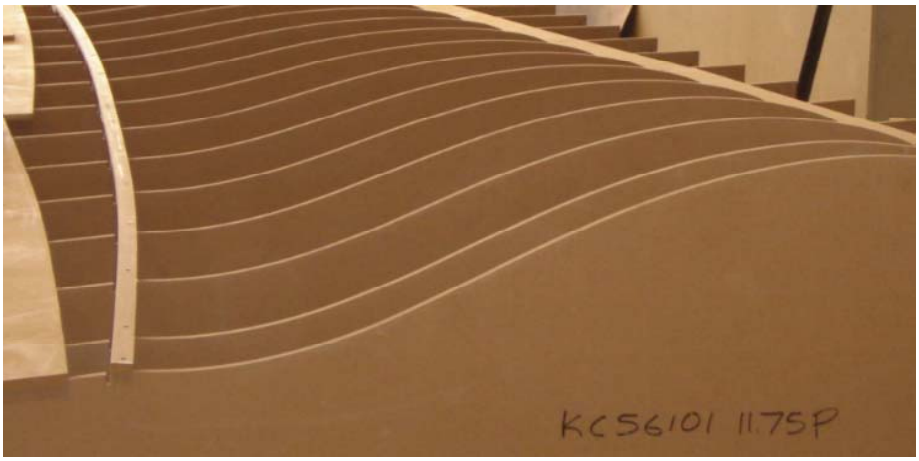

Figure 2.4 Airfoil templates were used to create the curved pattern for the STAR blade.

Figure 2.5 Workers smoothing the STAR blade pattern.

2.2.2 Blade Molds and Assembly Tools

Knight & Carver fabricated blade molds by first laminating over the finished pattern, as shown in Figure 2.6. The blade molds were constructed in sections for ease of shipping and a photograph of the root section molds is shown in Figure 2.7. The molds were lightweight in design and were not designed to be used for bond assembly. A separate fixture (Figure 2.8) was used to hold the blade shells in position during final bonding.

Figure 2.6 Laminating over the finished pattern for the STAR blade.

Figure 2.7 Root section molds for the STAR blade.

Figure 2.8 Assembly fixture for holding the blade shells during final bonding.

2.2.3 Prototype Blade Fabrication

The first blade prototype was fabricated in San Diego. In this first blade, a single shear web was used in the outboard sections, which was consistent with earlier design phases. However, the shear web in the root area was modified to match the Euros design and had two webs. The double-to-single shear web arrangement was used primarily because it minimized changes to the design and tooling of the root region.

The first blade prototype was tested statically in the flatwise direction to measure twist under design load conditions. The results of the static test were used to successfully verify design calculations for twist response of the STAR blade under expected operating loads. This test also showed that the complexity added by the double-to-single shear web created undesirable stresses in the blade. The final blade laminate and shear web design used a single shear web.

Knight & Carver began operating a new manufacturing facility in South Dakota to fabricate blades in 2007. The STAR molds and other tooling were shipped to the new factory prior to fabrication of one (1) fatigue test blade and three (3) field test blades. The fatigue and field

test rotor diameter was reduced from 56 to 54 meters for the Z48 variant, which was the version of the Zond 750 turbine ultimately selected for the field test effort. The 56 m diameter rotor blades are 27.2 m long and the 54 m rotor blades are 26.2 m in length. The reduced blade length was accomplished by shortening the root and tip each by 0.5 m. Figure 2.9 shows a photograph of the blade shell mold during the manufacturing process.

Figure 2.9 Fabrication of the STAR 54 field test blades in South Dakota.

2.3 Material and Blade Testing

2.3.1 Material Testing

Knight & Carver conducted a variety of material tests to evaluate various fabrics for use in making curved spar caps. The results showed that it was possible to manufacture the curved spar cap with vacuum infusion using fabrics available in the market. We subsequently decided to move forward with a spar cap manufacturing process based upon wet pultruded glass rovings.

2.3.2 Blade Static Testing

A static blade test was performed on the first blade prototype to verify the twist predictions. The test used a unique load approach that accurately modeled the design aerodynamic load for the blade at maximum twist. The barrel test, shown in Figures 2.10 and 2.11, was successful in verifying the twist response of the STAR blade under design operating load conditions.

Figure 2.10 Barrel testing the prototype blade to verify twist under load.

Figure 2.11 Barrel testing the prototype blade to verify twist under load.

2.3.3 Field Testing

The STAR blade was installed on a Z48 turbine in the Tehachapi Mountain area of California as shown in Figure 2.12. Measurements were collected over a period of three months (April, May, June 2008). During the test period measurements were collected to measure performance and operating loads for the STAR rotor. A large data set was collected to support engineering and commercial development of the technology.

Figure 2.12 STAR prototype blades on the Zond 750 test turbine in Tehachapi in April 2008.

The power performance improvement of the STAR rotor was somewhat greater than predicted by the increase in the swept area alone. A Z-48 power curve was generated using the best performance of three turbines (RP-05, RP-06, and RP-07) operating in a low turbulence location on the site. Data points selected as the best of this group are well matched with a 48 meter performance model, which provides validation of the modeling approach.

The actual measured power output of the STAR was somewhat better than predicted by the performance model in the region below 10 m/s, as shown in Figure 2.13. The power output of the STAR rotor was substantially above the baseline turbine over the operating range from 2 to 14 m/s. The STAR rotor increased average energy capture by 10-12% as compared to baseline Z48 turbines.

The maximum blade loads recorded during testing were well below the design values used to certify the design engineering of the Zond 750 turbine. Over 400 hours of blade root strain gage bending measurements were collected over a wide range of operating conditions. Maximum values for the root bending moment were calculated for each ten minute record, representing over 2400 individual data points. The blade root flatwise load maxima were rank ordered from highest to lowest and are graphed in Figure 2.14. The maximum recorded values were safely below the design maximum operating load.

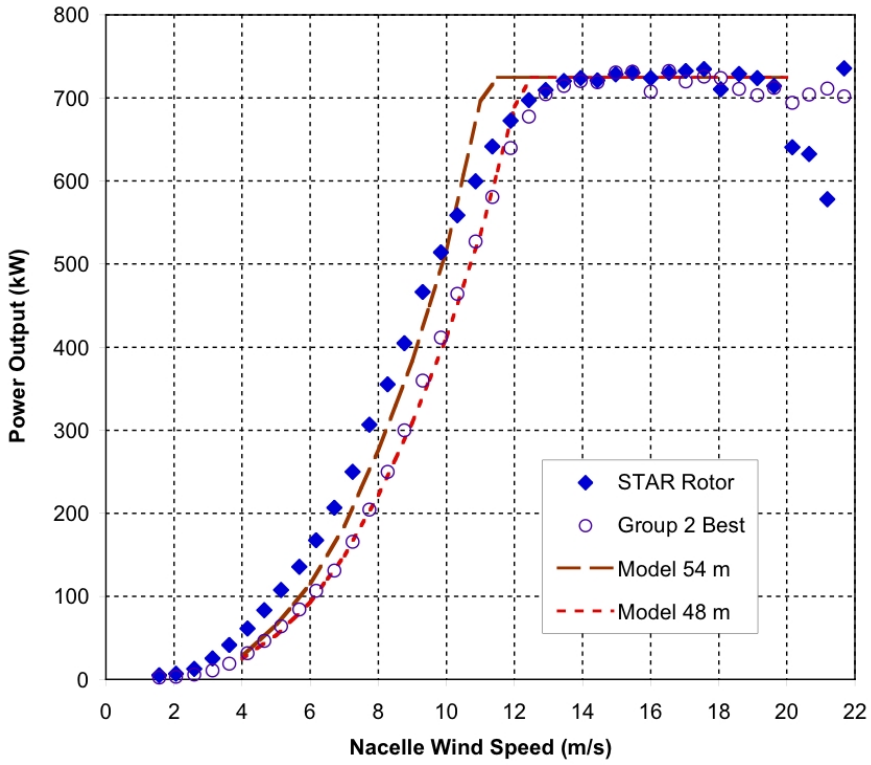

Figure 2.13 STAR prototype power performance compared to the best baseline turbine and modeled with two rotor sizes.

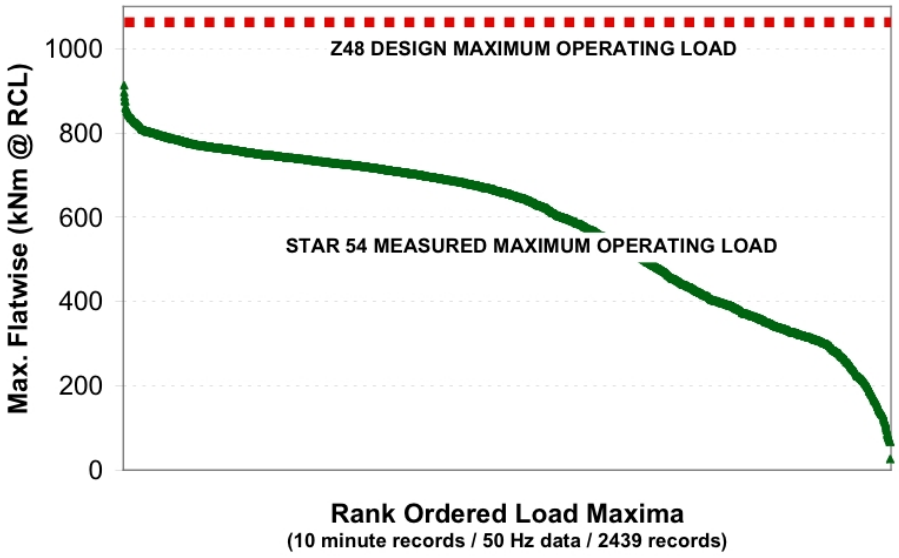

Figure 2.14 Measured maximum flatwise bending moment compared to design loads.

The measurement results obtained from the field testing effort were compared to the model predictions for performance and operating loads. The binned average of the mean flatwise moment was well correlated to the ADAMS model predictions, as shown in Figure 2.15. These results provide confidence that the tools used to design the STAR blade are adequate for engineering design purposes.

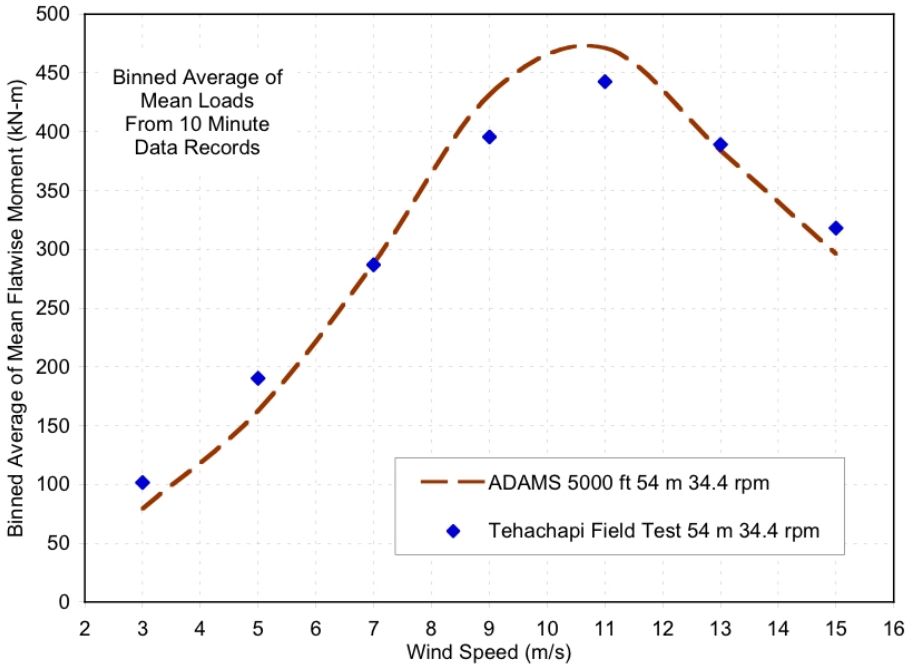

Figure 2.15 Comparison of measured flatwise loads to the ADAMS model predictions.

2.3.4 Fatigue Testing

One of the STAR prototype blades was shipped to NREL for fatigue testing. The fatigue test blade was mounted in the test stand and was cycled for the equivalent of twenty years operation without showing damage. Further testing showed that significant blades strength remained after completion of the design load fatigue test sequence.

3 WIND BLADE DESIGN REVIEW

This section provides a general review of wind turbine blade design and outlines some of the tradeoffs that were considered by Knight & Carver during the development of the STAR blade.

3.1 Structural Design

Wind turbine blades are almost exclusively fabricated from composite materials. The most common fiber type is fiberglass (specifically E-glass), although carbon fiber is finding usage in some specific applications. Polyester, vinylester, and epoxy resin systems are all currently used in the fabrication of wind blades. As the size of blades has increased there has been increasing design emphasis on reducing blade weight, which has in turn led to selective pressure toward higher strength materials.

3.1.1 Spar-Shell Construction

There are two general approaches to wind blade structural design: spar-shell and stressed-shell construction. The spar-shell construction method uses a tubular main spar as the primary structural element as shown in Figure 3.1. A lightweight aerodynamic shell encloses the main spar and is bonded to it. The blade components are a tubular main spar that extends nearly to the tip of the blade and two aero-shells that are bonded to the spar. Foam or balsa coring is included in the blade skin to prevent panel buckling under compressive loads.

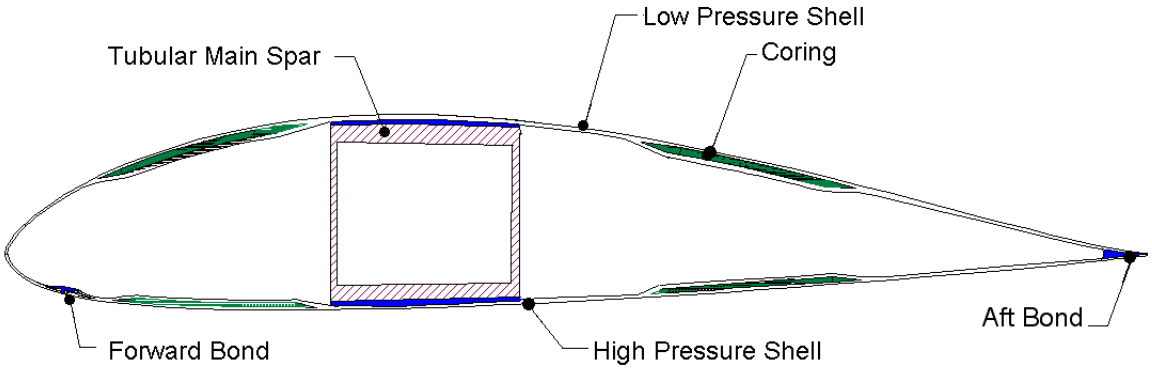

Figure 3.1 Typical section of a blade using spar-shell construction.

Advantages of spar-shell construction are the relatively simple structural shape of the main spar, the direct load path through the blade root, and a clear separation of primary and secondary structural elements. Since the shell is secondary structure this design approach is particularly tolerant of shell damage during transport or operation. The tubular main spar (Figure 3.2) is usually fabricated over a metal mandrel (Figure 3.3) and the process can be highly automated. For large blades there is also the possibility of shipping the main spar and performing assembly on site.

Figure 3.2 Root view of spar-shell blade with bonded threaded inserts.

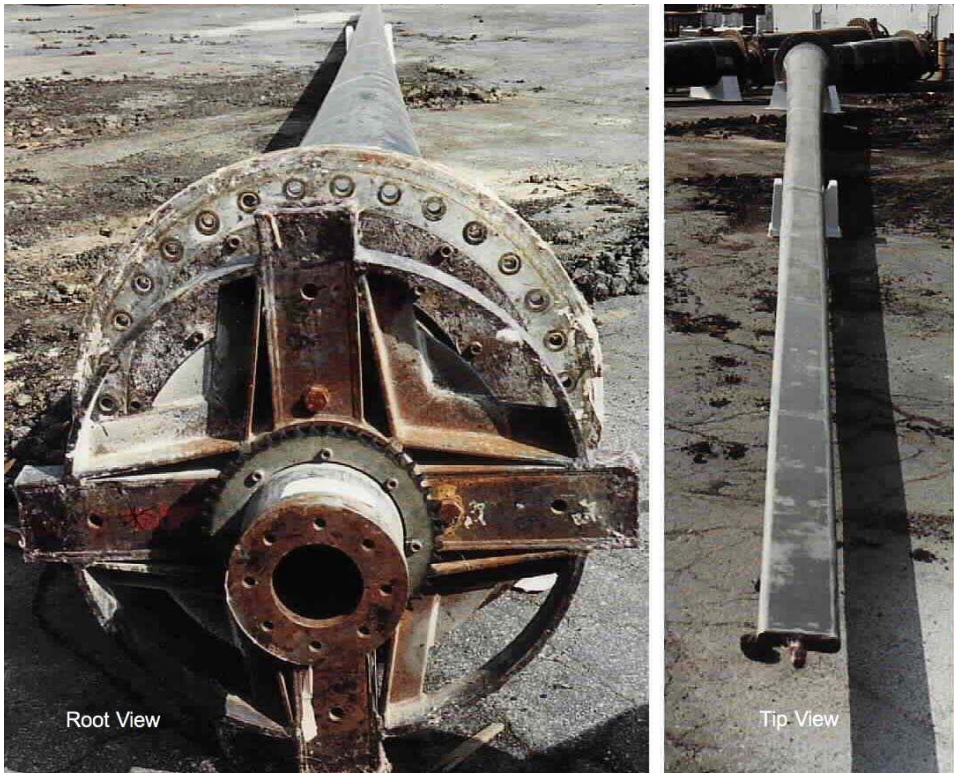

Figure 3.3 Steel mandrel used for fabricating a tubular main spar.

Disadvantages of the spar-shell construction method include reduced structural efficiency and large bonding surfaces between main components. The active dimensions of the main spar are slightly reduced in the flatwise direction and greatly reduced in the edgewise direction. As a result, spar-shell construction tends to be less efficient in its use of materials for a given strength and stiffness, especially with regard to edgewise properties. The second major disadvantage of this approach occurs because the spar-shell interface has a relatively large surface area. Final assembly of the components is difficult because of the large bond area and control of the adhesive bond thickness can be problematic. It is relatively difficult to maintain proper bond line and prevent voids.

3.1.2 Stressed-Shell Construction

Stressed-shell construction has been widely used in the wind industry and its higher structural efficiency is a particular advantage with larger blade sizes. With this design approach the blade is constructed from two structural shells, which are connected internally by shear webs bonded between the shells (Figure 3.4). Each blade shell has an area near the maximum thickness region of the airfoil that composes the "spar cap". The spar cap is constructed from unidirectional fiber which is oriented in the spanwise direction.

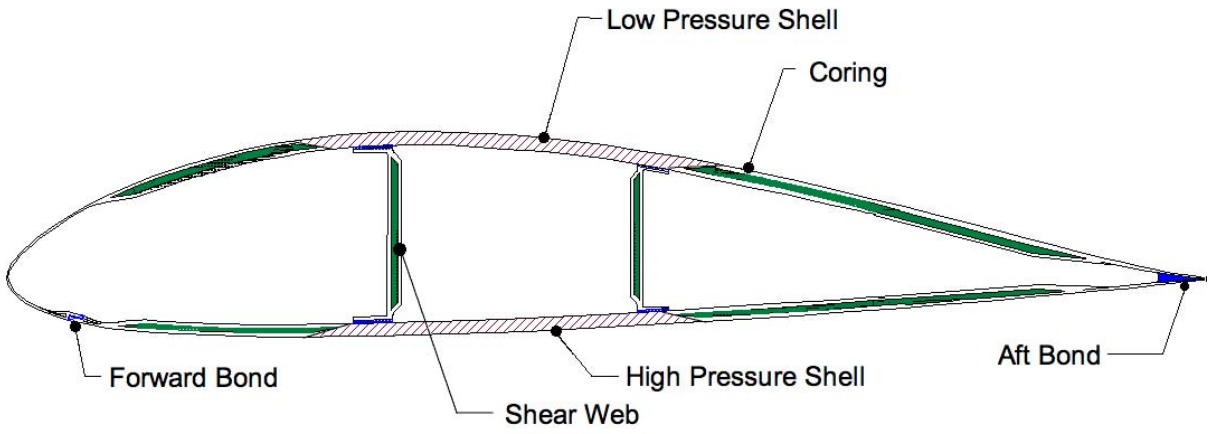

Figure 3.4 Typical section of a blade using stressed-shell construction.

Typically there are two shear webs bonded between the blade shells using flanges (Figure 3.5). The shear webs are designed to carry shear between the upwind and downwind spar caps. The webs must also withstand large compressive loads created by bending of the blade during operation and are stabilized against buckling through the use of balsa or foam cores. The root end of the shear webs typically terminate with a half-moon shape, which reduces the abrupt change in stiffness.

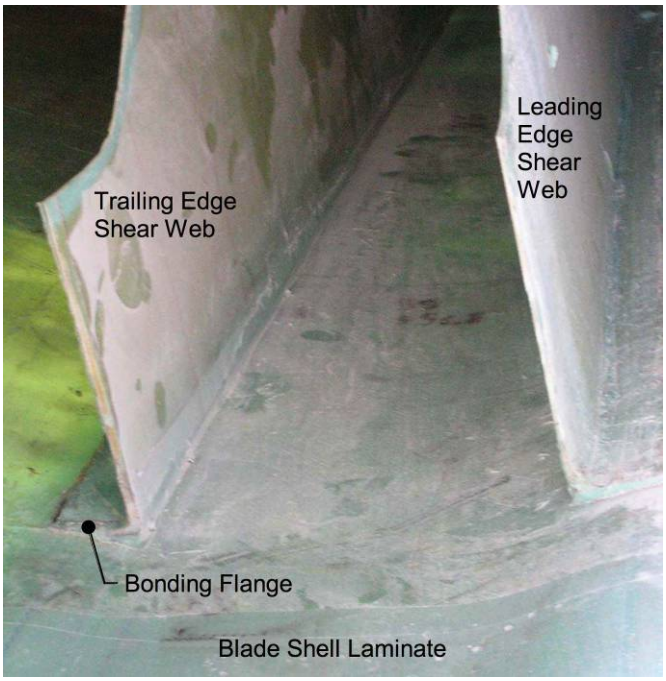

Figure 3.5 Shear web attachment to the shell at the inboard termination.

3.2 Root Attachment

The attachment of the blade root to the rotor hub has been a major structural design challenge for the wind industry. Three primary means have been used for attaching blades: one-piece metal root fitting, individual fastener inserts, and T-bolt connections.

3.2.1 One-Piece Root Fitting

The one-piece root fitting was employed by a number of manufacturers and constructed from either steel or aluminum. An schematic drawing of a one piece root fitting design is shown in Figure 3.6 and a photograph of an example blade is provided in Figure 3.7.

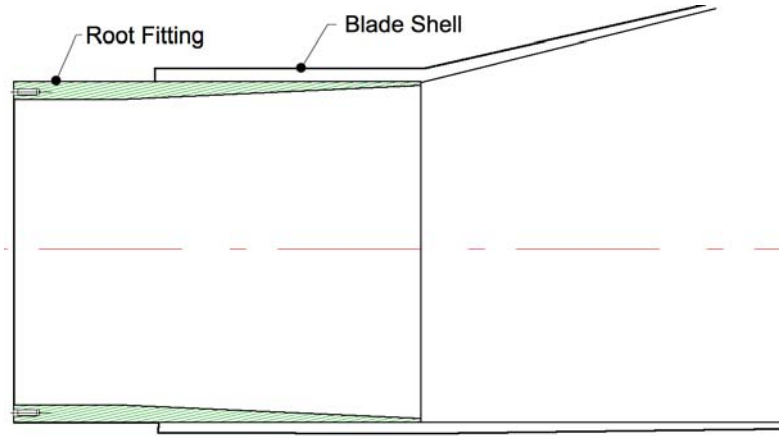

Figure 3.6. Schematic drawing of a one-piece bonded root fitting.

Figure 3.7 Photograph of the Zond Z-50 blade with a one-piece steel bonded root fitting.

The one-piece bonded root fitting design had a number of disadvantages, which included high weight, poor strain compatibility, and high adhesive bond stresses. This design is now considered obsolete and has been replaced by individual fastener inserts and T-bolt connections.

3.2.2 Threaded Inserts

Some manufacturers have laminated the root inserts directly into the blade during the manufacturing process, while others have formed or drilled holes and bonded the inserts during blade assembly. Direct embedment of the inserts can potentially reduce the number of manufacturing operations, but movement of the inserts during cure complicates this approach. With large wind turbine blades it can be difficult to maintain the necessary tolerances for proper fastener placement with the direct embedment approach. The other alternative is to mold or drill holes into which the inserts are bonded. A schematic drawing of a threaded insert is shown in Figure 3.8. This insert design tapers and is counter drilled to provide excellent strain compatibility. Similar designs have been employed on large wind blades (Figure 3.9) with good success.

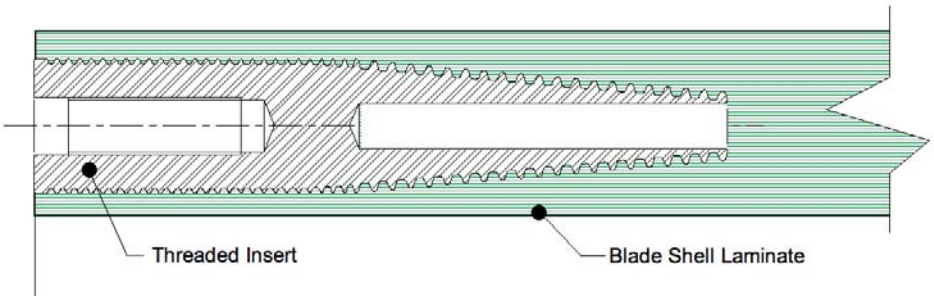

Figure 3.8 Schematic cross-section drawing of a threaded insert root attachment.

Figure 3.9 Vestas V80 blade with bonded threaded inserts.

Threaded inserts provide a smooth load transfer between the composite laminate and the metal components of the hub. Well designed inserts are strain compatible and the joint is lightweight and structurally efficient. The adhesive bond surrounding each insert is typically about 5 mm in thickness and allows location of the inserts on the bolt circle to easily fit to accurate tolerances. The primary disadvantage of this approach is the relatively high cost of the threaded inserts and the difficulties associated with drilling and bonding a multitude of components during blade final assembly.

3.2.3 Sliced Root Studs

There are several low-cost approaches to bonded inserts that have not been fully engineered, but appear to be cost effective. Further research and development effort is needed to properly design and manufacture sliced root studs, but that approach could be the least expensive for achieving high performance with low material and manufacturing cost. Sliced root studs are fabricated from threaded rod that is cut on an oblique angle to provide a smooth shear transfer to the composite materials.

The risk of corrosion at the adhesive bond line is greatly diminished by the use of high nickel steel, which provides high resistance to corrosion. Use of higher quality nickel steel is economically possible because of the simple manufacturing operations required to roll 30 mm threaded rods and slice them into proper lengths. The manufacturing process for sliced root studs can be easily automated using traditional machining tools.

3.2.4 T-bolt Connection

T-bolt connections have become a standard method for root attachment and the popularity of this approach has grown in recent years. The joint is formed by drilling a series of large diameter holes (60 mm) across the blade root laminate parallel to the blade flange approximately 100 to 150 mm outboard from the flange surface. The blade mounts to the hub at the flange interface. Another set of smaller holes (30 mm) is drilled perpendicular to the flange to intersect the cross laminate holes. A barrel nut is inserted into the cross holes and a root stud is threaded to it as shown in Figure 3.10.

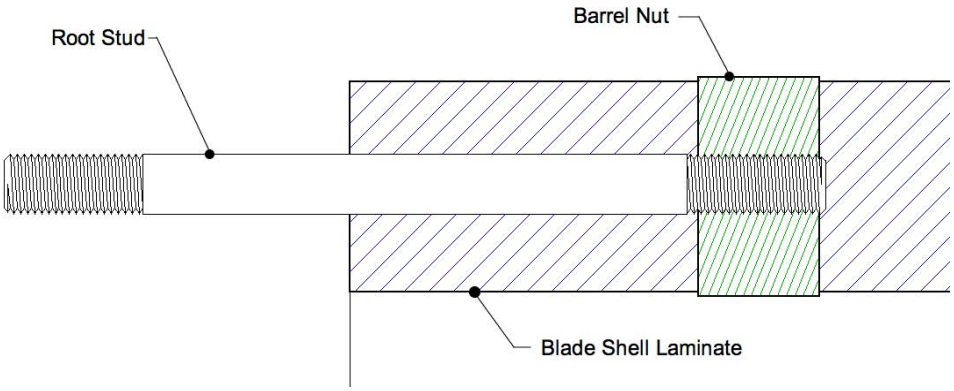

Figure 3.10 Schematic drawing of a T-bolt connection.

The combination of the root stud and barrel nut form a “tee”, from which the name is derived. A photograph of a blade with T-bolt connections is shown in Figure 3.11.

Figure 3.11 Euros EU-51 blades with T-bolt type root attachment.

There are several advantages of T-bolt connections as compared to threaded inserts. A key advantage is the relatively low manufacturing cost of the barrel nuts as compared to threaded inserts. The barrel nuts are manufactured from alloy steel bar stock and require minimal machining. They must be cut to the proper length and have a perpendicular threaded hole across the mid-point. Another advantage of the T-bolt connection is that it provides a mechanical joint that does not rely on adhesives. Damaged studs or barrel nuts can be removed and replaced if necessary.

The disadvantages of T-bolts are somewhat lower structural efficiency and increased laminate thickness as compared to threaded inserts. T-bolts also require high drilling accuracy and perpendicularity to prevent bending of root stud and premature failure of the fasteners.

3.3 Lightning Protection

Lightning protection is an important feature of modern wind blades. The International Electro Technical (IEC) recommendations for lightning protection of wind turbines [1] notes that:

"The most severe damage to wind turbine blades is caused when lightning arcs inside the blade. The arcs may form in the air filled cavities inside the internal surfaces. Another type of damage is seen when the lightning current or part of it is conducted in or between layers of composite materials, presumably because such layers hold some moisture. The pressure shock wave caused by such internal arcs may explode the blade, ripping the blade surface skins apart along the edges and from the internal carrying spar. All grades of damage are seen ranging from surface cracking to complete disintegration of the blade. In some cases pressure waves have propagated from the blade struck by lightning through the hub and into the other blades causing pressure damage to them."

An example of well functioning lightning system is provided in Figure 3.12, which show a photograph of the Vestas V80 blade lightning receptor after an electrical event. This photo shows a small burn mark on the receptor, but no damage occurred to the blade itself.

Figure 3.12 Blade receptor after a lightning strike showing burn marks, but no damage.

The lightning receptor is typically placed near the blade tip, which is the most likely location for impact. Wind turbine blades typically have a moisture vent (weep hole) located near the blade tip. This hole was traditionally placed at the very tip of the blade, but that location has proven to provide a conductive path and can cause blade damage. Euros used a particularly good design approach in the EU-51, which sealed the blade tip and place the moisture vent some distance inboard of the receptor, as shown in Figure 3.13. The receptor should be flush with blade surface to minimize acoustic noise.

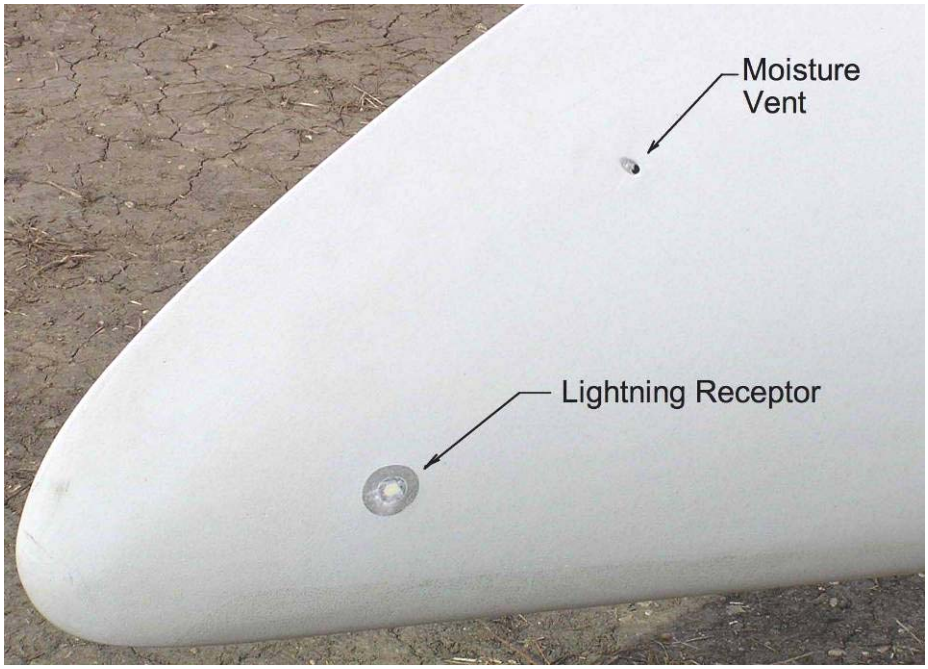

Figure 3.13 Lightning receptor placement at the blade tip.

The energy contained in a lightning strike can be safely conducted through the blade to the ground without damage in many instances. It is important to eliminate moisture from the area surrounding the receptor. During a lightning strike moisture can explosively flash to steam and cause damage to the blade tip. It is also important to have a conductor of sufficient size to carry the electrical current generated by the lightning event. The IEC recommends that the conductor have a minimum cross-sectional area of 50 mm^2. Using a lightning conductor that is greater than the IEC recommendation can considerably reduce temperature excursions in the conductor material during the lightning strike for minimal cost impact. The temperature rise in the conductor scales roughly as the inverse in the cross-sectional area, so doubling the conductor area reduces the temperature rise by a factor of four.

4 MANUFACTURING PROCESS REVIEW

This work was completed during the during the preliminary design phase of the effort and used in evaluation of different potential manufacturing techniques.

4.1 Overview of the Process

An outline of the general process for wind turbine blade manufacturing is presented in Figure 4.1. In this outline the process begins with raw materials being received at the factory and is completed with blades loaded and ready for transport to the wind plant construction site. The manufacturing process presented in this outline defines a generic approach typical of the stressed-shell blade construction used for the STAR blades.

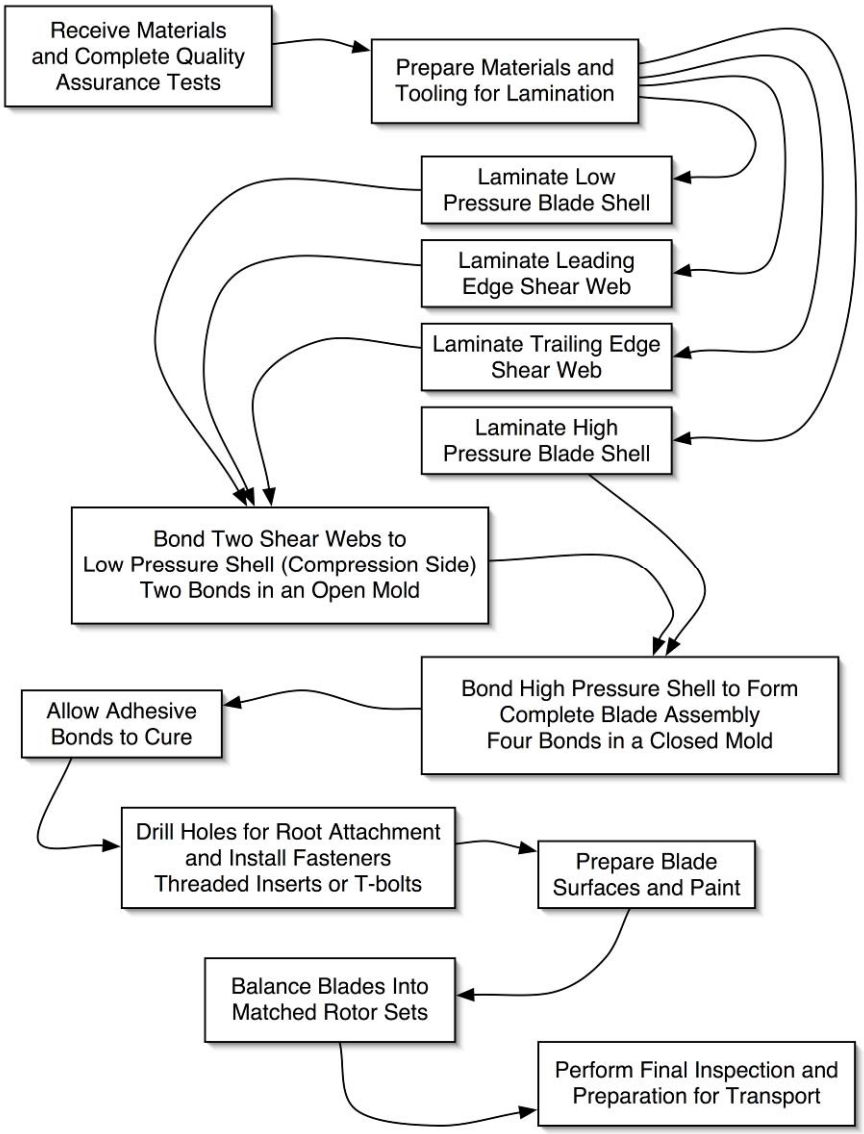

Figure 4.1 Generalized outline of the wind turbine blade manufacturing process.

The process begins with materials being received at the factory. Quality assurance tests are implemented prior to issuing the materials to the shop floor for production. The raw materials for the blade skin are cut to size and formed into kits before lamination in molds. Once the skins are cured the blade shear web is bonded to the downwind, compression surface of the blade. This process is completed in an open mold, which provides assurance in the quality of this critical bond. Once the shear webs are cured sufficiently to remain in position, the upwind, tension skin is bonded at the leading and trailing edges of the blade and at the two shear webs.

TPI Composites and Sandia National Laboratories published data [2] on an example manufacturing plant for a 50 meter blade. This study provides useful information on the facilities and capital cost required to build and operate a 50 meter wind blade manufacturing factory sized to fabricate ten blades per week. An example factory layout is shown in Figure 4.2 and annual plant operating costs as shown in Table 4.1. Cost allocations for various parts of the total blade cost are provided in Figure 4.3 and Table 4.2.

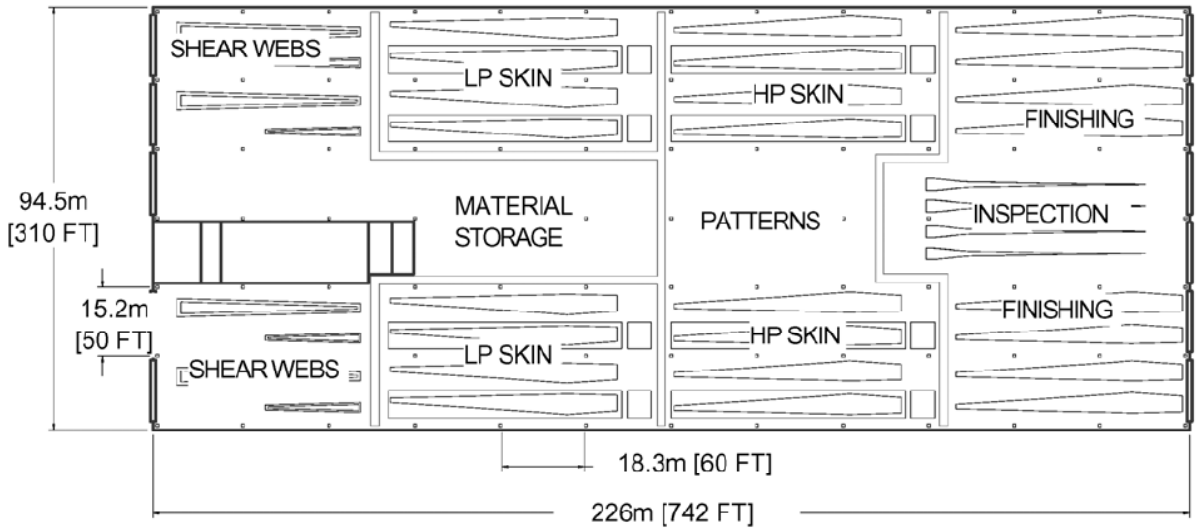

Figure 4.2 Example manufacturing plant layout for 50 meter blades estimated by TPI Composites [2].

Table 4.1 Manufacturing plant cost for several blade sizes estimated by TPI Composites [2].

Blade Length (m)	Plant Floor Area (ft2)	Plant Floor Area (m2)	Plant Cost ($/yr)	Plant Cost ($/MW)
30	164,996	15,329	$1,319,968	$1,813
50	230,020	21,370	$1,840,160	$2,654
70	304,920	28,328	$2,439,360	$3,703

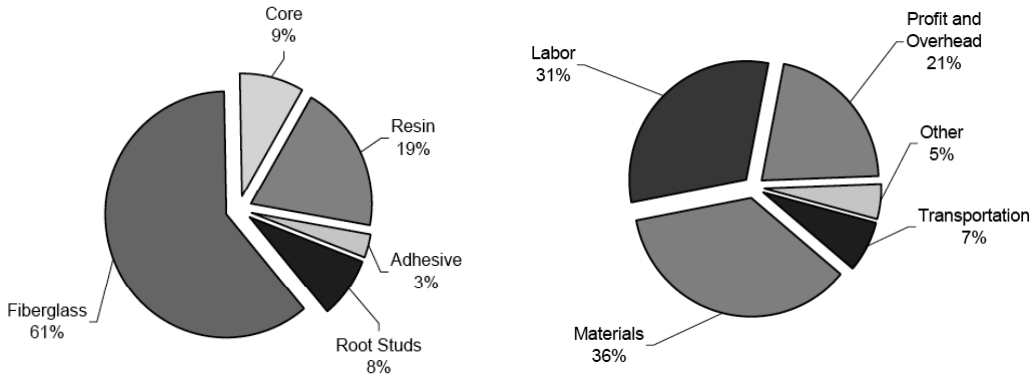

Figure 4.3 Cost allocations for a 50 meter blade according to TPI Composites [2].

Table 4.2 Blade component weight and cost allocations for the Sandia 50 meter blade [2].

Station % r/R	Blade Weight (lbs/ft)	Material Weights by Type: Gel Coat (lbs/ft)	Mat (lbs/ft)	DB Glass (lbs/ft)	Spar Cap +TE (lbs/ft)	Balsa (lbs/ft)	Plexus/ Resin (lbs/ft)
100%	5.58	0.12	0.47	5.79	0.00	0.92	0.66
95%	14.17	0.17	0.67	8.67	1.23	2.44	0.99
75%	48.52	0.36	1.48	20.18	15.65	8.53	2.31
55%	88.11	0.62	2.53	35.72	29.96	15.32	3.96
45%	117.86	0.78	3.17	46.84	31.03	31.03	5.01
35%	156.34	0.94	3.81	58.76	32.81	54.03	6.00
25%	205.03	1.06	4.33	70.15	36.05	86.63	6.81
15%	231.72	1.04	4.23	72.42	67.10	80.17	6.76
5%	324.21	0.89	3.63	54.89	259.80	0.00	5.00
Weight (lbs)	19358						

	Gel Coat	Mat	DB Glass	Spar Cap +TE	Balsa	Plexus/ Resin
Weight of Material	106	433	6592	6468	5096	674
Percent of Blade Weight	1%	2%	34%	33%	26%	3%
Cost per Pound	$1.88	$1.05	$1.09	$1.10	$2.24	$4.00
Material Cost	$200	$453	$7,173	$7,138	$11,438	$2,695
Percent of Blade Shell Cost	1%	2%	25%	25%	39%	9%
					Total Cost of Blade Shell Materials	$29,096

4.2 Blade Skin Molding

4.2.1 Laminate Impregnation Approach

Wet lay-up is the most common approach used for the lamination of industrial composites. This approach has been widely applied in wind blade manufacturing but has declined over time because of several disadvantages. Wet-layup has traditionally been performed by hand application of the resin to the fabric. This requires considerable worker skill to obtain consistent resin ratios and is difficult to control in volume manufacturing. Laminate impregnation provides an improved approach because the quantity of resin is controlled by machine.

An outline of blade component manufacturing using the laminate impregnation process is provided in Figure 4.4. The process begins by preparing tooling and fabrics for lamination, followed by fabric impregnation with metered quantities of resin. The wet fabric is placed in the mold, rolled flat, and covered with peel ply and a vacuum bag. After curing the laminate under vacuum pressure the bag is removed and the components are ready for bond assembly into the complete blade structure.

Knight & Carver has experience using an epoxy impregnator which can efficiently deliver fiberglass fabric widths varying from 457 mm to 1500 mm (18" to 60") in width (Figure 4.5). Depending on the materials used, the impregnator can produce laminates with glass content up to 55% by weight. Each laminate layer is wetted, placed in the mold, and rolled flat. Once the lamination is completed the laminate is sealed with a vacuum bag and cured under atmospheric pressure in a heated mold. This approach can also be applied to the manufacturing of large wind blades using a bridge crane as shown in Figure 4.6.

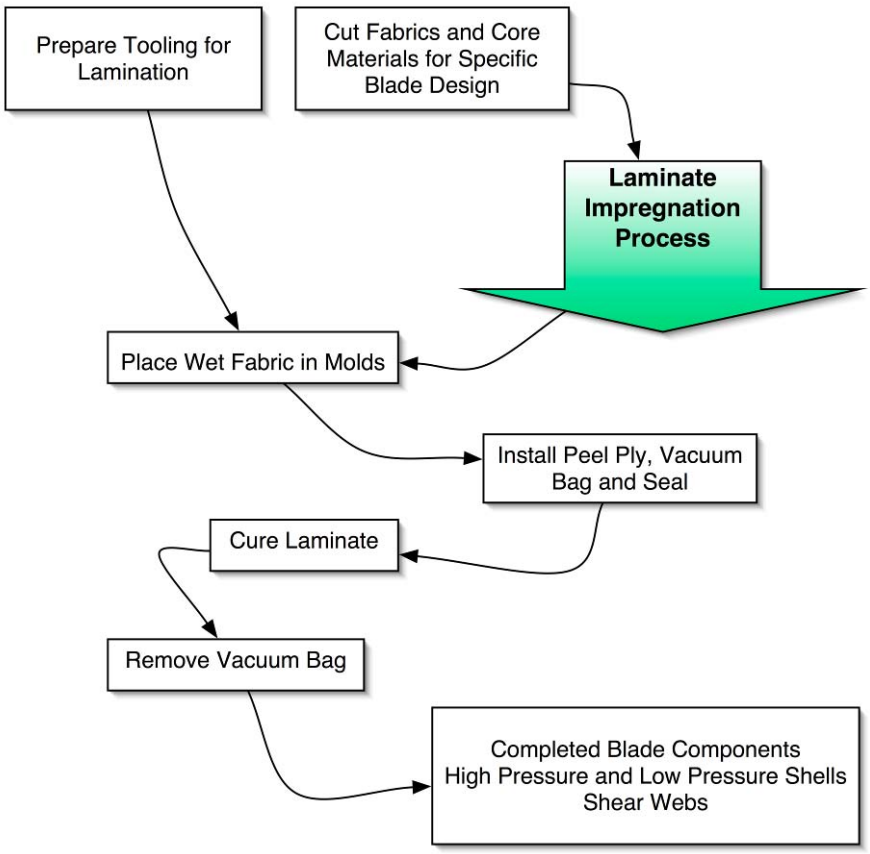

Figure 4.4 Outline of blade component manufacturing using laminate impregnation.

Figure 4.5 Laminate impregnator located at Knight & Carver.

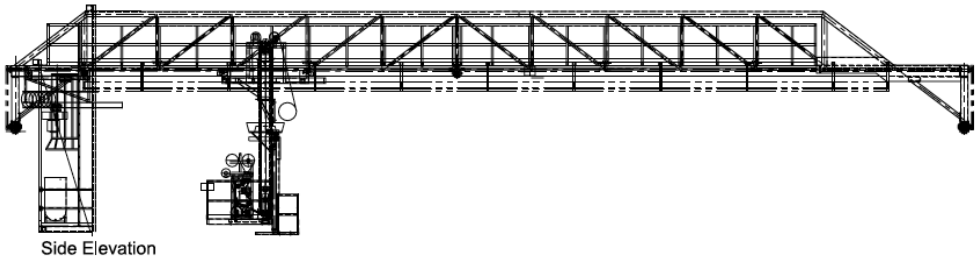

Figure 4.6 Schematic drawing of a bridge crane laminate impregnator.

The advantages of the laminate impregnation process are consistent resin-to-glass ratios and the assurance that fabrics are properly wetted before lamination. In addition, rolling of individual wetted fabric layers provides assurance the laminate is free of ripples or waves. Wetted fabrics, unlike dry fabrics, have considerable resistance to movement after placement due to the tackiness of the resin. Disadvantages of this approach are limitations on working time and worker exposure to wet resins. Skin exposure to epoxy resins is a particular concern and substantial measures must be used to prevent direct contact with these materials. Figure 4.7 shows the outer skin laminations in the blade mold and Figure 4.8 shows the core materials being placed over the outer skin.

Figure 4.7 Photograph showing outer skin laminations in the blade mold.

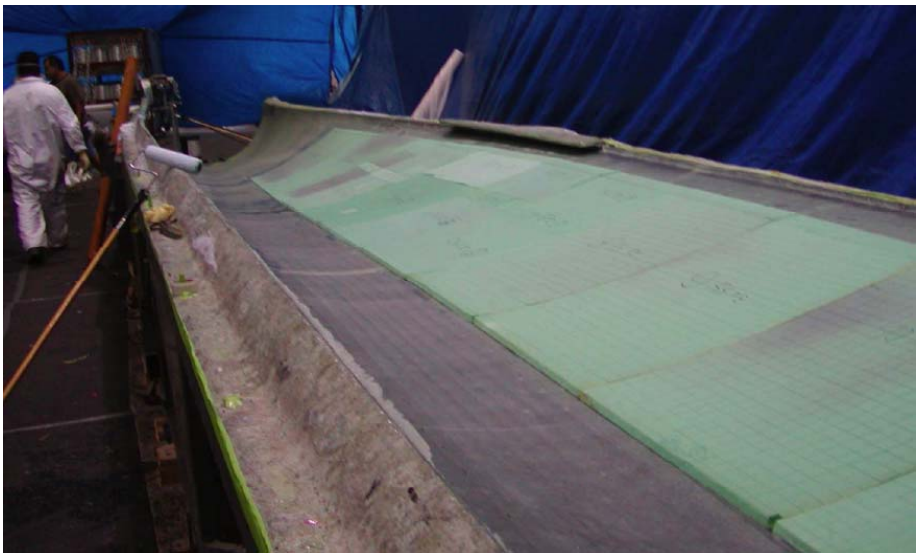

Figure 4.8 Photograph showing foam core material placed over the outer skin laminations.

4.2.2 Vacuum Infusion Process

Vacuum infusion is a process which uses atmospheric pressure to introduce liquid resin into dry fiber reinforcement. This technology has become more prevalent in the manufacture of large fiberglass components in recent years and is finding widespread usage in wind turbine blades. The maximum working pressure is 1 bar (14.7 psi), since the process relies upon a vacuum. Other processes, such as Resin Transfer Molding, can use higher working pressures and more viscous resins. For vacuum infusion it is important to use low viscosity resin formulations. Suppliers can now provide suitable viscosity resins in polyester, vinylester, and

epoxy. As an example Jeffco Products 1401-21T epoxy system has a viscosity of 350 cps at 77° working temperature, which is appropriate for wet-layup. A less viscous fluid is needed for infusion and the Jeffco 1401-21 epoxy system with a viscosity of 160 cps is an example.

Proper infusion also requires a perfect vacuum seal throughout the part. Achieving a complete vacuum is critical because leaks in the system can result in voids or dry spots. Design of the mold tooling can incorporate wide flanges and other features to simplify sealing the vacuum bag to the mold. If the seal is proper the vacuum pump will remove all the air from the dry fabric before the resin is introduced. This results in excellent laminate quality, consistent fiber-to-resin ratios, and a highly repeatable manufacturing process. The basic stages of wind blade manufacturing with vacuum infusion are presented in Figure 4.9.

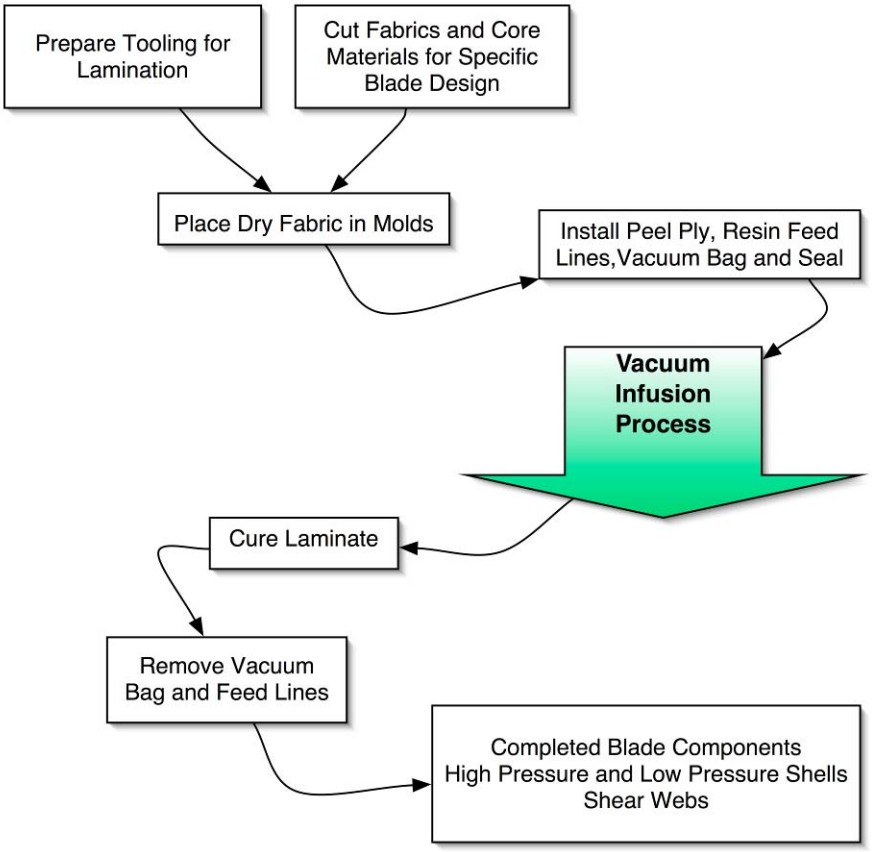

Figure 4.9 Outline of blade component manufacturing using vacuum infusion.

Designing the resin distribution network is a key consideration in the development of vacuum infused parts. The resin is usually delivered at several locations in the tooling and pushed by atmospheric pressure toward the vacuum port. As the resin travels through the dry laminate it wets the fabric and gradually seeps through the material. A number of techniques are used to aid in resin movement including surface media, coring channels, and interlaminar feed layers. Surface media placed under the vacuum bag permit large amounts of resin to be distributed over a large flow front. Scoring grooved channels in the core materials is another way to simply transport resin over large surfaces. Core channel infusion allows the design to include

resin feed channels in different sizes and flow directions. Interlaminar media distribute resin through a porous layer in the laminate. A disadvantage of this technique is the high resin content of the feed layer.

Key advantages of vacuum infusion are a decrease in labor costs, greatly reduced worker exposure to resins, and control of volatile organic compounds (VOCs). All fabrics remain dry when placed in the mold and there is no need to complete lamination in a specified time window. Working with dry fabric simplifies the process of fabric placement, especially in large blades (Figure 4.10). Infusion takes places in a single step, so secondary bonding for that part is also eliminated. Compaction of the dry fabrics is completed during the initial vacuum stage, prior to resin introduction and does not require workers to roll individual layers.

Figure 4.10 Placement of dry fabric in the blade shell mold (LM Glasfiber photograph).

The disadvantages of vacuum infusion are the potential for local voids or dry spots due to vacuum leaks or improper resin distribution. Dry spots cannot be identified by visual inspection if the parts are fabricated with a colored gelcoat in the mold, but use of a clear gelcoat will allow inspection and repair. Another potential problem occurs when fabric layers compress during vacuum infusion. Dry fabrics in thick regions of laminate may shift and develop folds or ripples during compaction. The presence of folds in the fibers can result in significant losses in laminate fatigue strength, but are not easily identified by inspection using non-destructive test methods.

4.2.3 Pre-Preg Materials

Pre-preg materials have the resin added to the fabric at the material supplier. After the fabric is impregnated the resin is stabilized for storage and handling. Pre-preg materials have been widely used in aerospace and offer excellent physical properties. This material has proven to be a commercially viable means to construct wind turbine blades, usually for lightweight skin panels. Pre-preg fabrics do not drape easily in the molds and can require vacuum de-bulking operations to compress them into position. Pre-preg materials also require mold heating or

autoclaves to cure the laminates. The high cost of the materials and the additional cost of handling and storing the materials limit its application in large wind blades.

4.2.4 Resin Film Infusion

Resin film infusion (RFI) offers many of the same benefits and disadvantages as pre-preg materials for fabrication of wind turbine blades. In this process the resin is applied in thin film in much the same way as would have to take place for pre-preg. Even though the material costs of RFI are less than pre-preg, they are still higher than that of resin infusion. RFI does not have the same problems in placement of the laminate, but cutting and forming the resin film correctly creates additional work during blade manufacturing. Finally, the need to heat the mold to higher temperatures and the higher cost of materials limit the application of this technique for wind turbine blade fabrication.

4.3 Bond Assembly

After lamination the blade components are bonded together to form the final blade assembly. There is typically an adhesive joint near the leading and trailing edges of the blade shells. Final blade assembly has many challenges which must be overcome to achieve a durable product. When bonding blade components during final assembly the critical factors are bond line thickness and adhesive contact area. Adhesives perform best when the bond line is relatively thin. A bond line thickness of 3 to 4 mm is considered to be ideal, although toughened epoxy adhesive can allow bond thickness to as much a 15 mm. When the bond thickness exceeds design tolerances, the quantity of adhesive applied to the surface may be insufficient to completely cover the intended bond surface. This sometimes leads to an incomplete bond or voids within the adhesive. Even if full contact is achieved, the bond can be weakened by excessive adhesive thickness.

The shear webs or spar are typically bonded into one blade half first in an open mold as shown in Figure 4.11. This provides easy access to assure that that bond line thickness is correct and full adhesive coverage is achieved. It is desirable to first bond the shear webs to the downwind, or low pressure, blade shell. The low pressure shell is typically loaded in compression and its bond to the shear web is critical to prevent panel buckling failure. A trial fit can be made prior to performing the final assembly of the upwind, or high pressure, blade shell. Clay balls can be placed on bond areas and the mold closed. When opened, the clay can be examined to determine the bond line thickness in those areas. If the bond line exceeds tolerances, additional laminate can be applied before bonding to decrease the bond line thickness. Trial fits also provide valuable data that can be used for tooling adjustment to improve tolerances over time.

Figure 4.11 Bond assembly of the KC-51 blade at Knight & Carver in San Diego.

With large wind turbine blades the issue of handling the parts becomes more important. Blade shells must be well supported during assembly and shear webs may need some support for handling. Reinforced lifting points need to be determined to not only handle the weight of the part without damage, but to balance it for easy assembly. Removing the blade shells from the mold and placing them in a separate bonding fixture is not practical if there is a chance of damaging the part. In large wind blades the shells are usually left in the mold which becomes part of the bonding fixture.

If the blade shells are left in the mold, then fixtures are needed to assure the shell remains properly seated as the mold is rotated 180° into the bonding position. Special hinges can be made which allows one half of the mold to be rolled to the other. Once in place, an overhead crane can be used to lift the mold and flip it over. More sophisticated turning fixtures can be used that hydraulically turn the mold half and lower it onto the other side. When using this method, the blade half molds have alignment pins that ensure that the blade halves are fitting properly. Spacer blocks are also used to achieve the proper bond line at the leading and trailing edges. The blade halves then need to be held together until the adhesive is cured. Once the adhesive has cured, the blade must be de-molded (Figure 4.12) and the tools prepared for the next molding cycle.

Figure 4.12 Photograph of a cured blade during the demolding process.

4.4 Fastener Installation

Fastener installation is often completed after bond assembly. With directly embedded threaded inserts, this step will be used to machine flat surfaces on each of the inserts that were installed during lamination. It is also possible to bond threaded inserts after bond assembly has been completed into molded cavities or drilled holes. T-bolt installation also involves drilling holes during this phase of blade manufacturing, as shown in Figure 4.13. Typically drilling operations are completed by specially designed machines which drill two or more holes at a time. Care is needed to align the blade axes and the location of the drilled holes is critical for proper blade assembly.

Figure 4.13 Photograph of the blade root drilling for T-bolt fasteners.

4.5 Blade Finishing

Blade finishing operations commence after the blade has been assembled and the adhesive is allowed to cure. The finishing work typically includes cleaning excess adhesive from the blade, adding additional laminate over the joints to assure strength, preparing blade surfaces, and fairing the trailing edge to minimize noise. Specialized tools for moving and turning the blades are used during this stage of manufacturing. A photograph of large wind turbine blades in the finishing hall of an LM Glasfiber facility is presented in Figure 4.14.

Blade surface coatings include colored gelcoat or paint. Field experience has shown that gelcoats have performed less well than paint as a surface coating for wind blades. This is because polyurethane paints are significantly more flexible than gelcoat and are resistant to micro-cracking. When gelcoat is used, it provides a finished surface to the blade and it is ready when pulled from the mold.

An improved, albeit more costly, approach is to apply a clear gelcoat to the mold before laminating. This allows visual inspection of the laminate and identification of surface defects, including small voids and pin holes. The blade is then washed with a solution to remove mold contaminates and sanded. At this time a thorough inspection takes place and any defects can be repaired. The blade is then painted with an appropriate paint selected for ultra violet (UV) protection and weather resistance. Finally, protection to the leading edge can be accomplished by applying a polyurethane tape or other abrasion resistant coating that is bushed, rolled or sprayed on. When complete the lightning system is checked to make sure that there is continuity and that the receptors are free of paint and the paint edge is tapered.

Figure 4.14 Large wind blades in the finishing hall (LM Glasfiber photograph).

4.6 Balancing

Wind turbine rotor blades are typically balanced in sets to specific tolerances determined in the design. The key parameters for balancing the rotor are the mass (kg) and the center of gravity (m) of each blade. The static moment is calculated as the product of the mass and the center of gravity (kg-m). With good manufacturing control of laminates, resin and adhesive the standard deviation before balancing can be 2% or less. Usually the blades are balanced so that the difference in static moment between any two blades in a rotor set is within a tolerance of 0.5%. Balance weights are typically added to adjust the mass and static moment of two blades to match the heaviest in the set, within given tolerances for the design.

Several approaches to blade balancing are used in the wind industry. One method is to determine the amount of weight needed at the factory but add the weight after the rotor is installed. A weight is pre-made to the correct size and lowered into the blade after adhesive is applied, from the root when the blade is in the down position. This allows the weight to be almost any size without worry of damage to the blade. More common is a “balance box” which is a hollow that is built into the blade capable of carrying the maximum weight allowed. After weighing the blades, a hole is drilled into the balance box of the blades needing weight and a mixture of lead shot and epoxy is injected to achieve the correct balance. The hole is then patched and touched up. On the root end of the blade another balance box can be built in. Another approach at the root is to laminate bars in place. Final weight checks will verify that the balance is within specifications.

Once blade balancing has been completed the blade are moved outside and readied for transportation, as shown in Figure 4.15.

Figure 4.15 Blade storage in preparation for shipment (LM Glasfiber photograph).

4.7 Transportation

Transportation of wind turbine blades presents unique challenges. The size and shape of these large, relatively fragile objects are unique. Blade skins are relatively thin, so protective fiberglass lifting covers are often used to protect the blade at lifting locations. Blade tips and trailing edges are particularly vulnerable to damage during transport. Tip covers prevent damage to the delicate trailing edge, spread the load over a large area, and are placed at predetermined positions to balance the load.

Special racks that hold the blades are located at the outboard area of the blade. The root is bolted to a stand or rack that secures the root. Special care is give to the tips so that vibration does not set the blades moving and damage them. Some blades sensitive to edgewise loading are shipped flat, while the more robust are shipped with the leading edge down.

Blades are usually shipped by rail or truck. Shipping by truck requires special care to assure the blade cargo is within limitations for weight, height, width, and length. Height limitations are typically the most inflexible restriction. Blades must be placed on a truck so that the maximum height does not exceed 13.5 feet or 14 feet. Width restrictions also need to be followed or special permits are needed. Any blade over 55 feet in length requires a special permit. These permits can double the shipping cost in some cases where a pilot car is needed. Stretch trailers can handle blades up to about 30 meters in length without issues and can carry multiple blades on the trailer as shown in Figure 4.16.

Figure 4.16 Loading wind blades for transportation at Knight & Carver in San Diego.

Wind blades for multi-megawatt class machines must be shipped with a single blade per truck, as shown in Figure 4.17. Truck transportation of wind turbine blades becomes impractical for blade lengths greater than about 55 meters.

Figure 4.17 Transportation of a large wind turbine blade (LM Glasfiber photograph).

Rail transportation is a good option for long distances. Trains can handle 40 m blades with no trouble by employing idler cars between the cargo cars. Trains can eliminate the high cost of permits or other trucking limitations, but most blades will be loaded on trucks at some point to reach the site. The use of rail transport requires additional loading and unloading operations that add significant costs and increase the potential for blade damage. Every blade must be analyzed for the best loading and shipping method.

5 STAR BLADE DESIGN

5.1 Aerodynamic Performance

5.1.1 Blade Section Shapes

A series of airfoils were developed for this project to provide the initial section shapes for the blade. These airfoils are derived from those designed by Wortmann in the late 1970s and compiled by Althaus [3]. We changed the geometry of these airfoils and decided to rename them with the new designation being STAR-xxxx-yyyy where xxxx represents the maximum thickness to chord ratio t/c × 100% and yyyy the trailing edge thickness to chord ratio $t_{te}/c \times 100\%$. (Note: Ultimately the inboard section of the prototype blade was based upon the DU airfoil series used in the Euros EU-51 blade.)

The STAR series airfoil family was prepared especially for this blade development project. Seven airfoil sections from the STAR series are shown in Figure 5.1. The tip airfoil STAR-1520-0018 has a t/c = 15.2% and a t_{te}/c = 0.18% and it was derived from the sharp trailing edge FX79-W-151a. The main outboard airfoil STAR-1700-0021 has a t/c = 17.0% and a t_{te}/c = 0.21% and it was derived from the STAR-1520-0018. The mid airfoil STAR-2615-0123 has a t/c = 26.15% and a t_{te}/c = 1.23% and it was derived from the FX77-W-258. The inboard airfoils STAR-3500-0545 (t/c = 35.0% and a t_{te}/c = 5.45%) and STAR-4000-0621 (t/c = 40.0% and a t_{te}/c = 6.21%) were derived from the FX77-W-270.

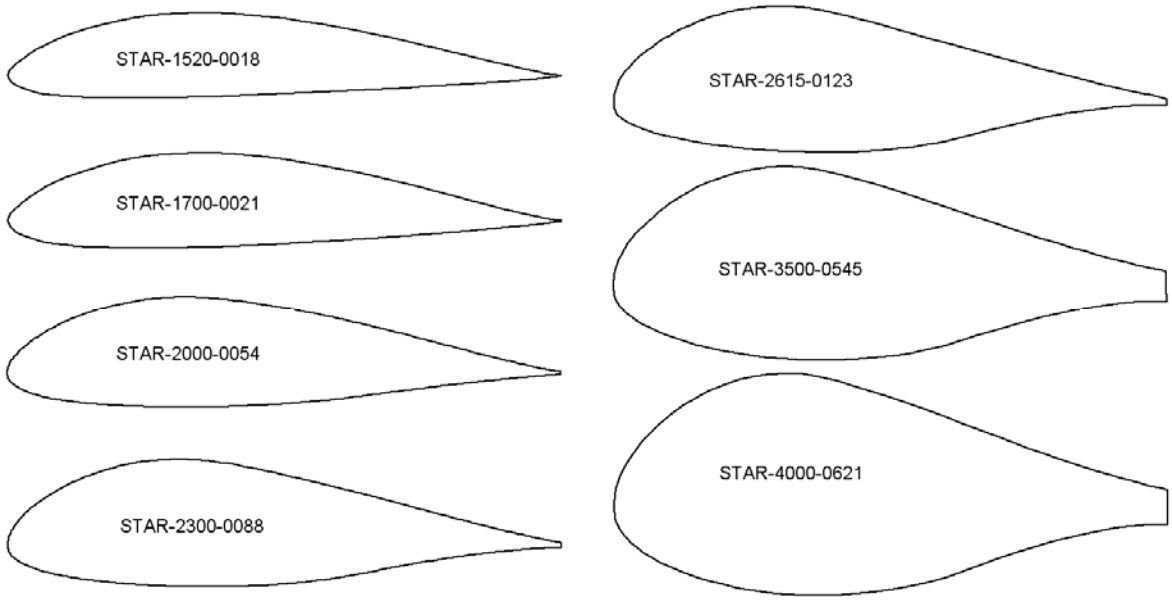

Figure 5.1 STAR Series Airfoil Family

5.1.2 Section Performance Characteristics

Figure 5.2 presents the predicted performance characteristics of the STAR-1520-0018 airfoil at Re = 3.0 million for clean and soiled surface conditions, with the latter simulated by fixing

transition at 2% of chord on the suction side and 5% of chord on the pressure side. The simulations for the STAR airfoil series were performed with the viscous-inviscid airfoil analysis method MSES [4,5]. The lift characteristics of this airfoil are mostly unaffected by surface soiling except for the nonlinear lift effect caused by a laminar bubble near the leading edge of the suction surface which disappears when transition is fixed near the leading edge. Both the lift coefficient at $\alpha = 0^{\circ}$, c_{l_o}, and the maximum lift coefficient, $c_{l_{max}}$, are unaffected by surface soiling. At clean and soiled surface conditions it generates a $(c_l/c_d)_{max}$ = 168.8 and 82.4, respectively. In Figure 5.3, the performance characteristics of the STAR-1520-0018 are compared against those of the published, high performance S831, airfoil. Both airfoils have a nearly identical $c_{l_{max}}$ with the S831 showing more lift loss due to soiling in the linear regime. At clean conditions the $(c_l/c_d)_{max}$ = 223.0 of the S831 is much higher than the $(c_l/c_d)_{max}$ = 168.8 of the STAR-1520-0018. However, this ranking reverses at soiled surface conditions with the $(c_l/c_d)_{max}$ = 82.4 of the STAR-1520-0018 and $(c_l/c_d)_{max}$ = 63.0 of the S831.

Figure 5.4 presents the performance characteristics of the STAR-1700-0021 at Re = 3.0 million and clean and soiled surface conditions. The lift characteristics of this airfoil are similar to those of the STAR-1520-0018. Again lift is mostly unaffected by surface soiling except for the bubble-induced nonlinear lift which disappears when transition is fixed near the leading edge. Both c_{l_o} and $c_{l_{max}}$ are unchanged by surface soiling. At clean and soiled surface conditions it generates a $(c_l/c_d)_{max}$ = 166.9 and 79.7, respectively. In Figure 5.5, the performance characteristics of the STAR-1700-0021 are compared against those of the S830. Both airfoils have a nearly identical $c_{l_{max}}$ and $(c_l/c_d)_{max}$ values at clean and soiled conditions.

With a thickening of the airfoil, the insensitivity of lift to surface soiling tends to disappear. Figure 5.6 presents the performance characteristics of the STAR-2615-0123 at Re = 3.0 million and clean and soiled surface conditions. Now lift is affected by surface soiling with $c_{l_{max}}$ decreasing from 2.25 to 1.27 as a result of surface soiling. At clean and soiled surface conditions the STAR-2615-0123 generates a $(c_l/c_d)_{max}$ = 170.6 and 65.7, respectively.

Figure 5.7 presents the performance characteristics of the STAR-3500-0545 at Re = 3.0 million and clean and soiled surface conditions. For this 35% thick airfoil, lift is severely affected by surface soiling with $c_{l_{max}}$ decreasing from 2.09 to 1.0 as a result of surface soiling. At clean and soiled surface conditions it generates a $(c_l/c_d)_{max}$ = 123.2 and 43.1, respectively.

Figure 5.8 presents the performance characteristics of the STAR-4000-0621 at Re = 3.0 million and clean and soiled surface conditions. Again lift is severely affected by surface soiling with $c_{l_{max}}$ decreasing from 1.89 to 0.7 as a result of surface soiling. At clean and soiled surface conditions it generates a $(c_l/c_d)_{max}$ = 113.4 and 29.0, respectively.

In conclusion, five airfoils shapes were developed for the proposed blades. The two outboard airfoils are roughness insensitive in terms of their lift characteristics and show a reasonable balance between lift-to-drag ratio at clean and soiled conditions. The mid and two inboard section shapes show significantly degraded lift performance at soiled conditions.

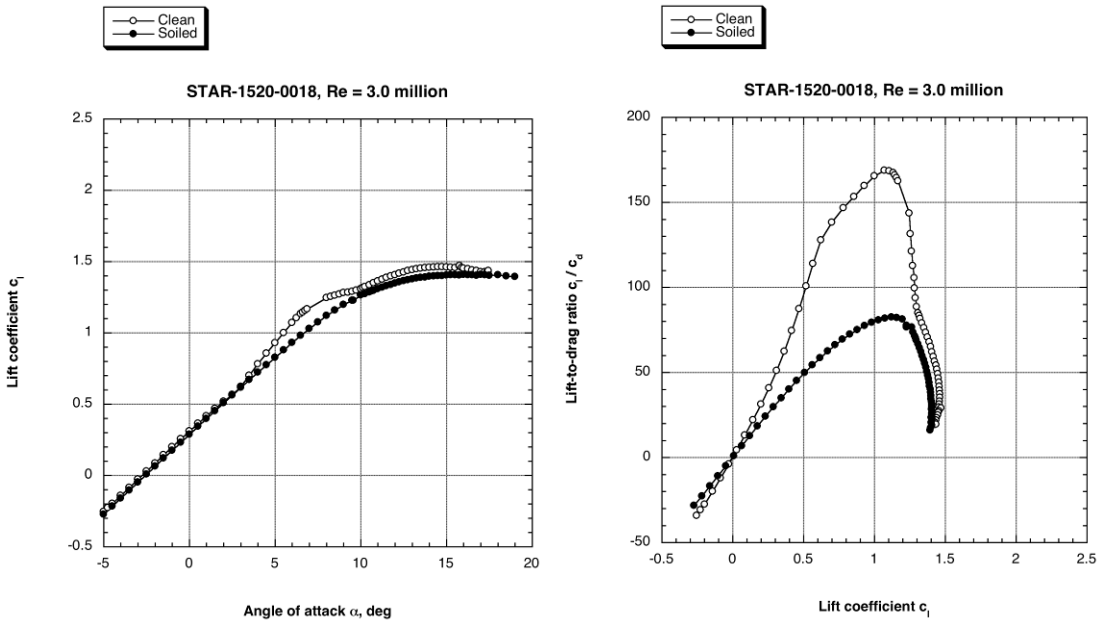

(a) Lift curve (b) Drag polar

Figure 5.2 Performance characteristics of the STAR-1520-0018 at clean and soiled (transition fixed at suction side $x_{tr}/c = 0.02$, pressure side $x_{tr}/c = 0.05$) surface conditions and Re = 3.0 million.

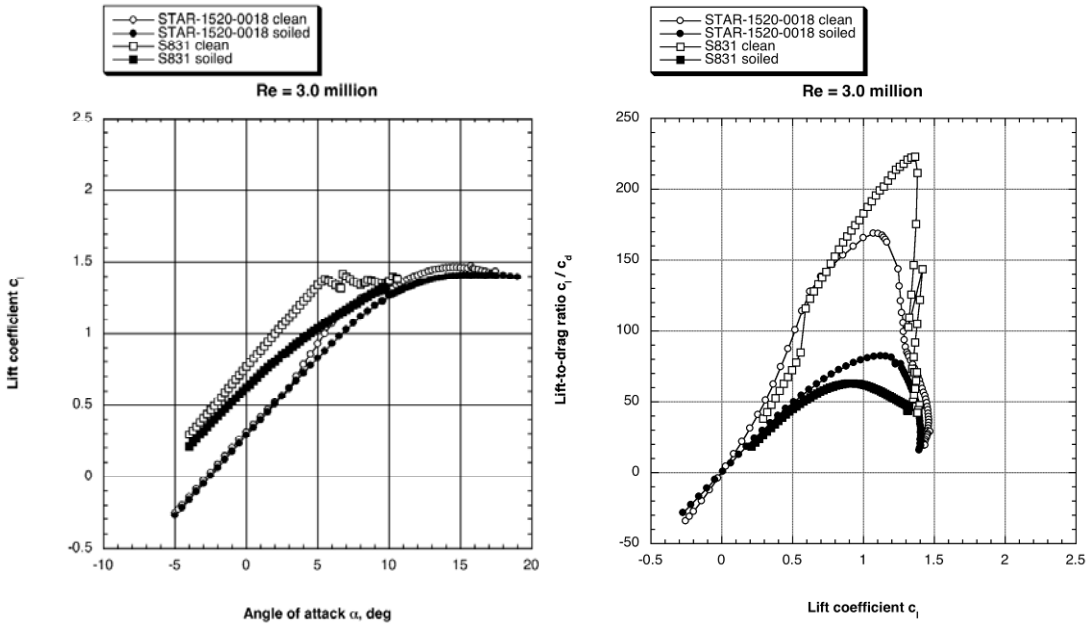

(a) Lift curve (b) Drag polar

Figure 5.3 Comparison of performance characteristics of the STAR-1520-0018 and the S831 at clean and soiled (transition fixed at suction side $x_{tr}/c = 0.02$, pressure side $x_{tr}/c = 0.05$) surface conditions and Re = 3.0 million.

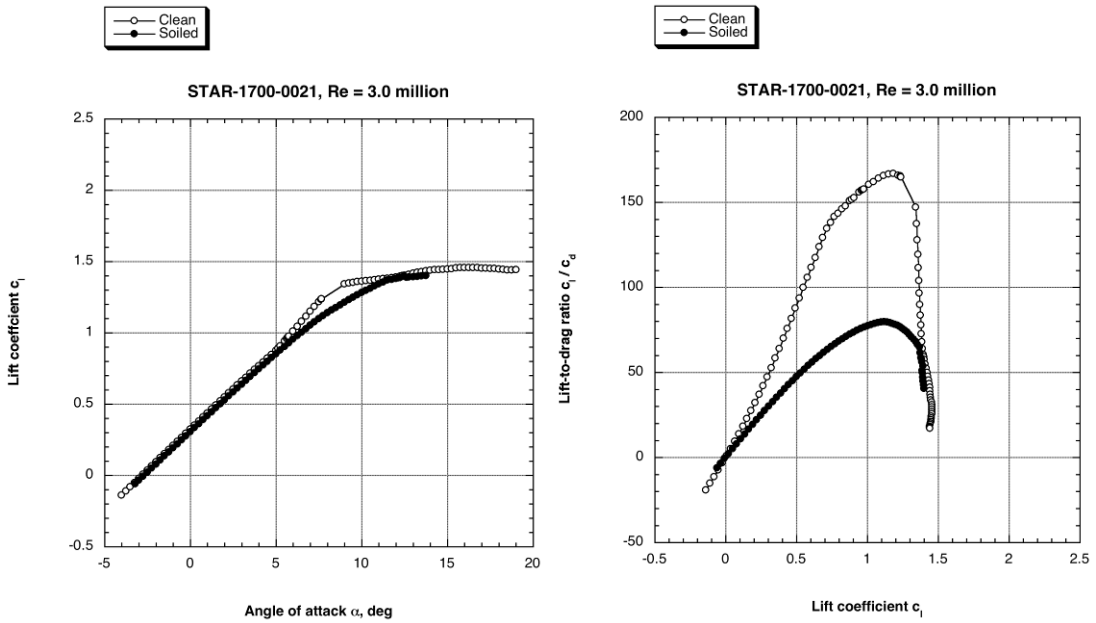

(a) Lift curve (b) Drag polar

Figure 5.4 Performance characteristics of the STAR-1700-0021 at clean and soiled (transition fixed at suction side $x_{tr}/c = 0.02$, pressure side $x_{tr}/c = 0.05$) surface conditions and Re = 3.0 million.

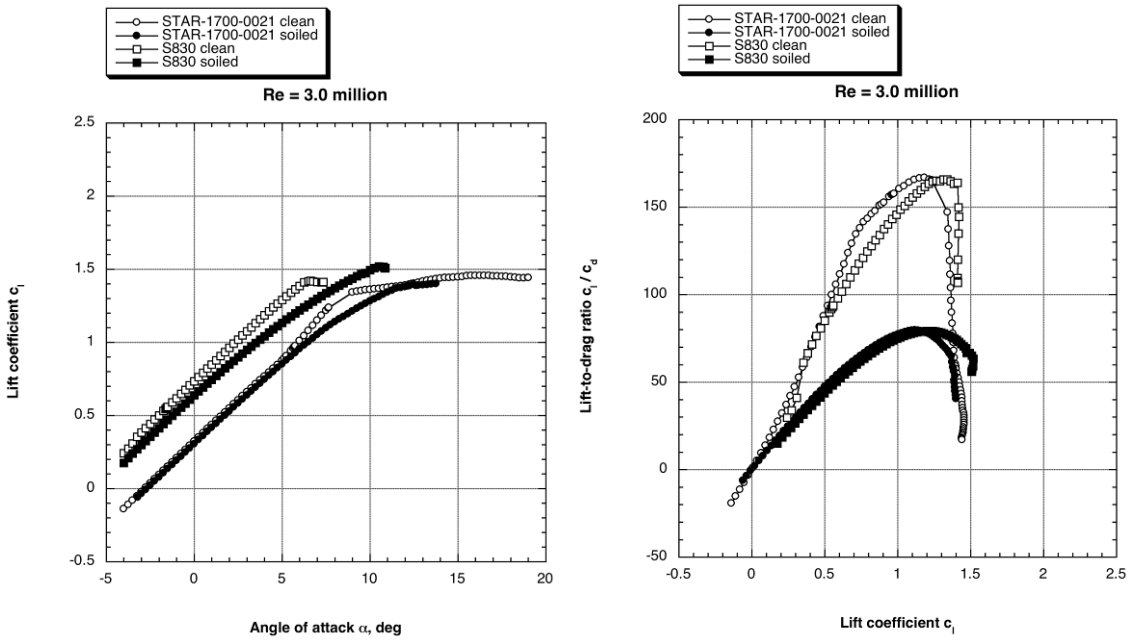

(a) Lift curve (b) Drag polar

Figure 5.5 Comparison of performance characteristics of the STAR-1700-0021 and the S830 at clean and soiled (transition fixed at suction side $x_{tr}/c = 0.02$, pressure side $x_{tr}/c = 0.05$) surface conditions and Re = 3.0 million.

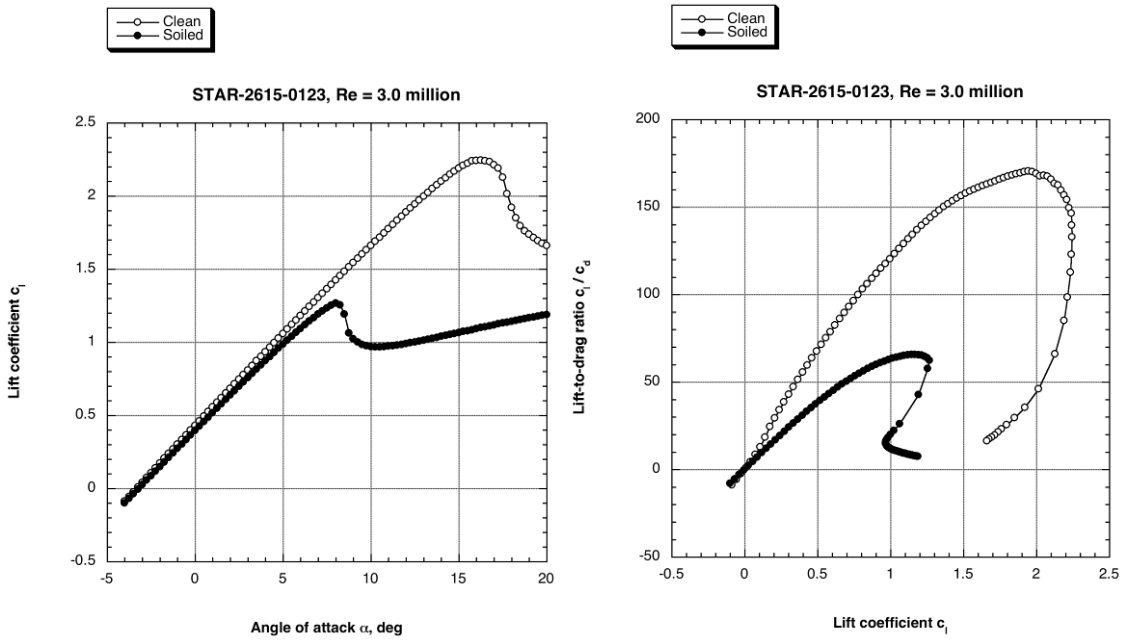

(a) Lift curve (b) Drag polar

Figure 5.6 Performance characteristics of the STAR-2615-0123 at clean and soiled (transition fixed at suction side $x_{tr}/c = 0.02$, pressure side $x_{tr}/c = 0.05$) surface conditions and Re = 3.0 million.

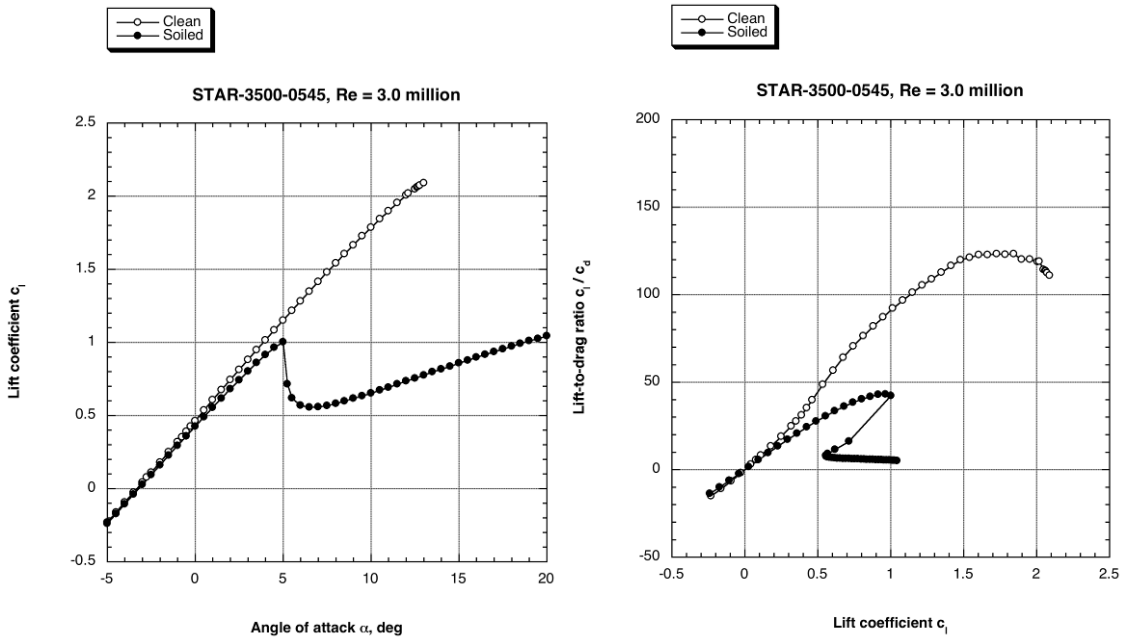

(a) Lift curve (b) Drag polar

Figure 5.7 Performance characteristics of the STAR-3500-0545 at clean and soiled (transition fixed at suction side $x_{tr}/c = 0.02$, pressure side $x_{tr}/c = 0.05$) surface conditions and Re = 3.0 million.

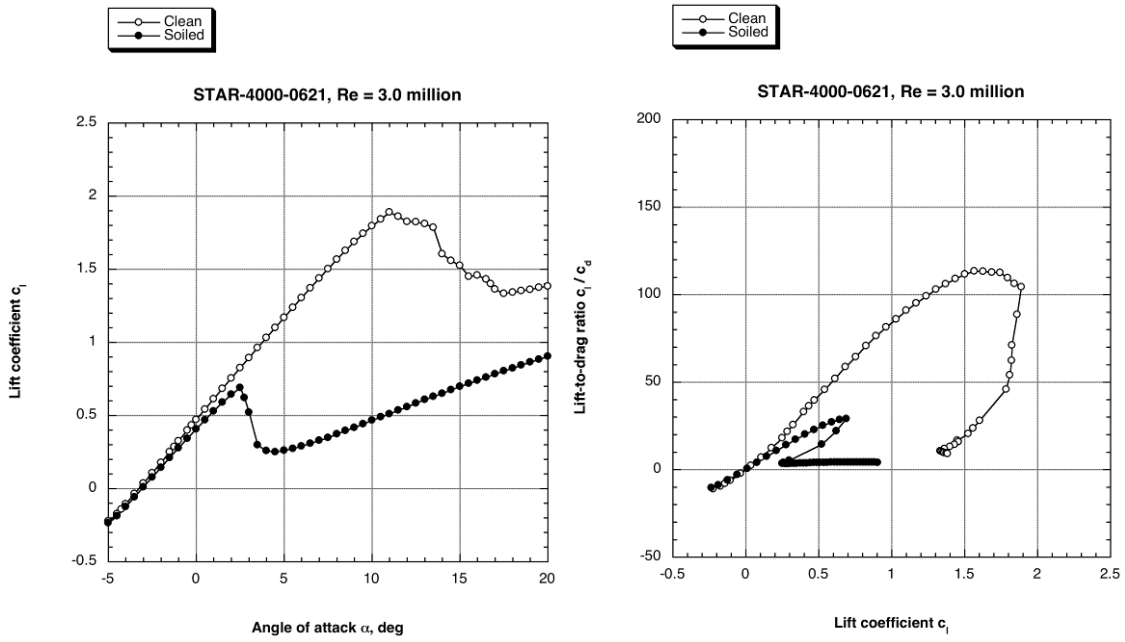

(a) Lift curve (b) Drag polar

Figure 5.8 Performance characteristics of the STAR-4000-0621 at clean and soiled (transition fixed at suction side $x_{tr}/c = 0.02$, pressure side $x_{tr}/c = 0.05$) surface conditions and Re = 3.0 million.

5.1.3 Summary of Airfoil Characteristics

The airfoil lift characteristics of the STAR airfoils were estimated for free and fixed transition using representative Reynolds numbers identified. Lift, drag, and pitching moment coefficients were calculated at a variety of angles of attack. These data are summarized in tabular form as a function of thickness ratio in Table 5.1 for free transition (clean airfoil) and Table 5.2 for fixed transition (soiled airfoil).

The airfoil section data are plotted in Figure 5.9 for clean conditions and Figure 5.10 for soiled conditions for thicknesses up to 23%. The drag characteristics are presented in Figures 5.11 and 5.12. The airfoil efficiency (lift-to-drag ratio, L/D) is presented in Figures 5.13 and 5.14 for clean and soiled conditions.

The lift characteristics of the STAR airfoils are insensitive to the effects of roughness up to thickness ratios of 20%. These airfoil sections also have desirable structural and manufacturing characteristics.

Table 5.1 STAR Series Airfoil Characteristics Assuming Clean Surfaces

Lift Coefficient / Free Transition / Clean

Alpha	15.2%	17.0%	20.0%	23.0%	26.2%	35.0%	45.0%
Re	3.0E+06	3.0E+06	5.6E+06	5.0E+06	5.6E+06	3.0E+06	4.5E+06
-4.00	-0.14	-0.14	-0.13	-0.10	-0.08	-0.09	-0.09
-3.00	-0.03	-0.02	0.00	0.02	0.04	0.04	0.02
-2.00	0.09	0.09	0.12	0.14	0.17	0.18	0.17
-1.00	0.20	0.21	0.24	0.27	0.31	0.32	0.31
0.00	0.31	0.32	0.36	0.40	0.44	0.46	0.46
1.00	0.42	0.44	0.48	0.52	0.56	0.61	0.60
2.00	0.52	0.55	0.60	0.65	0.69	0.74	0.74
3.00	0.62	0.66	0.72	0.77	0.82	0.88	0.88
4.00	0.78	0.77	0.84	0.89	0.94	1.02	1.03
5.00	0.93	0.88	0.96	1.02	1.07	1.15	1.17
6.00	1.07	1.01	1.08	1.14	1.20	1.28	1.30
7.00	1.18	1.15	1.20	1.26	1.32	1.41	1.44
8.00	1.25	1.26	1.31	1.38	1.44	1.54	1.57
9.00	1.28	1.34	1.42	1.50	1.56	1.67	1.68
10.00	1.31	1.36	1.53	1.61	1.68	1.79	1.78
11.00	1.36	1.38	1.61	1.72	1.80	1.90	1.75
12.00	1.41	1.39	1.66	1.82	1.91	2.01	1.74
13.00	1.44	1.42	1.67	1.91	2.02	1.88	1.73
14.00	1.46	1.44	1.67	1.96	2.12	1.91	1.70
15.00	1.46	1.45	1.66	1.94	2.21	1.83	1.45

Drag Coefficient / Free Transition / Clean

Alpha	15.2%	17.0%	20.0%	23.0%	26.2%	35.0%	45.0%
Alpha	3.0E+06	3.0E+06	5.6E+06	5.0E+06	5.6E+06	3.0E+06	4.5E+06
-4.00	0.0071	0.0072	0.0074	0.0082	0.0092	0.0145	0.0145
-3.00	0.0069	0.0070	0.0071	0.0079	0.0085	0.0139	0.0171
-2.00	0.0066	0.0068	0.0069	0.0073	0.0075	0.0135	0.0147
-1.00	0.0064	0.0065	0.0065	0.0065	0.0062	0.0129	0.0131
0.00	0.0061	0.0061	0.0061	0.0060	0.0062	0.0117	0.0119
1.00	0.0056	0.0058	0.0057	0.0061	0.0064	0.0107	0.0115
2.00	0.0052	0.0055	0.0057	0.0063	0.0065	0.0106	0.0117
3.00	0.0049	0.0053	0.0058	0.0065	0.0067	0.0107	0.0118
4.00	0.0053	0.0054	0.0060	0.0067	0.0069	0.0110	0.0118
5.00	0.0058	0.0058	0.0062	0.0069	0.0071	0.0114	0.0120
6.00	0.0063	0.0063	0.0064	0.0071	0.0073	0.0118	0.0122
7.00	0.0073	0.0069	0.0067	0.0074	0.0076	0.0121	0.0127
8.00	0.0087	0.0079	0.0072	0.0078	0.0080	0.0127	0.0133
9.00	0.0121	0.0091	0.0077	0.0081	0.0082	0.0136	0.0146
10.00	0.0154	0.0122	0.0085	0.0085	0.0086	0.0145	0.0164
11.00	0.0185	0.0165	0.0100	0.0093	0.0090	0.0158	0.0225
12.00	0.0227	0.0218	0.0126	0.0103	0.0095	0.0169	0.0294
13.00	0.0279	0.0271	0.0167	0.0119	0.0102	0.0235	0.0367
14.00	0.0350	0.0333	0.0231	0.0144	0.0114	0.0290	0.0466
15.00	0.0442	0.0351	0.0272	0.0200	0.0131	0.0453	0.0775

Moment Coefficient / Free Transition / Clean

Alpha	15.2%	17.0%	20.0%	23.0%	26.2%	35.0%	45.0%
Re	3.0E+06	3.0E+06	5.6E+06	5.0E+06	5.6E+06	3.0E+06	4.5E+06
-4.00	-0.0523	-0.0506	-0.0475	-0.0442	-0.0389	-0.0266	-0.0266
-3.00	-0.0526	-0.0520	-0.0494	-0.0460	-0.0429	-0.0335	-0.0138
-2.00	-0.0530	-0.0533	-0.0515	-0.0483	-0.0478	-0.0403	-0.0289
-1.00	-0.0532	-0.0545	-0.0536	-0.0508	-0.0537	-0.0479	-0.0418
0.00	-0.0531	-0.0557	-0.0559	-0.0532	-0.0572	-0.0573	-0.0541
1.00	-0.0522	-0.0568	-0.0583	-0.0556	-0.0605	-0.0661	-0.0642
2.00	-0.0504	-0.0578	-0.0607	-0.0579	-0.0639	-0.0731	-0.0733
3.00	-0.0488	-0.0584	-0.0632	-0.0602	-0.0673	-0.0795	-0.0827
4.00	-0.0589	-0.0580	-0.0656	-0.0623	-0.0708	-0.0857	-0.0929
5.00	-0.0674	-0.0579	-0.0680	-0.0641	-0.0743	-0.0918	-0.1023
6.00	-0.0746	-0.0638	-0.0704	-0.0657	-0.0777	-0.0978	-0.1115
7.00	-0.0748	-0.0713	-0.0727	-0.0668	-0.0812	-0.1038	-0.1201
8.00	-0.0675	-0.0740	-0.0748	-0.0672	-0.0845	-0.1095	-0.1281
9.00	-0.0565	-0.0691	-0.0765	-0.0659	-0.0879	-0.1147	-0.1347
10.00	-0.0469	-0.0565	-0.0774	-0.0598	-0.0912	-0.1195	-0.1391
11.00	-0.0428	-0.0474	-0.0744	-0.0557	-0.0944	-0.1233	-0.1275
12.00	-0.0392	-0.0413	-0.0685	-0.0532	-0.0971	-0.1267	-0.1229
13.00	-0.0363	-0.0377	-0.0597	-0.0516	-0.0995	-0.1102	-0.1208
14.00	-0.0337	-0.0351	-0.0538	-0.0515	-0.1009	-0.1097	-0.1184
15.00	-0.0320	-0.0345	-0.0518	-0.0526	-0.1003	-0.1034	-0.1065

Airfoil Efficiency / Free Transition / Clean

Alpha	15.2%	17.0%	20.0%	23.0%	26.2%	35.0%	45.0%
Alpha	3.0E+06	3.0E+06	5.6E+06	5.0E+06	5.6E+06	3.0E+06	4.5E+06
-4.00	-20	-19	-17	-13	-9	-7	-7
-3.00	-4	-3	-1	2	5	3	1
-2.00	13	14	17	20	23	13	11
-1.00	31	32	36	41	50	25	24
0.00	51	53	58	66	71	40	39
1.00	75	76	83	85	89	57	53
2.00	101	100	105	103	106	70	64
3.00	128	124	124	119	122	82	75
4.00	147	141	140	133	137	92	87
5.00	160	151	154	148	151	101	97
6.00	169	160	168	160	163	109	107
7.00	160	167	178	171	173	116	113
8.00	144	160	183	177	181	121	117
9.00	106	147	185	185	190	123	115
10.00	85	111	179	189	196	123	109
11.00	74	84	161	185	201	120	78
12.00	62	64	132	177	200	119	59
13.00	52	52	100	161	198	80	47
14.00	42	43	72	136	187	66	37
15.00	33	41	61	97	169	40	19

Table 5.2 STAR Series Lift and Drag Assuming Soiled Airfoils

Lift Coefficient / Fixed Transition / Soiled

Alpha	15.2%	17.0%	20.0%	23.0%	26.2%	35.0%	45.0%
Re	3.0E+06	3.0E+06	5.6E+06	5.0E+06	5.6E+06	3.0E+06	4.5E+06
-4.00	-0.16	-0.15	-0.13	-0.11	-0.09	-0.10	-0.01
-3.00	-0.05	-0.04	-0.01	0.01	0.03	0.03	0.00
-2.00	0.06	0.08	0.11	0.13	0.16	0.16	0.12
-1.00	0.18	0.19	0.22	0.25	0.28	0.29	0.25
0.00	0.29	0.31	0.34	0.37	0.40	0.43	0.37
1.00	0.40	0.42	0.46	0.49	0.53	0.55	0.48
2.00	0.51	0.53	0.58	0.61	0.65	0.68	0.36
3.00	0.62	0.64	0.69	0.73	0.77	0.81	0.07
4.00	0.72	0.75	0.80	0.85	0.89	0.93	0.05
5.00	0.83	0.86	0.92	0.96	1.00	1.04	0.09
6.00	0.93	0.97	1.02	1.07	1.12	1.15	0.13
7.00	1.03	1.07	1.13	1.18	1.22	1.00	0.17
8.00	1.12	1.17	1.23	1.28	1.32	0.72	0.22
9.00	1.20	1.25	1.32	1.36	1.40	0.72	0.27
10.00	1.26	1.32	1.39	1.41	1.15	0.74	0.32
11.00	1.31	1.38	1.44	1.42	1.08	0.77	0.37
12.00	1.35	1.43	1.48	1.38	1.08	0.81	0.42
13.00	1.38	1.46	1.51	1.32	1.09	0.84	0.47
14.00	1.40	1.49	1.52	1.29	1.11	0.88	0.51
15.00	1.40	1.50	1.52	1.29	1.14	0.91	0.56

Drag Coefficient / Fixed Transition / Soiled

Alpha	15.2%	17.0%	20.0%	23.0%	26.2%	35.0%	45.0%
Alpha	3.0E+06	3.0E+06	5.6E+06	5.0E+06	5.6E+06	3.0E+06	4.5E+06
-4.00	0.0095	0.0091	0.0095	0.0107	0.0113	0.0152	0.0266
-3.00	0.0095	0.0090	0.0095	0.0108	0.0111	0.0152	0.0228
-2.00	0.0095	0.0091	0.0095	0.0109	0.0112	0.0152	0.0213
-1.00	0.0096	0.0092	0.0096	0.0110	0.0113	0.0153	0.0210
0.00	0.0097	0.0093	0.0098	0.0112	0.0116	0.0157	0.0216
1.00	0.0099	0.0095	0.0100	0.0115	0.0119	0.0161	0.0229
2.00	0.0102	0.0098	0.0103	0.0119	0.0123	0.0167	0.0354
3.00	0.0105	0.0101	0.0107	0.0124	0.0127	0.0174	0.0655
4.00	0.0109	0.0105	0.0111	0.0129	0.0133	0.0183	0.0776
5.00	0.0114	0.0110	0.0116	0.0137	0.0140	0.0194	0.0857
6.00	0.0120	0.0115	0.0122	0.0147	0.0149	0.0210	0.0945
7.00	0.0127	0.0122	0.0129	0.0162	0.0159	0.0362	0.1028
8.00	0.0136	0.0130	0.0137	0.0183	0.0173	0.0689	0.1111
9.00	0.0148	0.0140	0.0147	0.0215	0.0192	0.0800	0.1190
10.00	0.0165	0.0154	0.0162	0.0264	0.0445	0.0900	0.1279
11.00	0.0196	0.0176	0.0186	0.0336	0.0596	0.0990	0.1367
12.00	0.0235	0.0208	0.0221	0.0433	0.0705	0.1083	0.1454
13.00	0.0285	0.0249	0.0271	0.0540	0.0803	0.1179	0.1543
14.00	0.0348	0.0301	0.0343	0.0641	0.0898	0.1267	0.1636
15.00	0.0426	0.0372	0.0432	0.0741	0.0996	0.1369	0.1739

Moment Coefficient / Fixed Transition / Soiled

Alpha	15.2%	17.0%	20.0%	23.0%	26.2%	35.0%	45.0%
Re	3.0E+06	3.0E+06	5.6E+06	5.0E+06	5.6E+06	3.0E+06	4.5E+06
-4.00	-0.0498	-0.0495	-0.0471	-0.0436	-0.0379	-0.0277	-0.0153
-3.00	-0.0498	-0.0506	-0.0488	-0.0460	-0.0412	-0.0338	-0.0091
-2.00	-0.0499	-0.0517	-0.0505	-0.0483	-0.0442	-0.0400	-0.0200
-1.00	-0.0500	-0.0528	-0.0522	-0.0508	-0.0473	-0.0462	-0.0312
0.00	-0.0501	-0.0539	-0.0540	-0.0532	-0.0505	-0.0522	-0.0395
1.00	-0.0502	-0.0550	-0.0557	-0.0556	-0.0536	-0.0582	-0.0461
2.00	-0.0501	-0.0560	-0.0574	-0.0579	-0.0566	-0.0640	-0.0312
3.00	-0.0501	-0.0569	-0.0590	-0.0602	-0.0596	-0.0696	-0.0139
4.00	-0.0498	-0.0577	-0.0605	-0.0623	-0.0624	-0.0749	-0.0140
5.00	-0.0494	-0.0583	-0.0618	-0.0641	-0.0650	-0.0795	-0.0170
6.00	-0.0487	-0.0587	-0.0629	-0.0657	-0.0673	-0.0830	-0.0201
7.00	-0.0475	-0.0587	-0.0636	-0.0668	-0.0691	-0.0667	-0.0237
8.00	-0.0455	-0.0582	-0.0637	-0.0672	-0.0700	-0.0536	-0.0275
9.00	-0.0417	-0.0555	-0.0628	-0.0659	-0.0684	-0.0541	-0.0316
10.00	-0.0364	-0.0522	-0.0581	-0.0598	-0.0586	-0.0556	-0.0355
11.00	-0.0311	-0.0481	-0.0543	-0.0557	-0.0568	-0.0577	-0.0398
12.00	-0.0267	-0.0438	-0.0508	-0.0532	-0.0578	-0.0601	-0.0441
13.00	-0.0229	-0.0400	-0.0480	-0.0516	-0.0593	-0.0628	-0.0484
14.00	-0.0200	-0.0368	-0.0456	-0.0515	-0.0611	-0.0657	-0.0530
15.00	-0.0179	-0.0339	-0.0443	-0.0526	-0.0632	-0.0687	-0.0576

Airfoil Efficiency / Fixed Transition / Soiled

Alpha	15.2%	17.0%	20.0%	23.0%	26.2%	35.0%	45.0%
Alpha	3.0E+06	3.0E+06	5.6E+06	5.0E+06	5.6E+06	3.0E+06	4.5E+06
-4.00	-17	-17	-14	-10	-8	-7	0
-3.00	-5	-4	-1	1	3	2	0
-2.00	7	9	11	12	14	11	6
-1.00	18	21	23	23	25	19	12
0.00	30	33	35	33	35	27	17
1.00	40	44	46	43	44	34	21
2.00	50	54	56	52	53	41	10
3.00	59	64	65	59	60	46	1
4.00	66	72	73	66	67	51	1
5.00	72	78	79	70	72	54	1
6.00	77	84	84	73	75	55	1
7.00	81	88	88	73	77	28	2
8.00	82	90	90	70	76	10	2
9.00	81	89	90	63	73	9	2
10.00	77	86	85	53	26	8	2
11.00	67	78	78	42	18	8	3
12.00	57	69	67	32	15	7	3
13.00	48	59	56	24	14	7	3
14.00	40	49	44	20	12	7	3
15.00	33	40	35	17	11	7	3

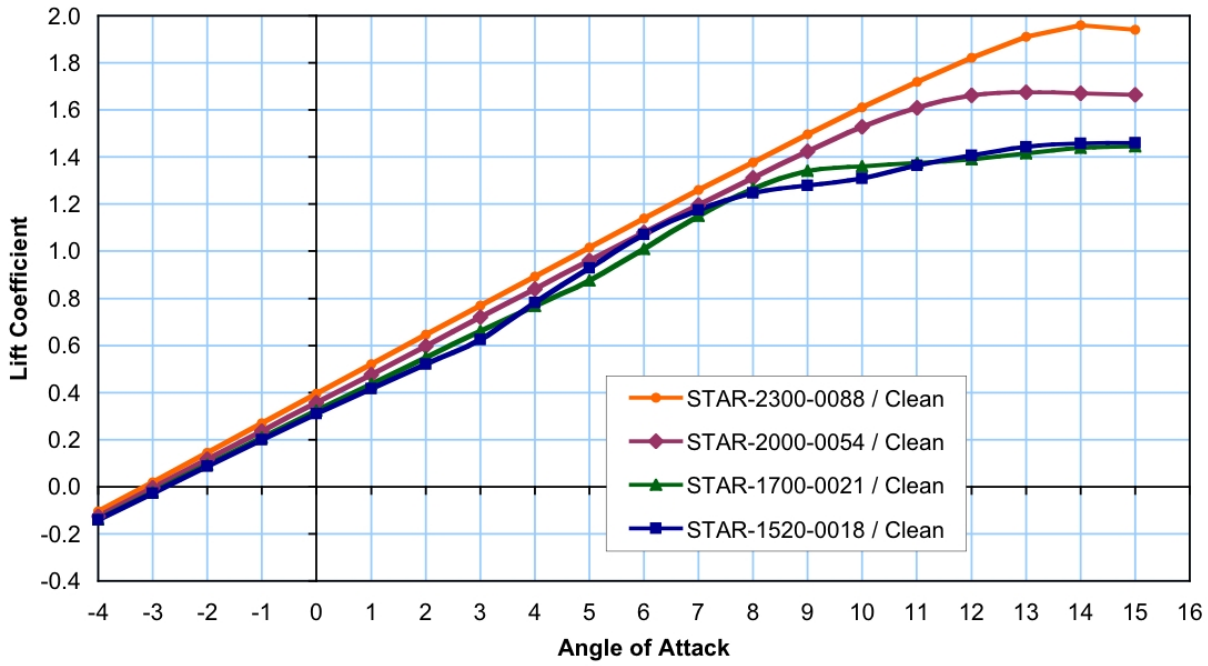

Figure 5.9 STAR Airfoil Lift Characteristics / Clean

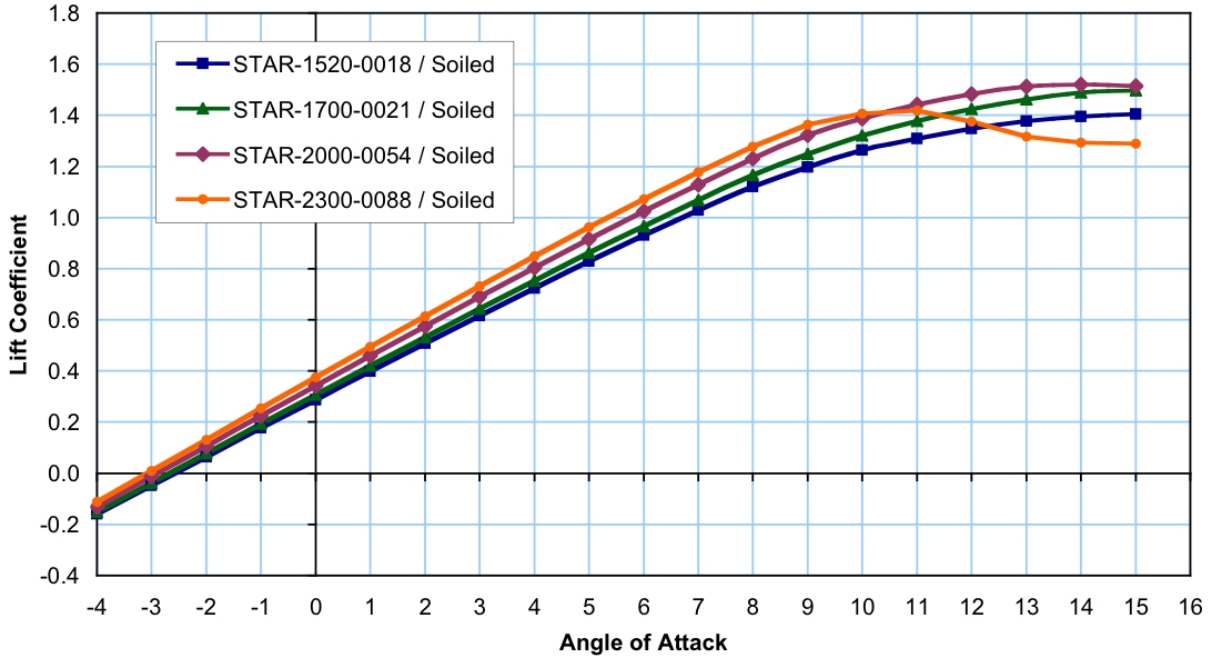

Figure 5.10 STAR Airfoil Lift Characteristics / Soiled

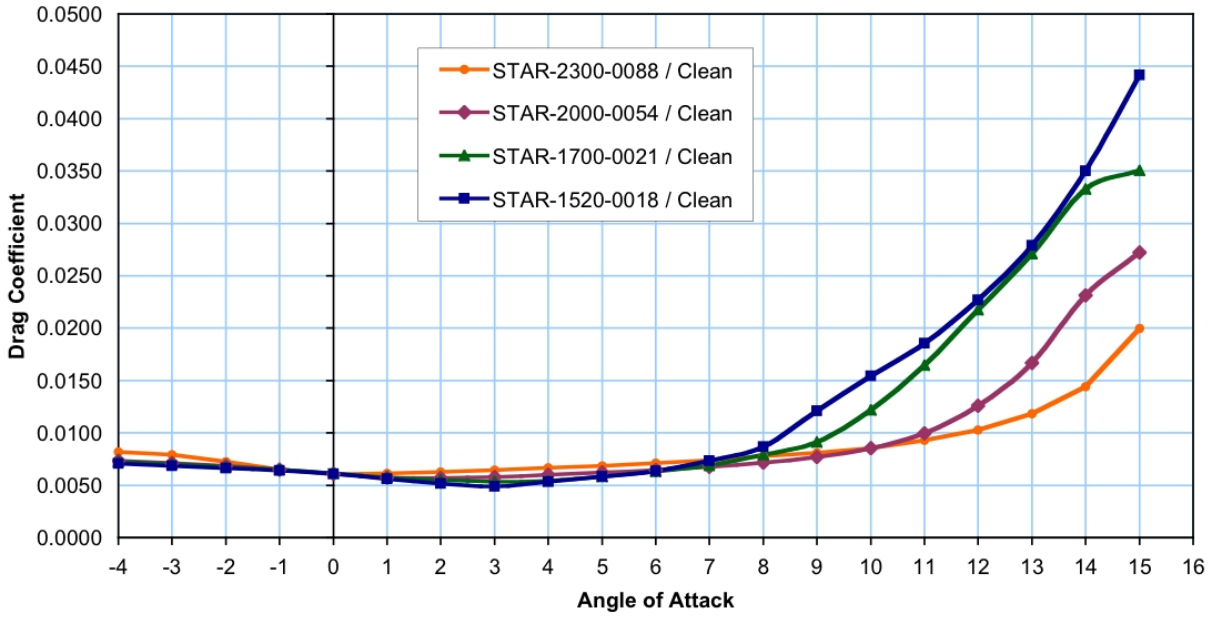

Figure 5.11 STAR Airfoil Drag Characteristics / Clean

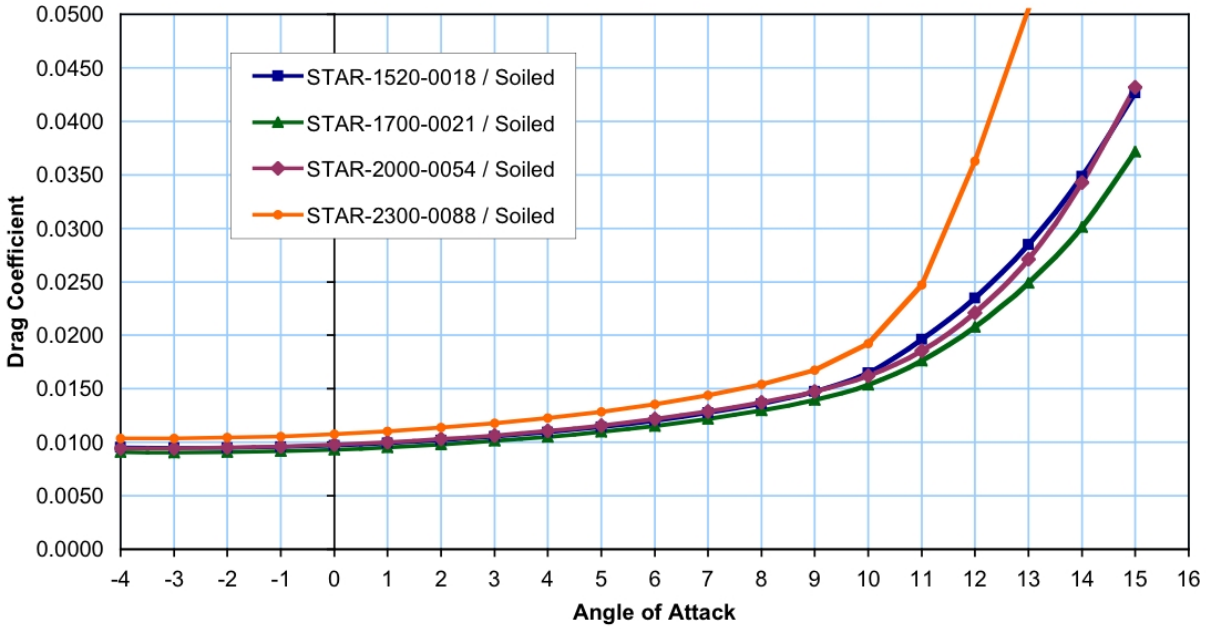

Figure 5.12 STAR Airfoil Drag Characteristics / Soiled

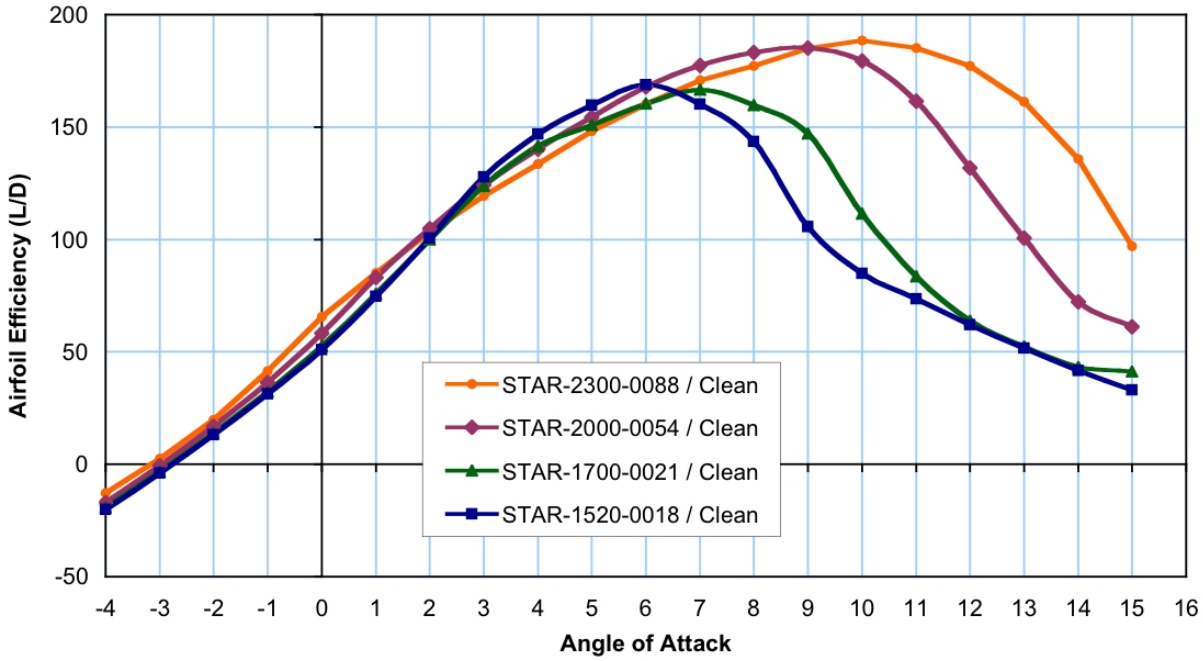

Figure 5.13 STAR Airfoil Lift-to-Drag Characteristics / Clean

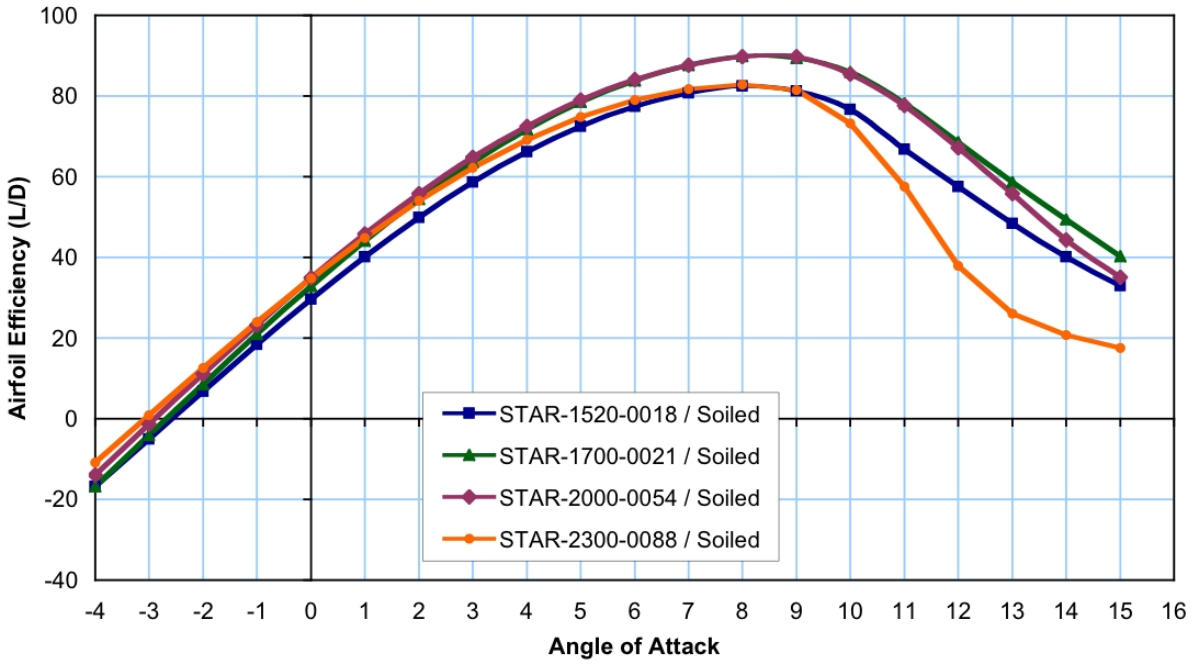

Figure 5.14 STAR Airfoil Lift-to-Drag Characteristics / Soiled

5.1.4 Aerodynamic Input Data

The aerodynamic input data for performance analysis are presented in Table 5.3 for clean airfoil conditions. The airfoil data were linearly interpolated from the STAR family using the local section thickness ratio and Tables 5.1 and 5.2.

Table 5.3 Aerodynamic Input Data Assuming Clean Surfaces

Station 2
Radius Ratio 15%
Thickness Ratio 48.1%
Reynolds Number 2.57E+06

Angle of Attack	Lift Coeff.	Drag Coeff.	Efficiency L/D
-4	-0.0941	0.0145	-6.5
-3	0.0242	0.0171	1.4
-2	0.1685	0.0147	11.4
-1	0.3137	0.0131	24.0
0	0.4606	0.0119	38.7
1	0.6048	0.0115	52.6
2	0.7448	0.0117	63.8
3	0.8847	0.0118	74.8
4	1.0289	0.0118	87.0
5	1.1675	0.0120	97.4
6	1.3044	0.0122	106.6
7	1.4379	0.0127	113.3
8	1.5662	0.0133	117.5
9	1.6822	0.0146	115.1
10	1.7824	0.0164	109.0
11	1.7478	0.0225	77.7
12	1.7354	0.0294	59.0
13	1.7323	0.0367	47.3
14	1.7037	0.0466	36.6
15	1.4507	0.0775	18.7

Station 3
Radius Ratio 25%
Thickness Ratio 33.9%
Reynolds Number 4.02E+06

Angle of Attack	Lift Coeff.	Drag Coeff.	Efficiency L/D
-4	-0.0928	0.0138	-6.7
-3	0.0426	0.0132	3.2
-2	0.1793	0.0127	14.1
-1	0.3177	0.0121	26.4
0	0.4596	0.0110	41.8
1	0.6010	0.0102	59.0
2	0.7379	0.0101	73.2
3	0.8730	0.0103	85.1
4	1.0071	0.0105	95.8
5	1.1400	0.0108	105.1
6	1.2716	0.0112	113.2
7	1.4024	0.0116	120.9
8	1.5301	0.0121	126.0
9	1.6533	0.0129	127.8
10	1.7731	0.0138	128.4
11	1.8856	0.0150	126.1
12	1.9953	0.0160	124.8
13	1.8949	0.0219	86.7
14	1.9384	0.0268	72.2
15	1.8745	0.0414	45.3

Station 4
Radius Ratio 35%
Thickness Ratio 28.0%
Reynolds Number 4.80E+06

Angle of Attack	Lift Coeff.	Drag Coeff.	Efficiency L/D
-4	-0.0854	0.0103	-8.3
-3	0.0440	0.0096	4.6
-2	0.1758	0.0087	20.1
-1	0.3103	0.0076	40.9
0	0.4423	0.0074	60.2
1	0.5733	0.0073	78.8
2	0.7029	0.0074	95.0
3	0.8316	0.0076	109.7
4	0.9599	0.0078	123.3
5	1.0873	0.0080	135.8
6	1.2136	0.0083	146.5
7	1.3388	0.0086	155.9
8	1.4619	0.0090	162.9
9	1.5838	0.0094	168.9
10	1.7036	0.0098	173.2
11	1.8200	0.0104	174.8
12	1.9327	0.0111	174.1
13	1.9915	0.0131	152.6
14	2.0780	0.0151	137.5
15	2.1265	0.0199	106.7

Station 5
Radius Ratio 45%
Thickness Ratio 24.0%
Reynolds Number 5.28E+06

Angle of Attack	Lift Coeff.	Drag Coeff.	Efficiency L/D
-4	-0.0975	0.0085	-11.4
-3	0.0278	0.0081	3.4
-2	0.1539	0.0073	21.0
-1	0.2820	0.0064	44.1
0	0.4090	0.0061	67.2
1	0.5350	0.0062	86.4
2	0.6608	0.0063	104.1
3	0.7858	0.0065	120.1
4	0.9101	0.0068	134.6
5	1.0342	0.0069	149.0
6	1.1570	0.0072	161.0
7	1.2787	0.0075	171.5
8	1.3981	0.0078	178.5
9	1.5172	0.0081	186.4
10	1.6338	0.0085	191.1
11	1.7458	0.0092	190.1
12	1.8520	0.0100	184.5
13	1.9470	0.0113	172.0
14	2.0126	0.0134	150.0
15	2.0279	0.0177	114.5

Station 6
Radius Ratio 55%
Thickness Ratio 22.8%
Reynolds Number 5.46E+06

Angle of Attack	Lift Coeff.	Drag Coeff.	Efficiency L/D
-4	-0.1061	0.0081	-13.0
-3	0.0177	0.0078	2.3
-2	0.1416	0.0072	19.6
-1	0.2667	0.0065	41.0
0	0.3925	0.0060	65.0
1	0.5172	0.0061	84.9
2	0.6420	0.0062	103.4
3	0.7660	0.0064	119.7
4	0.8890	0.0066	134.0
5	1.0120	0.0068	148.6
6	1.1337	0.0071	160.6
7	1.2544	0.0073	171.3
8	1.3724	0.0077	177.7
9	1.4899	0.0081	184.9
10	1.6042	0.0085	187.9
11	1.7111	0.0093	183.2
12	1.8099	0.0105	173.1
13	1.8920	0.0122	154.8
14	1.9367	0.0151	128.4
15	1.9191	0.0205	93.4

Station 7
Radius Ratio 65%
Thickness Ratio 22.3%
Reynolds Number 5.25E+06

Angle of Attack	Lift Coeff.	Drag Coeff.	Efficiency L/D
-4	-0.1096	0.0080	-13.7
-3	0.0137	0.0077	1.8
-2	0.1369	0.0072	19.1
-1	0.2611	0.0065	40.2
0	0.3858	0.0060	63.8
1	0.5097	0.0060	84.6
2	0.6339	0.0061	103.6
3	0.7574	0.0063	120.5
4	0.8799	0.0065	135.0
5	1.0024	0.0067	149.6
6	1.1237	0.0069	161.9
7	1.2437	0.0072	172.4
8	1.3612	0.0076	178.6
9	1.4776	0.0080	184.9
10	1.5902	0.0085	186.3
11	1.6921	0.0095	179.0
12	1.7826	0.0109	164.3
13	1.8519	0.0130	142.0
14	1.8877	0.0166	114.0
15	1.8721	0.0218	86.0

Table 5.3 Aerodynamic Input Data Assuming Clean Surfaces (continued)

Station	**8**
Radius Ratio	75%
Thickness Ratio	21.5%
Reynolds Number	4.84E+06

Angle of Attack	Lift Coeff.	Drag Coeff.	Efficiency L/D
-4	-0.1149	0.0078	-14.8
-3	0.0074	0.0075	1.0
-2	0.1297	0.0071	18.3
-1	0.2525	0.0065	38.9
0	0.3757	0.0061	61.9
1	0.4983	0.0059	84.1
2	0.6215	0.0060	104.0
3	0.7444	0.0061	121.7
4	0.8661	0.0063	136.7
5	0.9877	0.0065	151.1
6	1.1083	0.0068	163.8
7	1.2275	0.0071	174.1
8	1.3441	0.0075	180.1
9	1.4590	0.0079	185.0
10	1.5690	0.0085	183.9
11	1.6631	0.0096	172.7
12	1.7410	0.0115	152.0
13	1.7908	0.0143	125.4
14	1.8131	0.0188	96.4
15	1.8005	0.0237	76.1

Station	**9**
Radius Ratio	85%
Thickness Ratio	19.6%
Reynolds Number	4.34E+06

Angle of Attack	Lift Coeff.	Drag Coeff.	Efficiency L/D
-4	-0.1271	0.0073	-17.3
-3	-0.0071	0.0071	-1.0
-2	0.1128	0.0069	16.5
-1	0.2321	0.0065	35.8
0	0.3517	0.0061	57.5
1	0.4709	0.0057	82.0
2	0.5910	0.0057	104.0
3	0.7111	0.0057	124.2
4	0.8297	0.0059	140.4
5	0.9479	0.0062	153.8
6	1.0694	0.0064	166.8
7	1.1899	0.0068	176.0
8	1.3048	0.0073	179.6
9	1.4119	0.0079	178.9
10	1.5049	0.0090	166.5
11	1.5753	0.0109	144.9
12	1.6235	0.0139	116.9
13	1.6381	0.0181	90.4
14	1.6382	0.0245	66.8
15	1.6334	0.0283	57.7

Station	**10**
Radius Ratio	95%
Thickness Ratio	16.5%
Reynolds Number	3.07E+06

Angle of Attack	Lift Coeff.	Drag Coeff.	Efficiency L/D
-4	-0.1399	0.0072	-19.5
-3	-0.0242	0.0070	-3.5
-2	0.0913	0.0067	13.6
-1	0.2060	0.0065	31.9
0	0.3190	0.0061	52.1
1	0.4303	0.0057	75.4
2	0.5400	0.0054	100.1
3	0.6492	0.0052	125.0
4	0.7720	0.0054	143.0
5	0.8926	0.0058	153.5
6	1.0286	0.0063	163.0
7	1.1575	0.0070	164.5
8	1.2587	0.0081	154.5
9	1.3228	0.0100	131.9
10	1.3455	0.0132	102.0
11	1.3719	0.0171	80.3
12	1.3954	0.0220	63.3
13	1.4243	0.0273	52.1
14	1.4442	0.0338	42.7
15	1.4502	0.0378	38.3

A linear model that accounts for observed soiling patterns was used to estimate soiled rotor performance. The model assumed 95% soiled airfoil properties (5% clean) at 95% radius trending linearly to 15% soiled airfoil properties (85% clean) at 15% radius (Table 5.4).

Table 5.4 Aerodynamic Input Data Assuming a Linear Soiling Model

Station	**2**
Radius Ratio	15%
Thickness Ratio	48.1%
Reynolds Number	2.57E+06

Angle of Attack	Lift Coeff.	Drag Coeff.	Efficiency L/D
-4	-0.0819	0.0163	-5.0
-3	0.0204	0.0180	1.1
-2	0.1611	0.0157	10.2
-1	0.3043	0.0143	21.3
0	0.4476	0.0133	33.6
1	0.5867	0.0132	44.5
2	0.6867	0.0152	45.1
3	0.7624	0.0199	38.4
4	0.8828	0.0217	40.7
5	1.0063	0.0230	43.7
6	1.1280	0.0246	45.9
7	1.2482	0.0262	47.6
8	1.3643	0.0280	48.7
9	1.4706	0.0303	48.6
10	1.5626	0.0331	47.2
11	1.5405	0.0396	38.9
12	1.5375	0.0468	32.8
13	1.5422	0.0543	28.4
14	1.5252	0.0641	23.8
15	1.3167	0.0920	14.3

Station	**3**
Radius Ratio	25%
Thickness Ratio	33.9%
Reynolds Number	4.02E+06

Angle of Attack	Lift Coeff.	Drag Coeff.	Efficiency L/D
-4	-0.0948	0.0140	-6.7
-3	0.0396	0.0136	2.9
-2	0.1749	0.0132	13.2
-1	0.3115	0.0128	24.4
0	0.4504	0.0120	37.4
1	0.5885	0.0115	51.0
2	0.7230	0.0116	62.4
3	0.8554	0.0119	71.9
4	0.9862	0.0123	80.2
5	1.1147	0.0128	86.9
6	1.2398	0.0135	91.9
7	1.3095	0.0171	76.4
8	1.3456	0.0248	54.3
9	1.4406	0.0279	51.7
10	1.5274	0.0315	48.5
11	1.6167	0.0348	46.5
12	1.7060	0.0379	45.0
13	1.6387	0.0447	36.6
14	1.6809	0.0507	33.2
15	1.6410	0.0641	25.6

Station	**4**
Radius Ratio	35%
Thickness Ratio	28.0%
Reynolds Number	4.80E+06

Angle of Attack	Lift Coeff.	Drag Coeff.	Efficiency L/D
-4	-0.0893	0.0109	-8.2
-3	0.0391	0.0104	3.8
-2	0.1691	0.0099	17.1
-1	0.3007	0.0092	32.7
0	0.4304	0.0091	47.1
1	0.5591	0.0092	60.8
2	0.6865	0.0094	72.8
3	0.8127	0.0097	83.5
4	0.9378	0.0101	92.9
5	1.0611	0.0105	100.9
6	1.1819	0.0111	107.0
7	1.2820	0.0127	101.2
8	1.3678	0.0157	87.0
9	1.4681	0.0173	84.6
10	1.4801	0.0254	58.4
11	1.5379	0.0306	50.3
12	1.6127	0.0347	46.5
13	1.6579	0.0394	42.1
14	1.7230	0.0440	39.1
15	1.7632	0.0506	34.9

Table 5.4 Aerodynamic Input Data Assuming a Linear Soiling Model (continued)

Station	**5**
Radius Ratio	45%
Thickness Ratio	24.0%
Reynolds Number	5.28E+06

Angle of Attack	Lift Coeff.	Drag Coeff.	Efficiency L/D
-4	-0.1017	0.0096	-10.6
-3	0.0226	0.0093	2.4
-2	0.1472	0.0090	16.4
-1	0.2729	0.0085	32.0
0	0.3978	0.0084	47.1
1	0.5216	0.0086	60.3
2	0.6449	0.0089	72.5
3	0.7671	0.0092	83.2
4	0.8881	0.0096	92.5
5	1.0078	0.0100	100.5
6	1.1253	0.0106	106.2
7	1.2401	0.0113	109.4
8	1.3503	0.0124	108.9
9	1.4531	0.0138	105.1
10	1.4939	0.0193	77.6
11	1.5485	0.0240	64.5
12	1.5934	0.0290	54.9
13	1.6299	0.0344	47.4
14	1.6620	0.0400	41.5
15	1.6729	0.0468	35.7

Station	**6**
Radius Ratio	55%
Thickness Ratio	21.1%
Reynolds Number	5.46E+06

Angle of Attack	Lift Coeff.	Drag Coeff.	Efficiency L/D
-4	-0.1106	0.0095	-11.6
-3	0.0122	0.0094	1.3
-2	0.1348	0.0092	14.7
-1	0.2580	0.0089	28.9
0	0.3811	0.0088	43.2
1	0.5032	0.0090	55.8
2	0.6249	0.0093	67.4
3	0.7454	0.0096	77.6
4	0.8645	0.0100	86.2
5	0.9823	0.0105	93.5
6	1.0978	0.0112	98.4
7	1.2104	0.0120	100.5
8	1.3183	0.0134	98.7
9	1.4189	0.0152	93.5
10	1.4946	0.0179	83.3
11	1.5514	0.0220	70.4
12	1.5758	0.0276	57.0
13	1.5835	0.0340	46.5
14	1.5918	0.0408	39.0
15	1.5824	0.0487	32.5

Station	**7**
Radius Ratio	65%
Thickness Ratio	20.1%
Reynolds Number	5.25E+06

Angle of Attack	Lift Coeff.	Drag Coeff.	Efficiency L/D
-4	-0.1148	0.0096	-12.0
-3	0.0073	0.0095	0.8
-2	0.1290	0.0094	13.8
-1	0.2511	0.0092	27.3
0	0.3730	0.0092	40.6
1	0.4941	0.0094	52.8
2	0.6147	0.0096	63.9
3	0.7341	0.0100	73.7
4	0.8520	0.0104	82.0
5	0.9684	0.0109	88.8
6	1.0824	0.0116	93.4
7	1.1933	0.0125	95.4
8	1.2993	0.0138	93.9
9	1.3971	0.0157	89.0
10	1.4676	0.0185	79.3
11	1.5183	0.0227	66.8
12	1.5356	0.0285	53.8
13	1.5349	0.0353	43.5
14	1.5371	0.0427	36.0
15	1.5297	0.0508	30.1

Station	**8**
Radius Ratio	75%
Thickness Ratio	20.0%
Reynolds Number	4.84E+06

Angle of Attack	Lift Coeff.	Drag Coeff.	Efficiency L/D
-4	-0.1207	0.0095	-12.7
-3	0.0029	0.0095	0.3
-2	0.1185	0.0094	12.6
-1	0.2341	0.0094	25.0
0	0.3494	0.0094	37.2
1	0.4639	0.0095	48.6
2	0.5776	0.0098	58.9
3	0.6899	0.0102	67.9
4	0.7994	0.0106	75.5
5	0.9034	0.0111	81.4
6	1.0051	0.0118	85.4
7	1.1025	0.0126	87.2
8	1.1933	0.0139	86.1
9	1.2752	0.0155	82.1
10	1.3385	0.0181	74.1
11	1.3860	0.0219	63.3
12	1.4166	0.0273	51.9
13	1.4351	0.0338	42.4
14	1.4445	0.0414	34.9
15	1.4436	0.0497	29.0

Station	**9**
Radius Ratio	85%
Thickness Ratio	18.9%
Reynolds Number	4.34E+06

Angle of Attack	Lift Coeff.	Drag Coeff.	Efficiency L/D
-4	-0.1339	0.0091	-14.7
-3	-0.0153	0.0090	-1.7
-2	0.1029	0.0091	11.4
-1	0.2210	0.0091	24.3
0	0.3387	0.0092	36.9
1	0.4558	0.0093	48.9
2	0.5723	0.0095	60.0
3	0.6877	0.0098	69.8
4	0.8016	0.0102	78.3
5	0.9136	0.0107	85.4
6	1.0240	0.0112	91.1
7	1.1313	0.0119	95.2
8	1.2337	0.0127	97.5
9	1.3268	0.0136	97.5
10	1.3965	0.0150	92.8
11	1.4543	0.0173	84.1
12	1.4978	0.0207	72.4
13	1.5246	0.0255	59.8
14	1.5335	0.0323	47.5
15	1.5307	0.0403	38.0

Station	**10**
Radius Ratio	95%
Thickness Ratio	15.2%
Reynolds Number	3.07E+06

Angle of Attack	Lift Coeff.	Drag Coeff.	Efficiency L/D
-4	-0.1538	0.0091	-16.9
-3	-0.0394	0.0091	-4.4
-2	0.0747	0.0091	8.2
-1	0.1884	0.0092	20.6
0	0.3017	0.0093	32.5
1	0.4143	0.0095	43.8
2	0.5259	0.0097	54.3
3	0.6364	0.0100	63.7
4	0.7460	0.0104	71.9
5	0.8536	0.0109	78.7
6	0.9596	0.0114	84.1
7	1.0618	0.0121	87.8
8	1.1575	0.0129	89.7
9	1.2373	0.0140	88.4
10	1.3051	0.0156	83.8
11	1.3572	0.0182	74.7
12	1.4014	0.0216	64.8
13	1.4352	0.0261	55.1
14	1.4594	0.0317	46.1
15	1.4681	0.0388	37.9

5.1.5 Rotor Efficiency, Power, and Energy Output

A blade element momentum theory model was used to estimate rotor performance. The effects of sweep were included using a cosine squared correction. The rotor efficiency at run pitch (0°) is shown in Figure 5.15 and the power curve is plotted in Figure 5.16. A power

curve for the 50 m baseline rotor using STAR airfoils and the baseline planform are both provided.

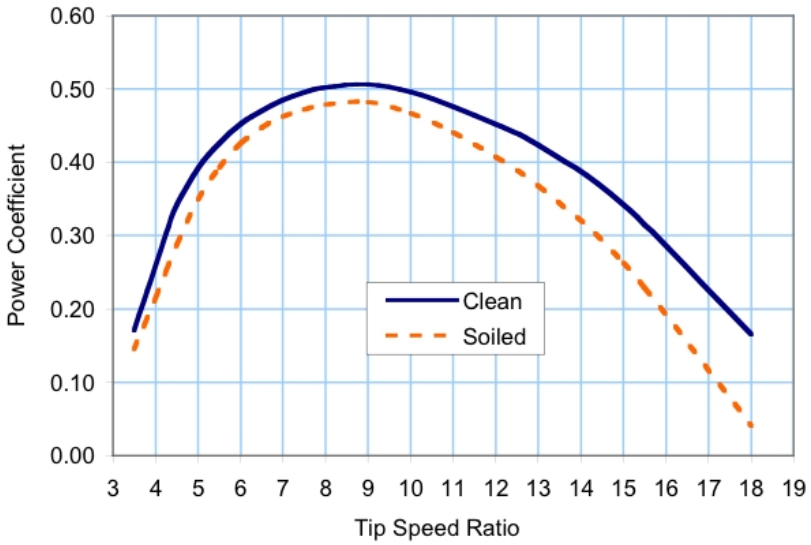

Tip Speed Ratio	Power Coefficient	
	Clean	Soiled
3.50	0.171	0.145
3.75	0.214	0.179
4.00	0.259	0.216
4.25	0.304	0.253
4.50	0.342	0.288
5.00	0.392	0.349
5.50	0.426	0.393
6.00	0.453	0.426
6.50	0.471	0.448
7.00	0.485	0.462
7.50	0.495	0.472
8.00	0.502	0.479
9.00	0.506	0.482
10.00	0.496	0.467
11.00	0.476	0.441
12.00	0.452	0.407
13.00	0.424	0.368
15.00	0.342	0.263
18.00	0.165	0.041

Figure 5.15 Rotor Efficiency Curve at 0° Pitch Angle

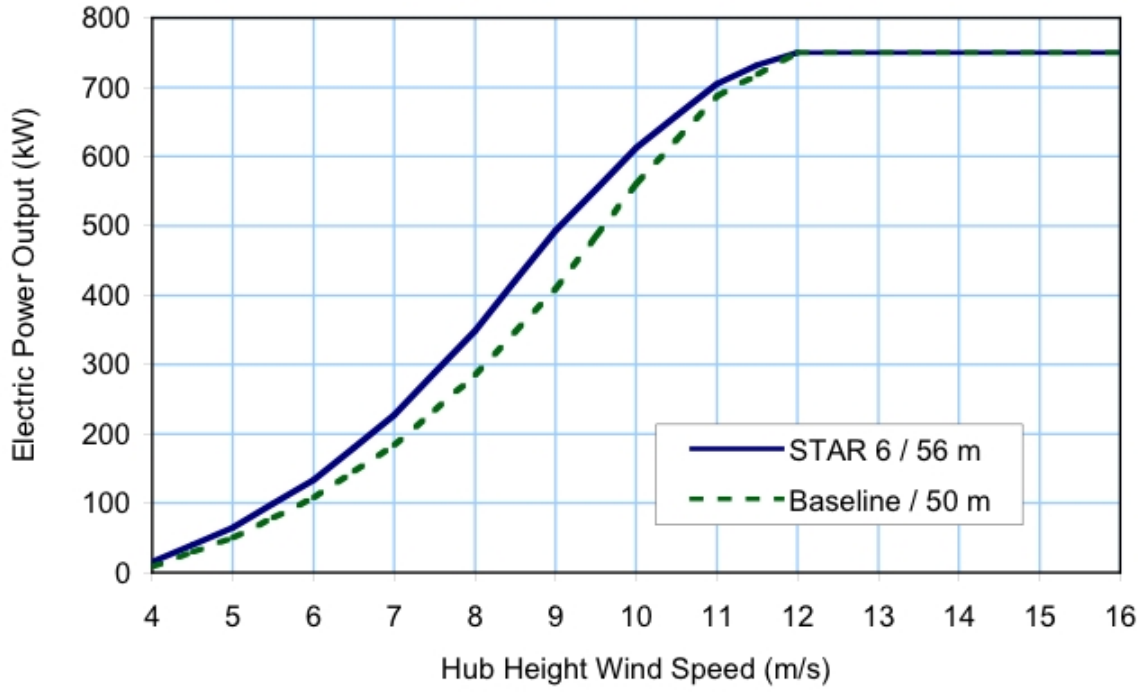

Figure 5.16 Rotor Power Curve Comparison (clean)

Preliminary design estimates indicated that the STAR 6 planform would provide 8.3% greater energy capture in IEC Class III sites (Table 5.5). Passive blade twist in the outer blade will

be used to limit the maximum rotor thrust as shown in Figure 5.17. A comparison of clean and soiled performance is shown in Table 5.6 and Figure 5.18.

Table 5.5 Rotor Performance Comparison

Hub Speed (m/s)	STAR 6 / 56 m (kW)	Baseline / 50 m (kW)
4.0	15.2	8.7
4.5	40.0	29.4
5.0	64.8	50.2
5.5	99.2	79.2
6.0	133.6	108.2
6.5	180.4	146.0
7.0	227.3	183.8
7.5	288.1	234.1
8.0	348.9	284.5
8.5	420.9	346.8
9.0	493.0	409.1
9.5	552.9	485.2
10.0	612.8	561.3
10.5	658.9	624.1
11.0	705.0	687.0
11.5	731.7	718.6
12.0	750.0	750.0
20.0	750.0	750.0

Hub Wind Speed (m/s)	STAR 6 / 56 m (kW)	Baseline / 50 m (kW)	Power Difference (kW)	Power Difference (%)
4.0	15.2	8.7	6.5	43%
5.0	64.8	50.2	14.6	23%
6.0	133.6	108.2	25.4	19%
7.0	227.3	183.8	43.6	19%
8.0	348.9	284.5	64.4	18%
9.0	493.0	409.1	83.9	17%
10.0	612.8	561.3	51.5	8%
11.0	705.0	687.0	18.0	3%
12.0	750.0	750.0	0.0	0%
20.0	750.0	750.0	0.0	0%

	Annual Energy Output (MWh)			
IEC Class	I	II	III	IV
(m/s)	10.0	8.5	7.5	6.0
STAR 6	3908	3294	2767	1832
Baseline	3711	3075	2538	1618
Difference	5.0%	6.7%	8.3%	11.7%

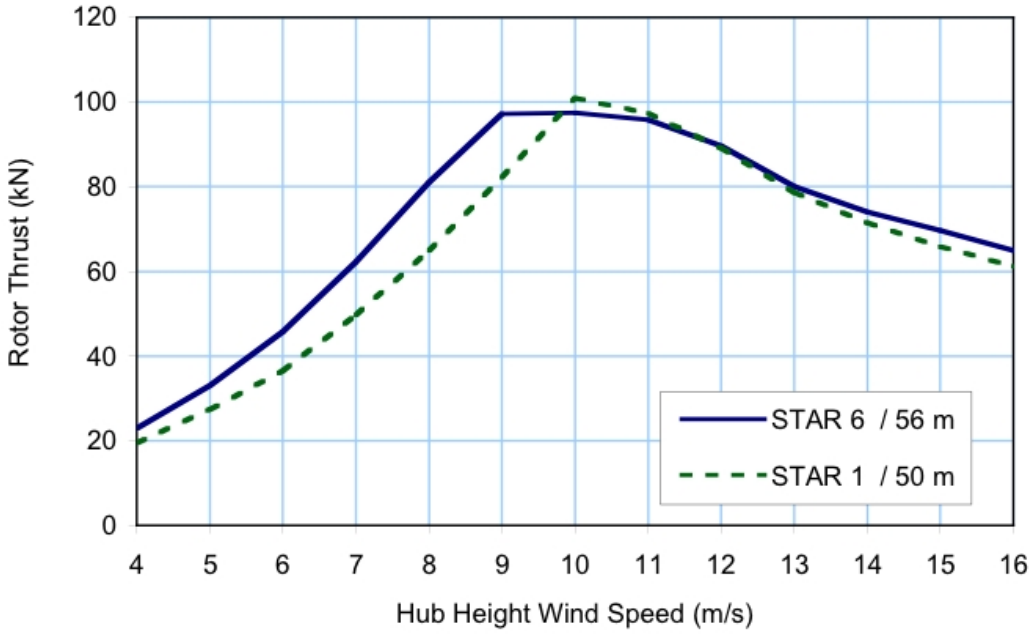

Figure 5.17 Rotor Thrust Comparison

Table 5.6 Soiled Rotor Performance Comparison

Hub Speed (m/s)	STAR 6 / 56 m (kW)	STAR 6 Soiled (kW)
4.0	15.2	8.4
4.5	40.0	32.8
5.0	64.8	57.1
5.5	99.2	90.9
6.0	133.6	124.7
6.5	180.4	170.0
7.0	227.3	215.4
7.5	288.1	273.6
8.0	348.9	331.9
8.5	420.9	401.5
9.0	493.0	471.0
9.5	552.9	530.0
10.0	612.8	589.1
10.5	658.9	640.3
11.0	705.0	691.5
11.5	731.7	727.7
12.0	750.0	750.0
20.0	750.0	750.0

Hub Wind Speed (m/s)	STAR 6 / 56 m (kW)	STAR 6 Soiled (kW)	Power Difference (kW)	Power Difference (%)
4.0	15.2	8.4	6.7	45%
5.0	64.8	57.1	7.7	12%
6.0	133.6	124.7	8.9	7%
7.0	227.3	215.4	12.0	5%
8.0	348.9	331.9	16.9	5%
9.0	493.0	471.0	22.0	4%
10.0	612.8	589.1	23.7	4%
11.0	705.0	691.5	13.5	2%
12.0	750.0	750.0	0.0	0%
20.0	750.0	750.0	0.0	0%

	Annual Energy Output (MWh)			
IEC Class	I	II	III	IV
(m/s)	10.0	8.5	7.5	6.0
Clean	3908	3294	2767	1832
Soiled	3840	3219	2689	1758
Difference	1.7%	2.3%	2.8%	4.0%

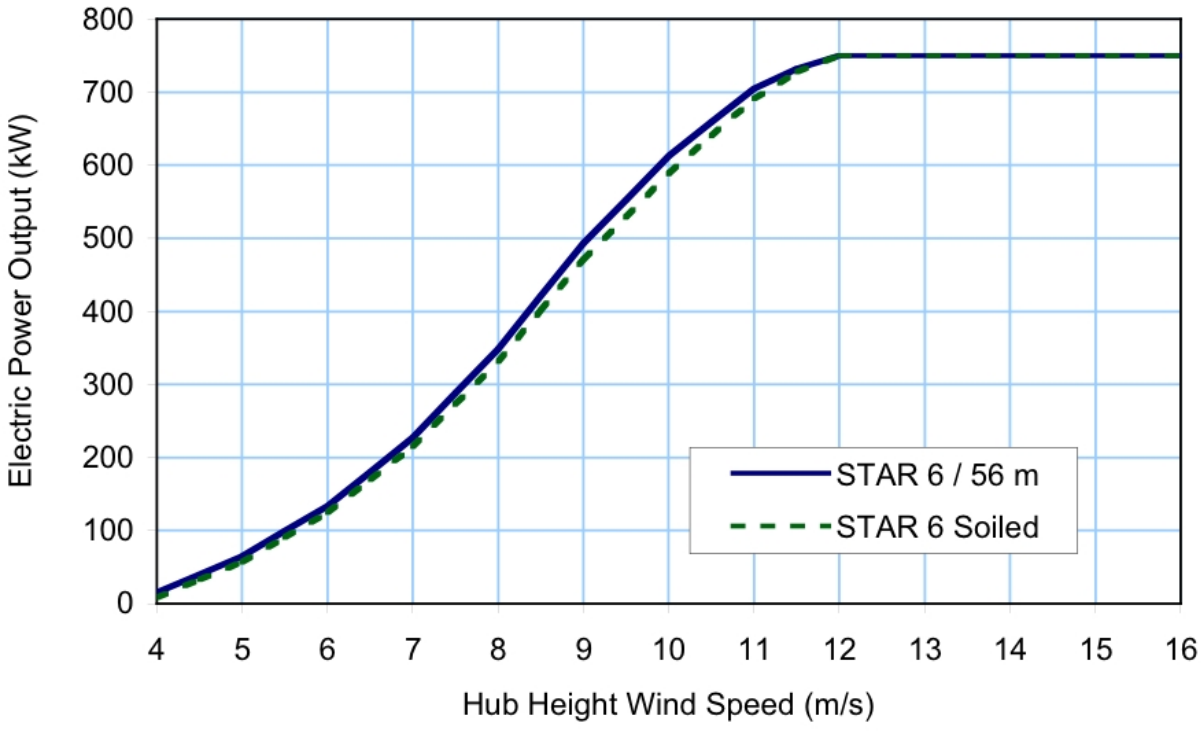

Figure 5.18 Soiled Rotor Performance Comparison

5.1.6 Acoustic Noise

As a result of the increase in blade length without modification in rotor rpm, the STAR blades will operate at tip speeds that are somewhat higher than the baseline blades. During the conceptual design stage we reviewed the literature to evaluate the impact of higher tip speed on acoustic noise. Blade aerodynamic noise will increase as a result of the higher blade operating speeds. A number of observations were developed with regard to noise impacts. These observations were based in part on several reference sources [6,7,8,9,10].

The rotor tips generate a broadband type of noise as a result of instabilities of (1) in the turbulent shear layers at the tip and (2) interaction of the tip vortex with the trailing edge of the blade. In part as a result of the complicated flow development in the tip region, the tip noise mechanisms are still not well understood. This lack of understanding explains that up to this point most of the tip noise reduction techniques have been developed through trial and error. Lack of understanding also raises the level of risk.

There is a strong similarity with flap edge noise generated by airplane flaps. A significant amount of research has been conducted in this area in the recent past, e.g. [9]. Based on the fact that the interaction of the tip vortex with the trailing edge appears to play an important role in the tip noise generation process, a very sharp trailing edge (trailing edge thickness less than 0.3-0.5 times the boundary-layer displacement thickness) is required in the tip region. (Note, the boundary layer thickness to chord ratio becomes smaller with increasing Reynolds number and, hence, the sharpness requirement increases with increasing rotor size).

Most of the trailing edge noise of a blade is generated in the tip region (outer 10-20%) as a result of the higher flow velocities and the tip effect. The aerodynamic loading characteristics in the tip region which are in large part governed by the geometry of the blade tip, play a critical role in determining the tip noise levels:

$$L' = c_l \frac{1}{2} \rho V^2 c = \rho V \Gamma$$

$$\Gamma = \frac{c_l V c}{2}$$

$$d\Gamma_{trailing} = -\frac{d\Gamma}{dy} dy$$

where L' is the lift per unit span, V is the local flow velocity, c_l is the sectional lift coefficient, c is the local chord, and Γ is the bound circulation. The above equations show that the trailing vortex strength in the tip region is a function of the spanwise gradient of the bound circulation in the tip region, $\Gamma(y)$, where $\Gamma = 0$ at the tip. Reducing the vortex shedding at the immediate tip appears to contribute significantly to a drop in tip noise (Figures 5.19 and 5.20).

$\Gamma(y)$ is a function of:

1. Section angle of attack, $\alpha(y)$. In the linear lift regime $c_l = 2\pi\alpha$ with α measured w.r.t. zero-lift line. Washout (fixed and aeroelastic) in the tip region reduces Γ at the tip.

2. Velocity, $V(y)$.

3. Chord, $c(y)$. Taper in tip region to spreads vortex shedding and reduces Γ at the tip.

4. Sweep angle. Backward sweep increases the tip loading and, hence, increases the drop in Γ at tip. Forward sweep increases the loading inboard and, hence, decreases the drop in Γ at the tip.

Note some of these observations are based on 3-D wing aerodynamics experiences and must be validated using rotor flow simulations using methods that capture the governing phenomena. However, they appear to explain why 1) backward sweep in the tip region almost always results in higher noise levels, 2) the ogee type tip (Figures 5.19, 5.21, and 5.22) with its forward sweep has relatively low noise levels, and 3) the lowest noise tips, ogee type tip (Figures 5.19, 5.21, and 5.22) and sword shape type tip, (Figure 5.20) includes a relatively long tapered section that terminates at the tip with a near-zero chord length.

Broadband tip vortex noise intensity scales by the effective velocity to the power 5 or 6. With tip speed defined as:

$$V_{tip} = \sqrt{(\pi nD)^2 + V_\infty{}^2}$$

where n is the number of revolutions per second, D is the rotor diameter, and V_∞ is the wind velocity. Based on this the sound pressure level SPL $\approx 50 \log_{10} V_{tip}$, which indicates that an increase in tip speed from 70 m/s to 100 m/s results in 7.7 dB increase in noise and an increase in tip speed from 80 m/s to 100 m/s in 4.8 dB higher noise levels.

Experiments that have been conducted show reductions in noise level not greater than 5 dB compared to the typical reference tip. This appears to indicate that a goal of 5 dB reduction in tip noise compared to the tips used on current blades (e.g., Z50 blade) is challenging and that larger reductions in noise may be unrealistic at this point in time. Assuming that we can achieve this 5 dB noise reduction goal, it would limit the increase in tip speed to 26%.

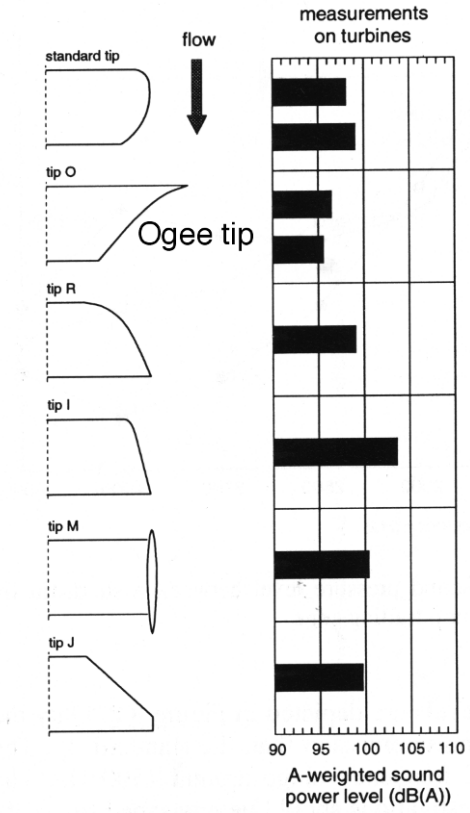

Figure 5.19 Ogee tip (Source: Wagner et al, 1996)

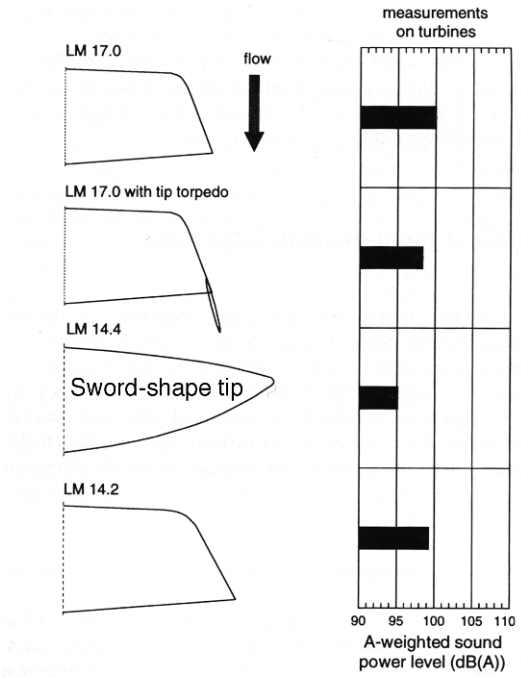

Figure 5.20. Sword shape tip (Wagner et al, 1996)

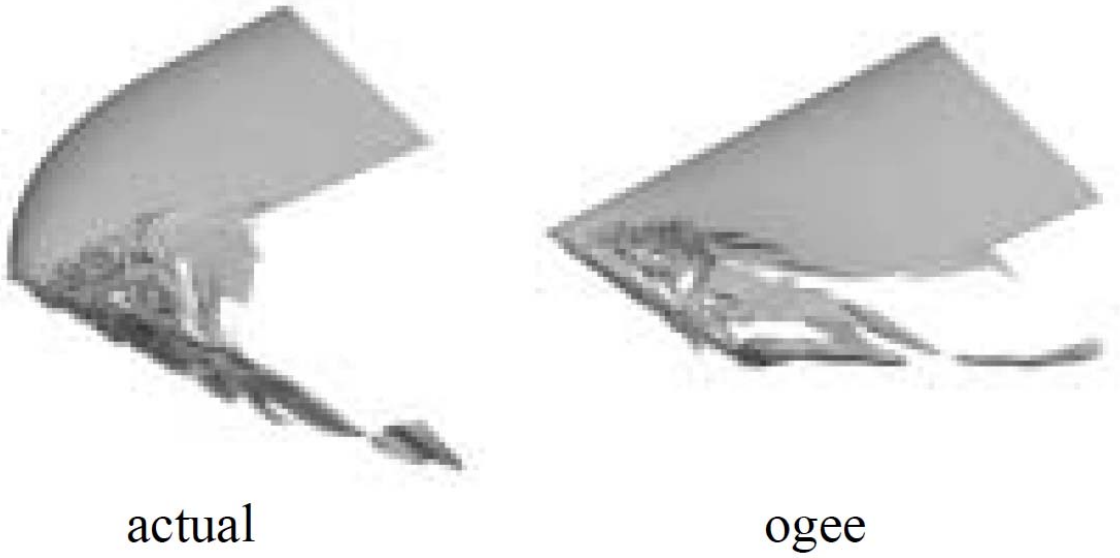

Figure 5.21. Trailing vorticity isosurfaces for actual (baseline) sweptback tip and ogee tip (Source: Iida et al, 2005)

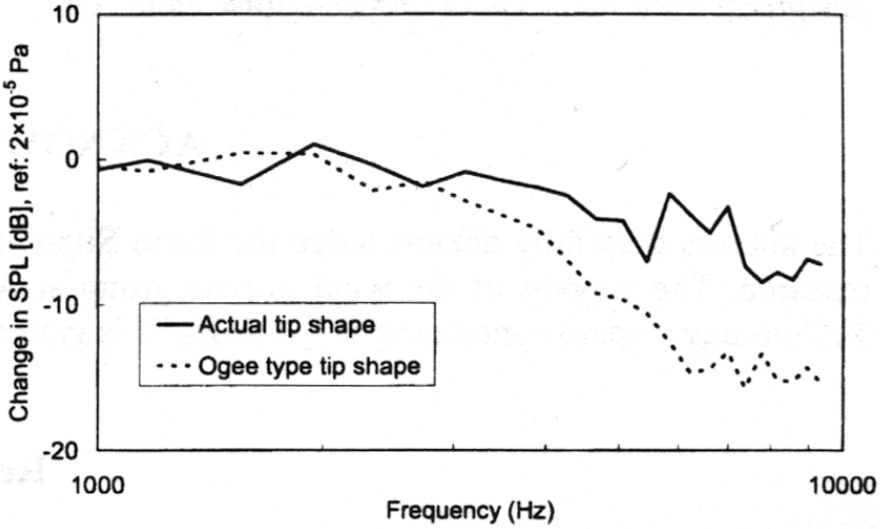

Figure 5.22 Far-field sound pressure levels (20 m upstream of turbine) for rotor with actual blade shape and ogee tip (Source: Iida et al, 2005)

5.2 Design Loads

The design loads for the project were determined by a combination of aeroelastic simulations using NREL's FAST (Fatigue, Aerodynamics, Structures, and Turbulence) code and MSC.ADAMS, a multi-body simulator that can be used to simulate very complex mechanical

systems and has been mated to the NREL aerodynamics package AeroDyn to support simulation of horizontal-axis wind turbines. Five revisions of the dynamic model were developed for the prototype STAR blades and are shown in Table 5.7. The prototype blades used the STAR 7 planform in which the root region was based upon the Euros EU-51 design.

Table 5.7 Aeroelastic model revisions for the STAR prototype blades.

Revision	Date	Simulaton Code	Rotor Diameter (m)	Rated Rotor Speed (RPM)	Comments
A	02/04/2008	FAST	56	32	Initial Investigation, no blade torsion DOF
B	02/28/2008	FAST	54	32	Design loads for fatigue test, no blade torsion DOF
C	05/28/2008	ADAMS	54	32	1st ADAMS run with blade torsion DOF
D	03/01/2009	ADAMS	54	34	ADAMS model with rotor RPM to match field data with density @5000ft
E	03/05/2009	ADAMS	54	34	ADAMS model with rotor RPM to match field data with density @sea level

The simulations were used to identify both fatigue and ultimate loads at various stations along the wind turbine blades. The results of these simulations were the basis for the blade fatigue testing and to help understand/validate field test data.

5.2.1 Design Load Cases

Five of the IEC load cases were selected as the design basis for aeroelastic simulations and are summarized in Table 5.8.

Table 5.8 Design Load Cases (DLCs) for aeroelastic simulations

Design Load Case (DLC)	Acronym	Mean or Initial Wind Speeds (m/s)	Wind Directions	Return Periods (years)	Type of analysis
Normal turbulence model, IEC class IIA	NTM	3, 5, 7, 9, 11, 13, 15,17, 19, 21, 23, 25 (@5 turbulence seeds each)	N/A	N/A	F
Extreme coherent gust with direction change	ECD	12, 16, 20, 24	positive & negative	N/A	U
Extreme direction change	EDC	12, 16, 20, 24	positive & negative	1 & 50	U
Extreme operating gust	EOG	12, 16, 20, 24	N/A	1 & 50	U
Extreme wind model	EWM	42.5 (@5 turbulence seeds each)	turbulent	50	U

5.2.2 Control System

The controller used in the STAR study was based on the work accomplished by Craig Hansen for the NREL WindPACT study [11]. Much of the following discussion is based upon that earlier work. The control system used is typical of those used on wind turbines with full-span, collective pitch control in conjunction with variable-speed generators. Therefore, all the pitch controllers in this study have as their primary goal the control of generator speed:

- below rated , the system attempts to operate at constant tip speed ratio (fixed pitch)
- above rated wind speed, the pitch controller attempts to maintain constant rotor speed ("rated speed")

The generator/power-electronics systems in this study have torque proportional to the square of generator speed below rated, then constant (or very slowly increasing) torque above the rated generator speed. This makes it possible to operate at constant tip speed ratio below rated as long as the blade pitch remains constant. Above rated, the system power output will change only in proportion to rotor speed since the torque remains essentially constant. Hence, power regulation is entirely dependent upon speed regulation.

The pitch control systems are implemented in the form of linear transfer functions in ADAMS and FAST models. The same control subroutines and controller data files are used in both codes to calculate the pitch demand. In ADAMS, this pitch demand is sent to an actuator, which applies a pitching moment to the blade. In FAST_AD the pitching dynamics are not calculated directly. Instead, the actuator is represented as a linear transfer function between pitch demand and actual pitch. The ADAMS actuator and the FAST actuators are selected to have essentially identical characteristics.

Figure 5.23 shows the control diagram for the basic speed controller. Figure 5.24 is similar, but tower acceleration is input to the pitch demand controller in an attempt to damp longitudinal vibration of the tower. Both systems use basic PID control with gains denoted in the figures as K_I, K_P, and K_D. When implemented numerically, a modified form of the derivative term, $K_D s/(1+\tau s)$ was used, where τ is a time constant that is small compare with other significant time scales in the system. We implement all the controls in discrete time. The typical time step is 0.025 sec.

Generator speed error is input to the basic controller. The PID controller determines the desired pitch angle, feathering the blade (increasing pitch) when the generator speed is too high. The pitch demand is limited to the range of θ_{min} to 90°. θ_{min} is the pitch angle at which optimum rotor aerodynamic performance is achieved when operating at constant tip speed ratio. When the rotor speed is below the desired setpoint, the pitch will remain constant at $\theta_{min.}$ The generator torque characteristics must be matched to the rotor torque in order to actually achieve constant tip speed ratio operation.

The presence of the pitch demand saturation function requires that integrator anti-windup be included in the controller. This is shown as the feedback with gain K_{AW} in the figures. Note that this anti-windup term is fed back to the integrator only. This prevents the integrated speed

error from accumulating when the rotor is operating in low winds, below rated speed. We have used a gain of 0.3 rpm/deg in all of our simulations. The results are insensitive to this gain when implemented in this manner.

The rotor characteristics are a strong nonlinear function of wind speed, hence blade pitch. This requires that the PID gains be "scheduled" as a function of blade pitch angle. Each of the PID gains is multiplied by a function, GS, of the form:

$$GS = \begin{cases} 1 & \theta < \theta_1 \\ a\theta^p & \theta_1 \le \theta \le \theta_2 \\ a\theta_2^p & \theta > \theta_2 \end{cases}$$

where a, p, θ_1, and θ_2 are constants input by the user. Coefficients a and p must be selected such that the exponent p is negative. It should be selected such that the product of the gain schedule value, GS, and the rotor "gain", (the sensitivity of rotor torque, Q, to blade pitch, θ), is nearly constant for all wind speeds in the operating range.

The pitch actuator in the models is a simple second order system:

$$H_a(s) = \frac{\omega_n^2}{s^2 + 2\xi\omega_n s + \omega_n^2}$$

with ξ = 80% of critical damping and a natural frequency that is a multiple of the rotor speed. In most cases we have used $\omega_n = 4\Omega$, where Ω is the rotational velocity.

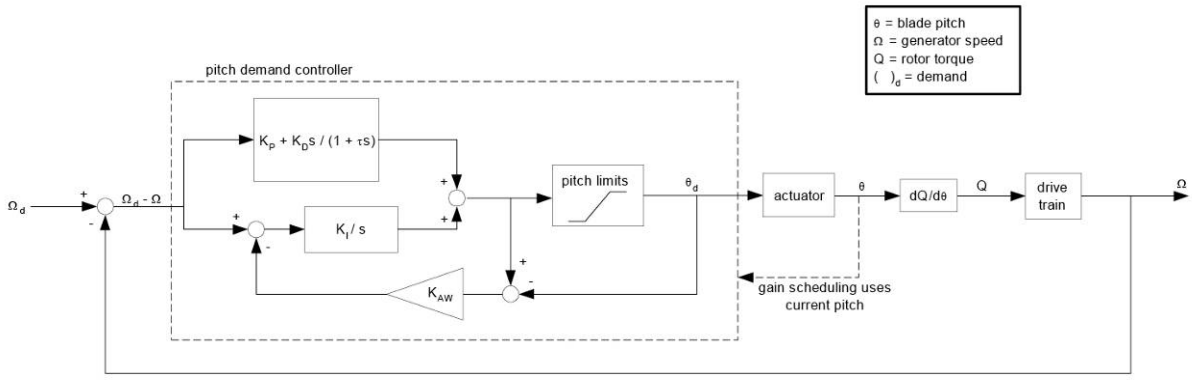

Figure 5.23 Pitch controller for speed regulation.

The turbine drive train is represented as a single torsion spring, k, between the generator inertia, I_g, and rotor inertia, I_r. The generator torque is represented as a linear function of generator speed, with slope =A.

The resulting transfer function between rotor torque and generator speed is:

$$H_{DT}(s) = \frac{\frac{k}{I_r}}{I_g s^3 + As^2 + \left(1 + \frac{I_g}{I_r}\right)ks + \frac{Ak}{I_r}}$$

Many of the rotors we are modeling have a tower natural frequency close to 1 cycle per rotor revolution (1P). These systems experience substantial tower motion parallel to the wind direction. The tower motion appears as a cyclic wind speed input to the rotor and causes rotor speed oscillations, which in turn cause pitch oscillations. This motion can be exacerbated by a highly responsive pitch control system. We generally find it necessary to reduce the speed control effectiveness in order to avoid excessive tower fatigue loads. Finding the best balance between tower loads and effective speed control is subjective and largely a matter of trial and error with system simulations.

To alleviate this problem, we have implemented tower acceleration feedback. This is illustrated in Figure 5.24. The tower dynamics (in the "tower fore-aft motion" box) are represented as a transfer function from rotor thrust to tower-top velocity:

$$H_T(s) = \frac{\frac{s}{k_t}}{\frac{s^2}{\omega_t^2} + \frac{2\xi}{\omega_t}s + 1}$$

Here k_t is the effective stiffness of the tower, ω_t is the natural frequency, and ξ is the structural damping ratio. The rotor thrust is a linear function of the blade pitch (at a given wind speed) with a slope of determined from steady-state aerodynamics calculations at the desired wind speed and pitch angle.

The tower acceleration is input to a lag compensator to determine a change in pitch in response to the motion. This compensator is of the form:

$$H_{LC}(s) = \frac{s + \frac{1}{T}}{s + \frac{1}{\alpha T}}$$

where $\alpha > 1$ and T is a time scale related to the period of tower motion.

Two additional derivatives are needed to run a simple linearized model of this system. The sensitivity of rotor thrust to changes in pitch angle was mentioned above. We also need the sensitivity of rotor torque to wind speed (or tower speed). Using this technique, all of the aerodynamic characteristics of the system are represented by simple constants determined by steady-state simulations. Obviously this approximation neglects unsteady and nonlinear aerodynamic effects, which are known to be important to the system dynamics. As a result, the controllers must be verified and fine-tuned in full system simulations over the entire operating range of the system.

We have found that we can use this feedback to reduce tower loads or to improve speed regulation without increasing tower loads. However, the selection of the controller parameters remains at least in part a matter of trial and error. We generally find that we can decrease loads in one area at the expense of increased loads elsewhere. Selection of the best design depends on the lowest cost of energy, obviously not a simple thing to evaluate.

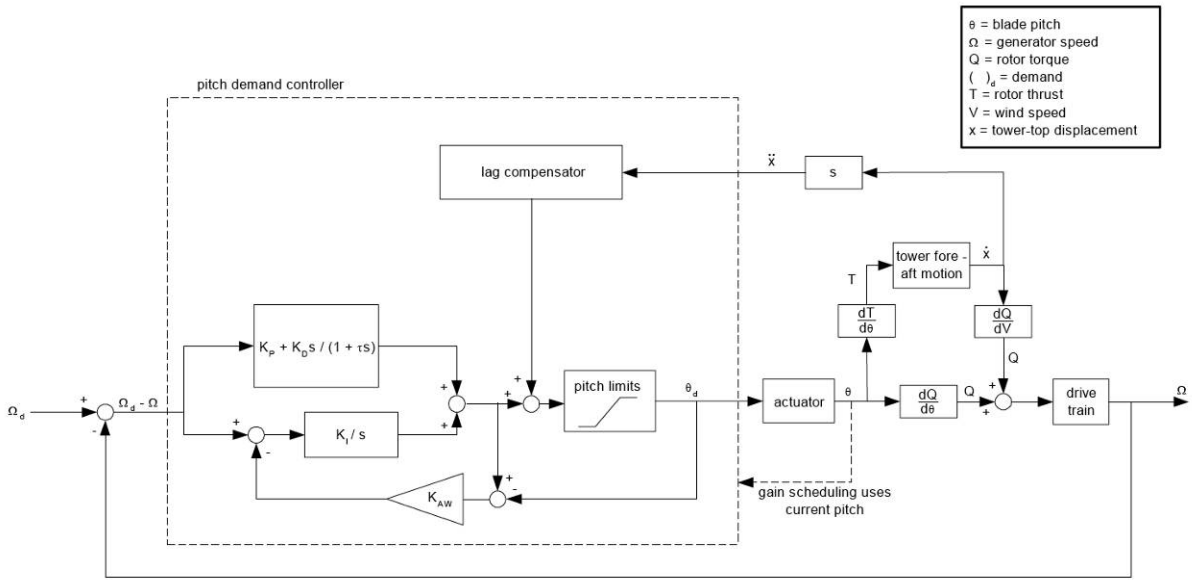

Figure 5.24 Pitch controller with tower feedback.

5.2.3 Dynamic Modeling

The ADAMS code was used to model the Z50 turbines with the existing and new STAR blades to determine the effects of sweep twist on loads and performance, as shown below in Figure 5.25.

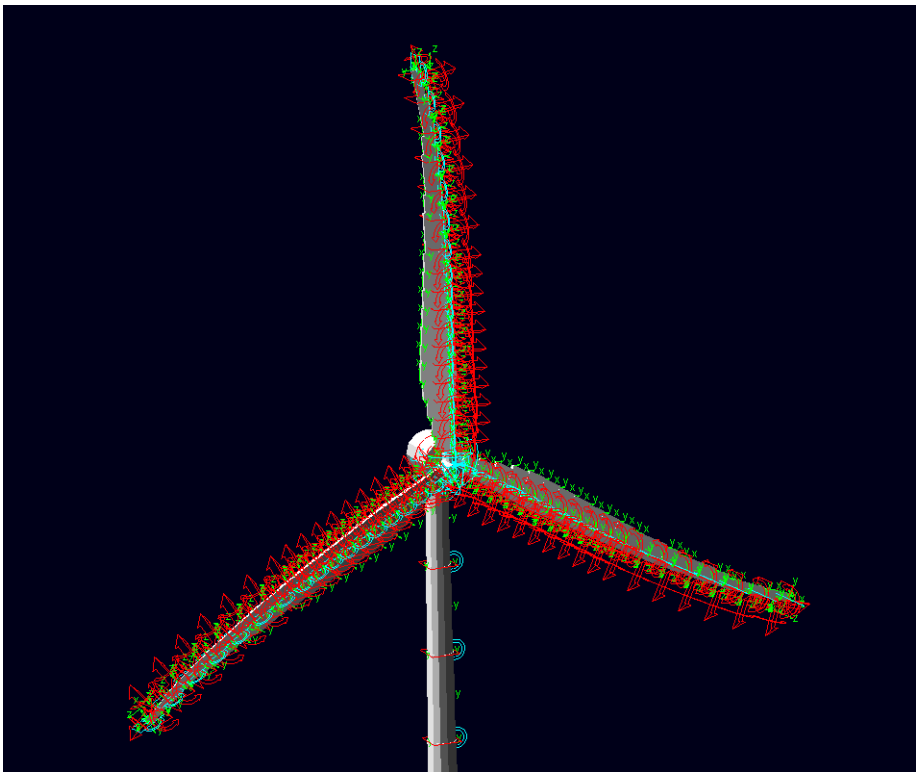

Figure 5.25 ADAMS STAR turbine model.

The drivetrain for ADAMS model was loosely based on the Zond Z-50 wind turbine (Figure 5.26). The model assumed a conventional setup with low-speed shaft, gearbox, high-speed shaft and generator. As described above, the drivetrain is modeled as a spring, mass and damper system. The drivetrain was assumed to be 100% efficient mechanically and 95% efficient electrically.

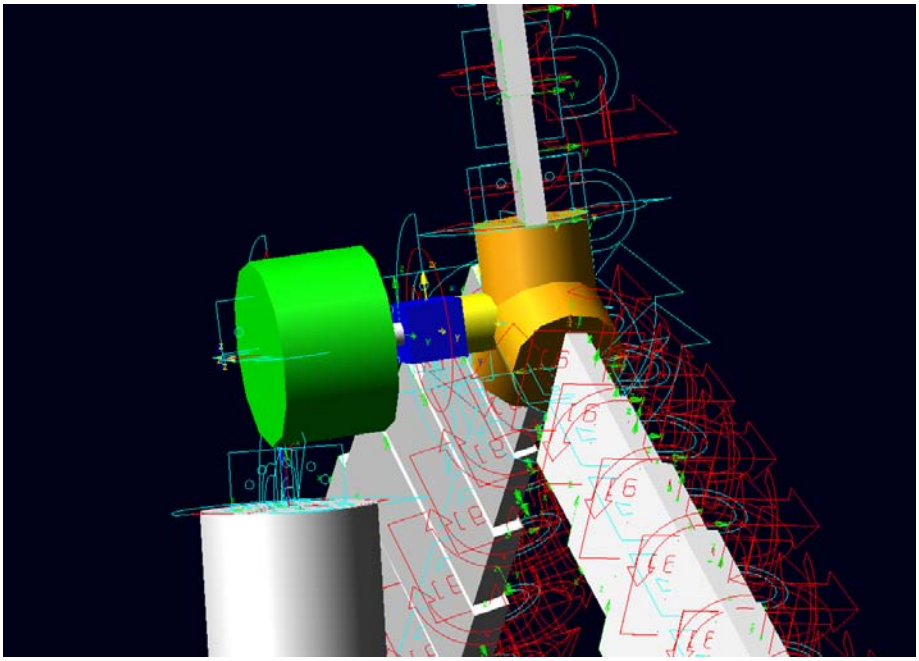

Figure 5.26 ADAMS STAR drivetrain model.

The blade model in ADAMS consists of 20 point mass rigid bodies connected by springs that provide flexibility for 6 degrees-of-freedom each, as shown in Figure 5.27.

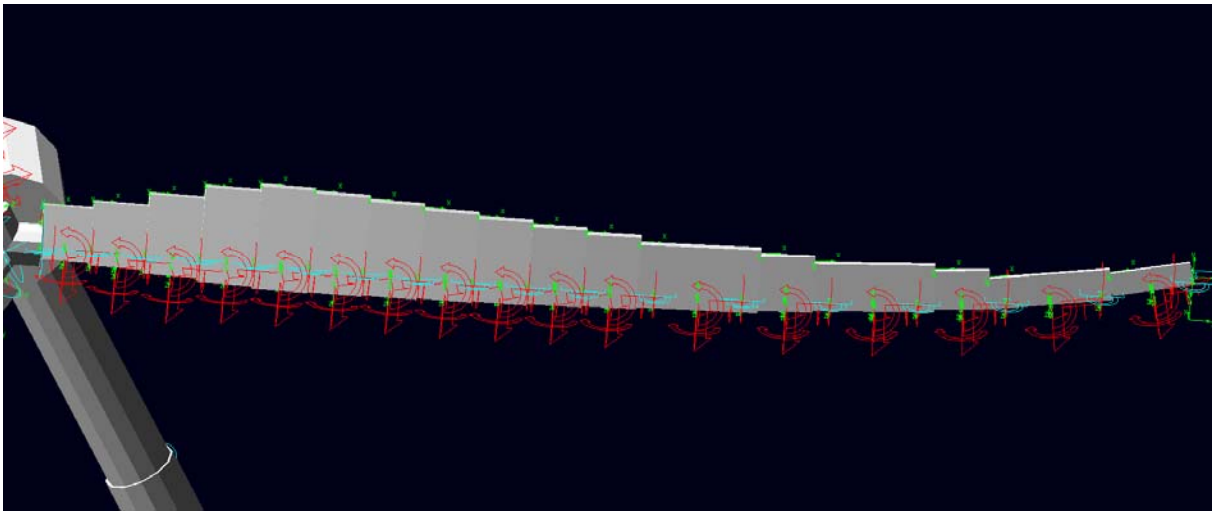

Figure 5.27 ADAMS STAR blade model

The tower was modeled similarly to the blades with ten rigid bodies connected by springs that provide the flexibility. The test turbine was mounted on a lattice tower, so it was not expected that the tower model in ADAMS would be adequate to fully model the dynamics. The main focus of the tower modeling was to match the tower 1st fore-aft and 1st side-to-side natural frequencies.

The aerodynamic model used seventeen blade-elements to represent the aerodynamic forces on each STAR blade. Turbulence was modeled in all simulations above 9 m/s, and the Bedddoes dynamic stall model was used for all but the standstill extreme wind cases.

In general the prototype design (STAR 7) blade simulations showed good stability and convergence. The blade curvature did, in fact, reduce the blade fatigue loads by about 12% from the baseline straight blade. The STAR rotor also had the added advantage of reducing drivetrain oscillations and improving controllability of rotor speed near rated wind speed. Calculated and measured blade root bending moments are compared in Section 6.

5.3 Structural Analysis

5.3.1 Shell Construction

The STAR blade design used E-glass/epoxy composite and a stressed-shell construction approach. With this design approach the blade is constructed from two structural shells, which are connected internally by a shear web bonded between the shells (Figure 5.28). The spar cap is constructed from unidirectional fiber which is oriented in the spanwise direction. Typically there are two shear webs bonded between the blade shells, but the STAR blade uses a single web to provide improved torsional response.

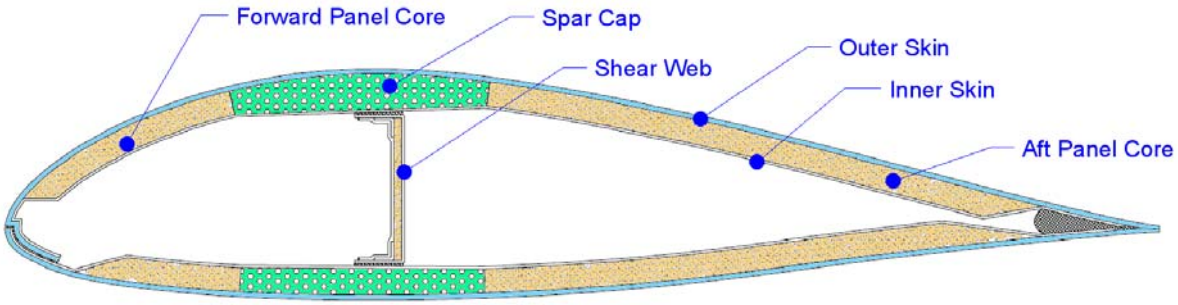

Figure 5.28 Typical blade section.

The STAR prototype blades were fabricated using the T-bolt root attachment design developed by Euros. The joint is formed by drilling a series of large diameter holes (60 mm) across the blade root laminate parallel to the blade flange 140 mm outboard from the flange surface. Another set of smaller holes (30 mm) is drilled perpendicular to the flange to intersect the cross laminate holes.

5.3.2 Finite Element Model Approach

The original finite element model (FEM) analysis was based upon the STAR 6 planform and for budgetary reasons the FEM did not include the root attachment details. The primary objective of the FEM analysis was to confirm the bending and twisting behavior predicted by section analysis. Additional calculations were conducted to assess panel buckling and perform detailed stress analysis. The FEM includes three dimensional geometric effects that were not modeled by section analysis. The model can also be used to generate equivalent beam properties for use in the dynamics model and to perform buckling stability analyses for

key load cases. The potential shear buckling due to the increased twist inherent in the design can also be investigated. The FEM allows independent verification that the design meets basic strength and stiffness requirements.

The finite element model was focused on the outboard portion of the blade, which is the unique feature of the STAR blade. Structures such as wind turbine blades are typically modeled using traditional shell or plate elements with offsets from the outer surface to account for the shell thickness. Recent findings by Laird, et. al. [12] have demonstrated that this technique can produce erroneous results, particularly in torsion, which is key to predicting the twisting response of the blade.

For this project, the blade was modeled using ABAQUS, a commercial finite element software package. A full 3D solid model was developed, including interior nodes to represent the material layer thicknesses at each location, as shown in Figure 5.29.

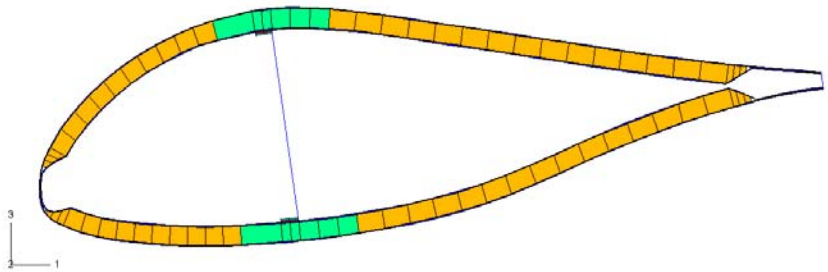

Figure 5.29 Typical cross-section of FEM showing thickness definition.

This approach enables the use of a variety of solid element types and avoids the use of traditional shell elements with offsets, thus ensuring more accurate predictions of the torsional response. The skins and spar caps were initially modeled using the continuum shell elements available in ABAQUS version 6.5. These elements are similar to solid elements (i.e., "bricks") in that they have eight nodes and a discrete thickness. However, the FE theory used is the same as for traditional, general purpose shells, which enables high aspect ratio elements (large length or width to thickness ratios), which are often desirable in skin-type structure. These elements generally performed well in the blade model. However, the limitations of shell theory with regard to radius of curvature led to ABAQUS element shape warnings and erroneous stress/strain results at the leading edge near the tip. The continuum shells in the skins and spar caps were subsequently replaced with traditional solid elements, which eliminated these problems. An assessment of the element aspect ratios showed that the element length/width-to-thickness ratio does not exceed 50:1, which is reasonable for solid elements in this application since there are no high stress/strain gradients.

5.3.3 Model Development

The geometry of the blade model was established by airfoil data at a number of key station locations along the span. The FEM mesh was generated using a script developed specifically for this project. The airfoils were rotated and translated according to a prescribed twist angle and sweep distance, respectively, at each station. Chordwise splines were defined along the surface of each airfoil in order to provide a continuous geometric function for locating nodes

on the FE mesh. Key node locations were chosen based on geometric and material transition points around the airfoil (Figure 5.30). The chosen mesh density determined the total number of nodes around each airfoil, which was the same at every spanwise station.

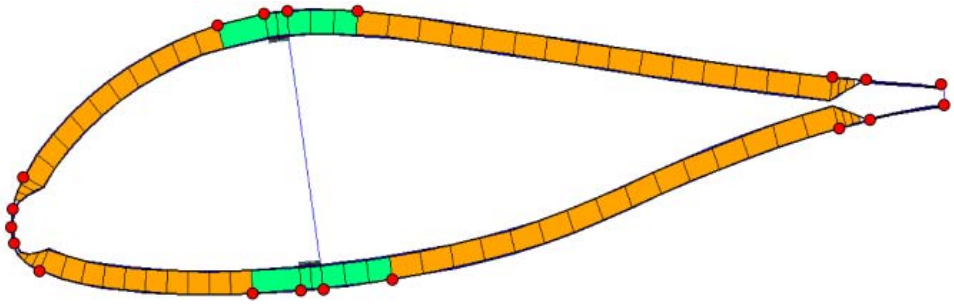

Figure 5.30 Finite element model key nodes.

Once the location of the nodes on each airfoil had been determined, spanwise splines were used to provide a continuous geometric function between the corresponding node on each airfoil. The finite element mesh was then defined between the key stations based on the chosen mesh density. Material properties were assigned to the elements to represent the laminate at any given location. Linear interpolation was used to determine the spar width at locations between the spanwise stations where the material definitions were defined. Material thickness and/or property changes were defined over one spanwise element (~3 inches) and were held constant until next outboard material station.

The skins, spar caps, and core were modeled with continuum solid elements (ABAQUS element type C3D8R) as shown in Figure 5.31. The skins were modeled with one solid element through the thickness. The individual plies of the skins (DB/Uni, random mat, gelcoat) were represented as a single equivalent uniform material through the thickness. The spar cap was modeled with one solid element though the thickness with orthotropic material properties (E-glass roving). The core was modeled with one solid element though the thickness with isotropic properties (foam). The web flanges were modeled using continuum shells (SC8R) with a single orthotropic material (double bias fabric). The spar web was modeled with layered traditional shell elements (S4R) with mid-thickness nodes and included both web face sheets as well as the core in a single element through the thickness. The adhesive at the spar flange-to-skin joint was modeled using solid elements (C3D8R) with isotropic properties.

All of the elements used were first-order, reduced integration elements that are geometrically linear between nodes. As such, a mesh density was chosen that is sufficient to represent the curvature of the blade reasonably well.

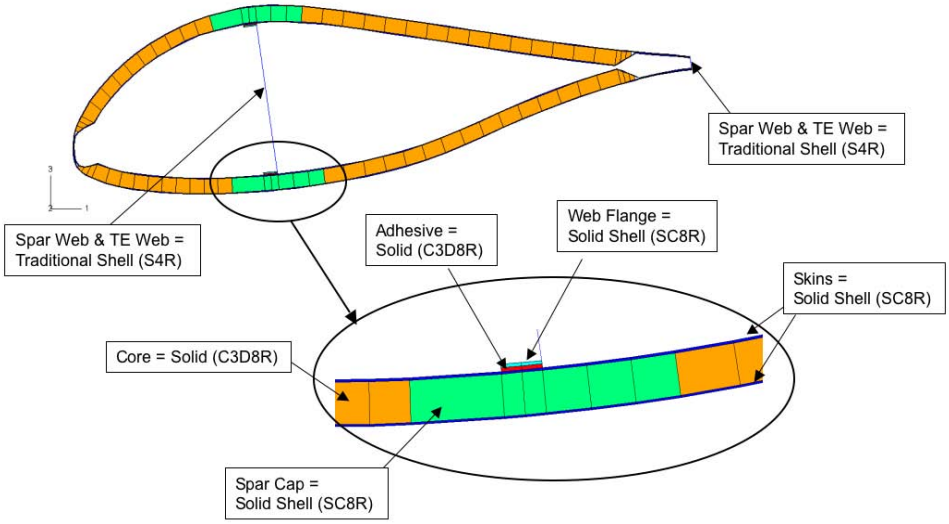

Figure 5.31 Typical blade finite element model section.

The baseline FE model was geometrically linear and used linear material properties. For comparison, a geometrically nonlinear run was performed with the operating load case. It showed a negligible effect of due to large deformations (bending and twisting), so the linear model was deemed to be sufficient. All load cases were assumed to be steady-state; dynamic effects due to delayed twisting response were not modeled. The model, shown in Figure 5.32, consisted of 87,728 elements with 123,052 nodes representing 394,734 degrees of freedom. The linear geometry solution required 4 minutes using an HP Itanium computer.

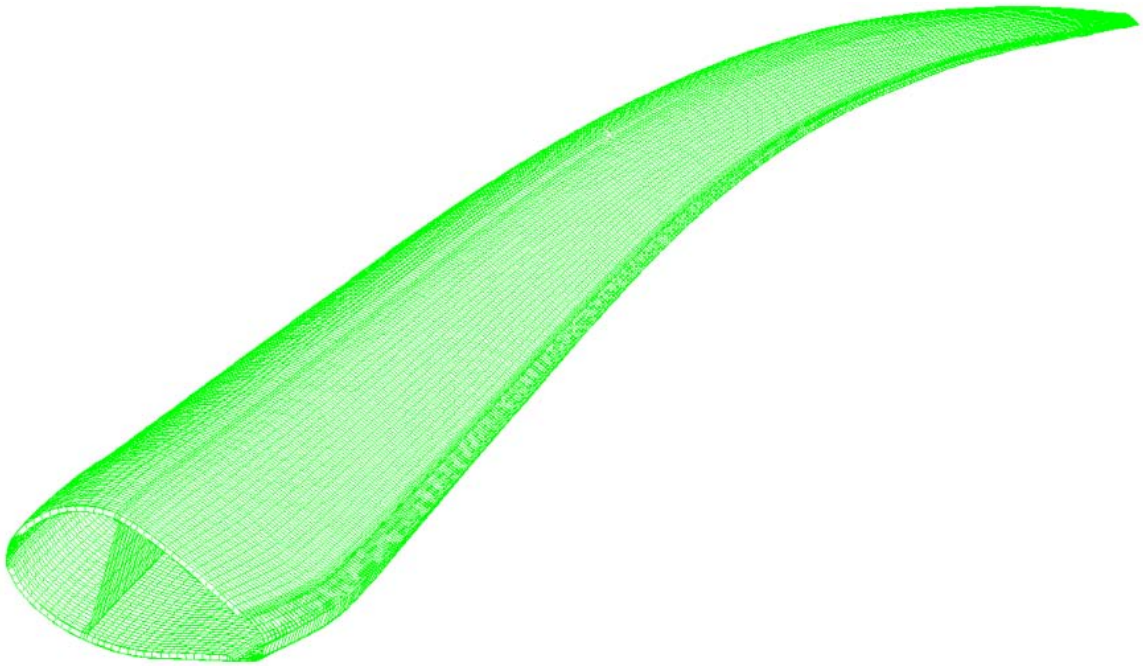

Figure 5.32 Blade finite element mesh overview.

5.3.4 Modeling Simplifications

Development of the FEM required several simplifications to efficiently model the blade. The first simplification was to eliminate modeling the inboard region near the root attachment. The STAR 6 blade was modeled as having a fixed boundary condition at 15.16% span, as shown in Figure 5.33.

Figure 5.33 Illustration of the root region not included in the finite element model.

The FEM used a simplified approach to model the shear web flange. The flange width was reduced from 2.0 to 1.5 inches outboard of 85% span. This change assured that the shear web flange width would not exceed the edges of the spar cap, which was a meshing requirement. The FEM also made small adjustments to core ramp angles to improve mesh, using a nominal ramp angle of 30 degrees (Figure 5.34). Adhesive in the joints at the leading and trailing edge was not modeled (Figure 5.35).

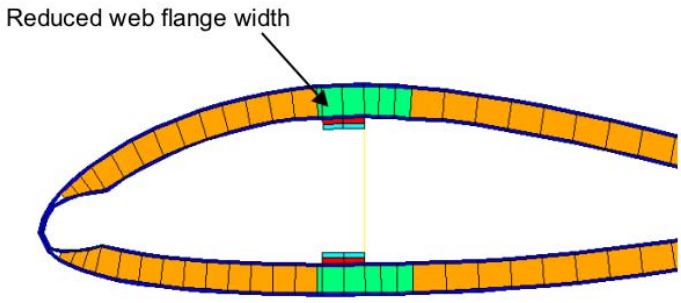

Radius r/R (%)	Core Ramp Angle (degrees)
15%	30
20%	30
25%	30
35%	35
45%	35
55%	30
65%	25
75%	25
85%	25
95%	25

Figure 5.34 Modifications to the input data.

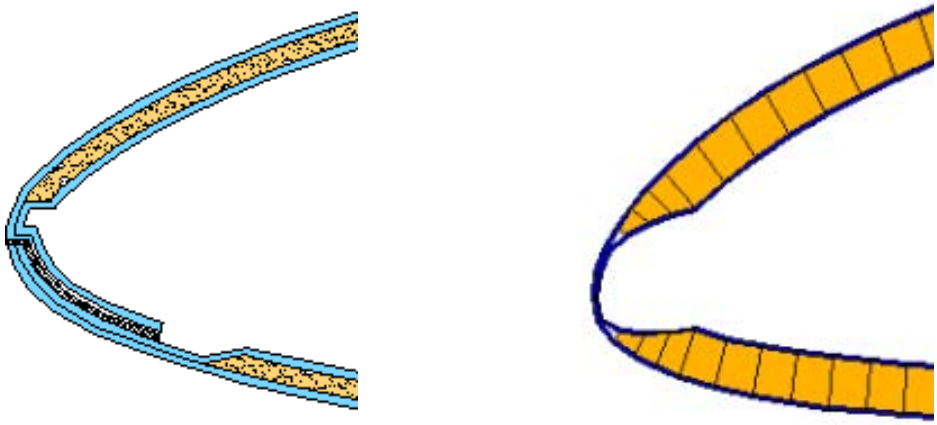

as-designed as-modeled

Figure 5.35 Leading edge bond not modeled.

The spar cap/core thickness is transitioned at several spanwise locations. These transitions were modeled as occurring over one element length, or about 3 inches with this mesh. Figure 5.36 shows a transition from 1.50 inches to 1.25 inches that occurs at 55% span (r/R).

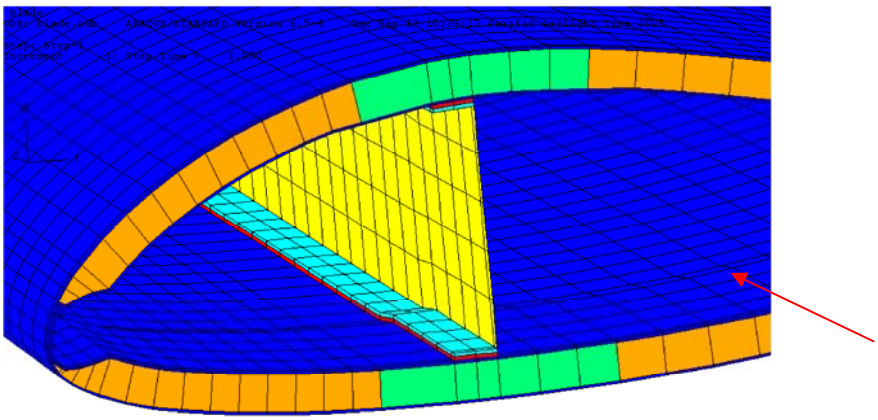

Figure 5.36 Modeling approach for the spar/core thickness transition.

Based on the material definition data from the preliminary design, the inner skins and core overlap to varying degrees at the trailing edge outboard of r/R = 35%, as shown in Figure 5.37. The outer skins never overlap since they are defined by airfoil data. The additional core material has negligible effect on global response and the model was not adjusted to compensate for this issue. The amount of skin material is approximately correct.

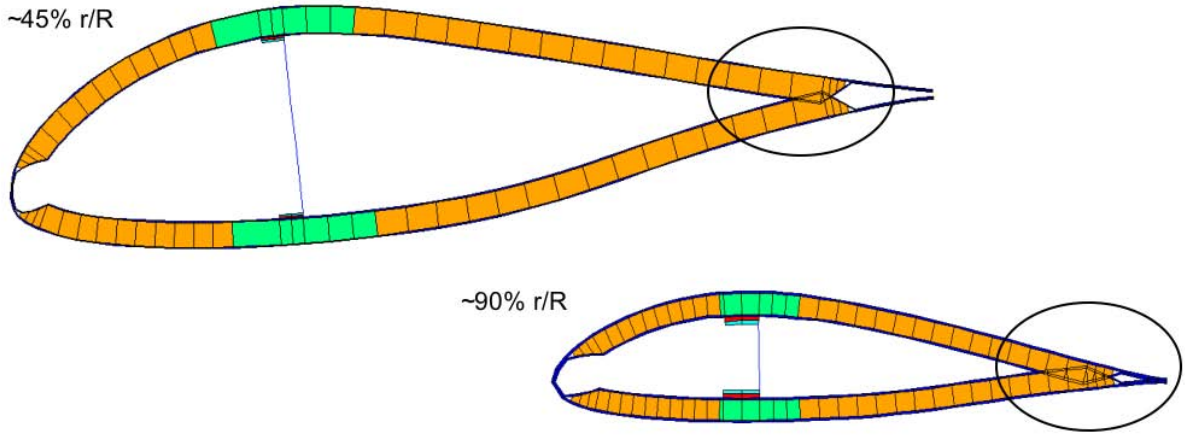

Figure 5.37 Model shell overlap.

The inboard airfoils have a flat back regions that were connected with a fiberglass web made from 4 layers of double bias material (t = 0.140 inches) as shown in Figure 5.38.

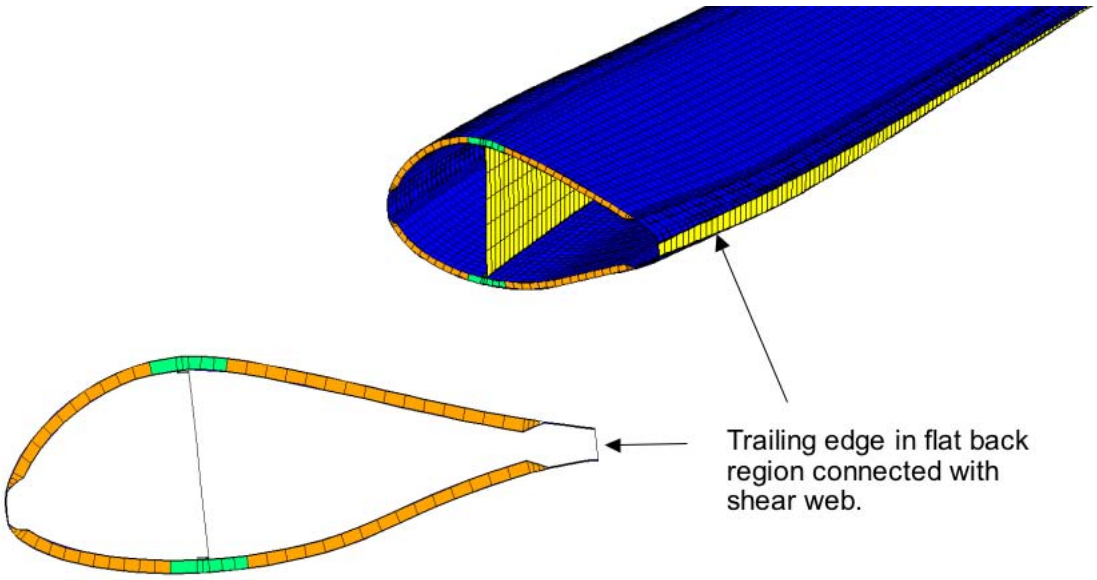

Figure 5.38 Modeling approach at the trailing edge flatback.

5.3.5 Modeling Applied Loads

Two load cases were applied to the model: 1) an operating load case, and 2) an extreme wind load case. The operating load case was represented as a line load applied at the spar centerline on the high pressure surface. The extreme wind load case was modeled using pressure applied to the upwind surface of the blade. For the operating load case, twist adjusted segment loads were determined at a number of spanwise stations. Segment loads were then converted to spanwise distributed loads. The spanwise distributed line load was applied normal to the high-pressure surface of the airfoil to nodes located at the intersection of the spar cap and spar web centerlines, as shown in Figure 5.39. These nodes were coupled with kinematic constraints as shown such that the applied loads will be distributed through the skin and spar flange thicknesses (the sets of coupled nodes on the two surfaces are not coupled to each other). The potential pitching moment due to the offset between the spar centerline and of the center of pressure was not included in the loading.

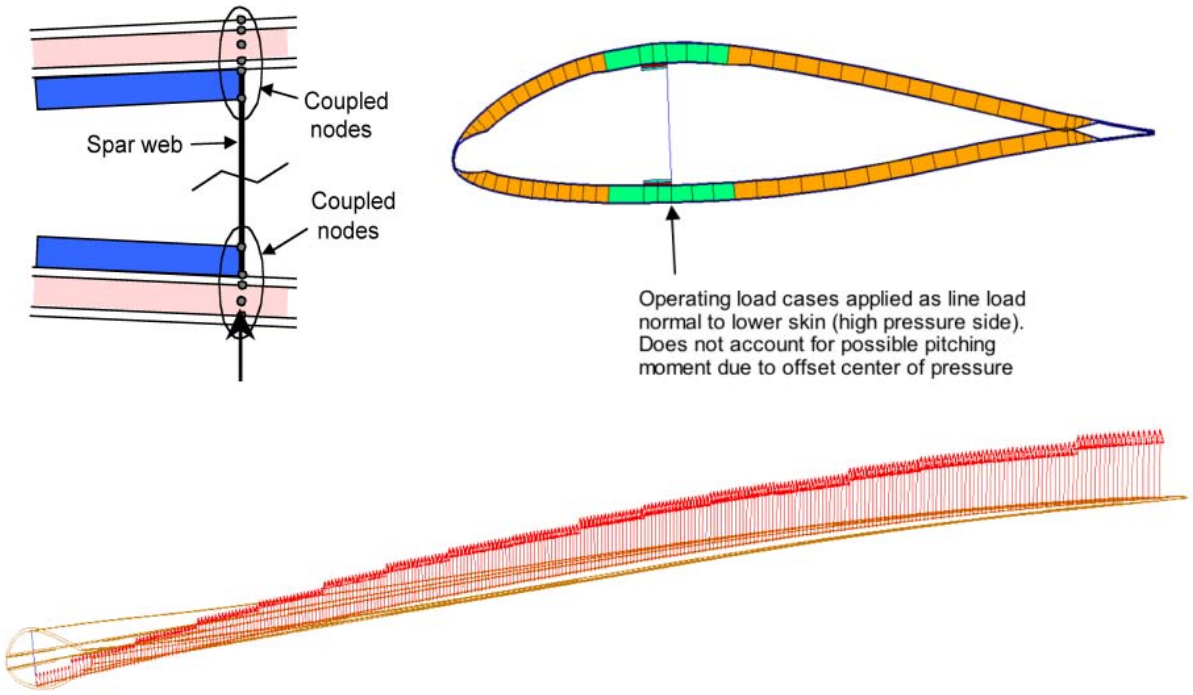

Figure 5.39 Application of operating loads in the finite element model.

For the extreme wind load case, a surface pressure was applied uniformly to the high-pressure side of the blade in each segment. The surface pressure was calculated assuming IEC Class II extreme wind conditions (conservative because target class for STAR rotor is Class III) with the blade positioned vertically upward.

5.3.6 Material Properties

Linear material properties were used in all cases (e.g., the nonlinear stress-strain behavior of the adhesive was not modeled). Orthotropic properties for the skins were calculated using classical laminated plate theory (CLPT) based on the ply properties shown for the layers defined in the preliminary design material definition data (i.e., smeared laminate properties were used). For the spar caps, the E-glass roving properties were used directly. The spar web and trailing edge web in the flatback region were defined using layered elements with each layer (e.g., skin, core) defined discretely. All of the orthotropic properties used (laminate and lamina) were defined with the `'ENGINEERING CONSTANTS'` material format in ABAQUS. The isotropic core adhesive properties were entered using the `'ISOTROPIC'` material format.

Material orientations for each element were assigned to match the actual ply orientations expected in the blade. In the inboard portion of the blade, the plies will generally be orientated such that the 0° direction is aligned to the rotor radius. In the swept area of the blade, the 0° direction must follow the curvature of the leading edge, as shown in Figure 5.40. In general, the skin and spar cap elements in the FEM were defined such that two edges are parallel to the leading edge and the other two edges are orientated streamwise (perpendicular to the blade radial direction). Using the `'OFFSET TO NODES'` orientation approach in ABAQUS, the material orientations were defined to align with the element edge best

representing the actual material orientation. For the skins and spar caps, the direction parallel to the leading edge was used, since it best represents the actual 0° fiber direction.

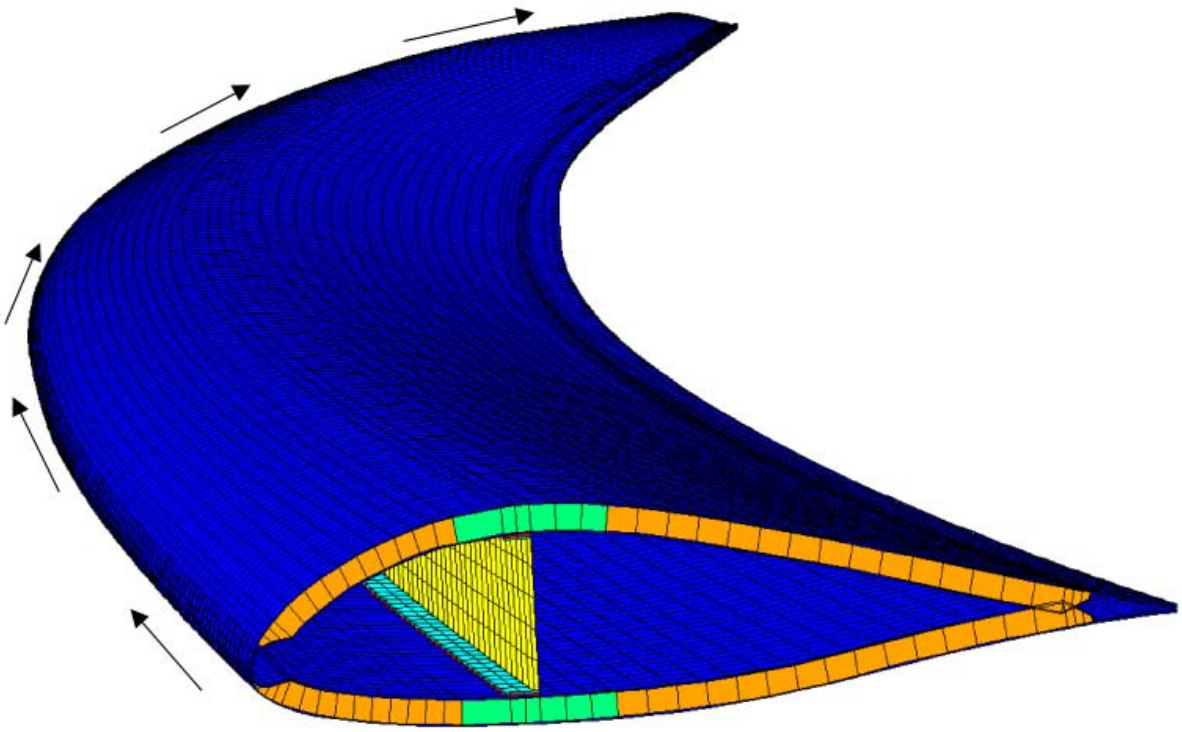

Figure 5.40 Material orientation diagram.

5.3.7 FEM Analysis Results

The flatwise deflection of the model for the maximum operating load case is shown in Figure 5.41. Agreement with the tip deflection result from section analysis was excellent.

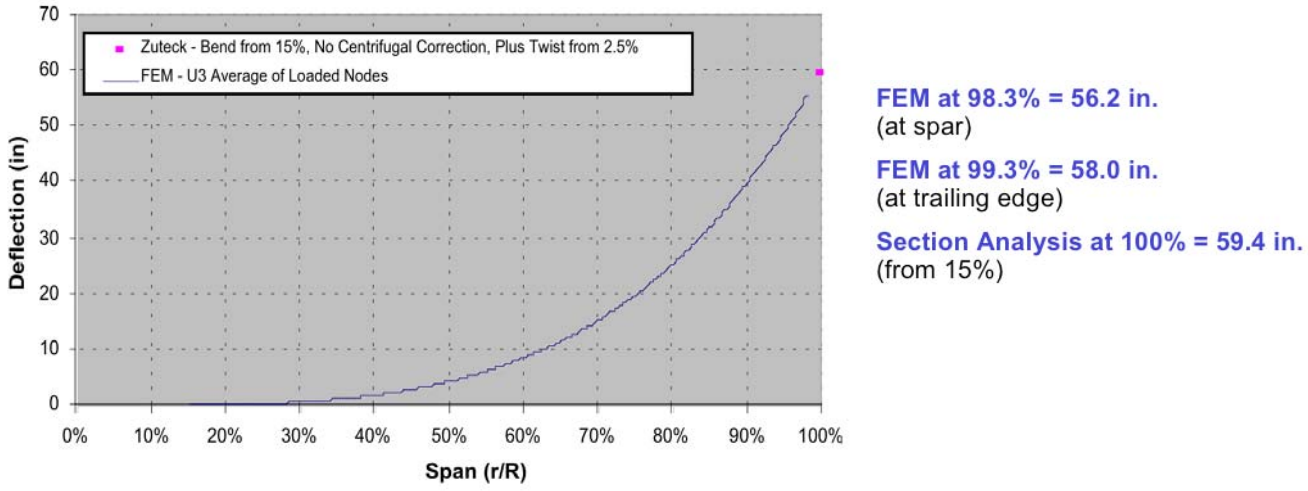

Figure 5.41 Blade deflection for the maximum operating load case.

Initial evaluation of the strains in the blade laminate for the extreme wind load case are given in Figures 5.42 through 5.44. Comparison with the strain values predicted by section analysis showed good results.

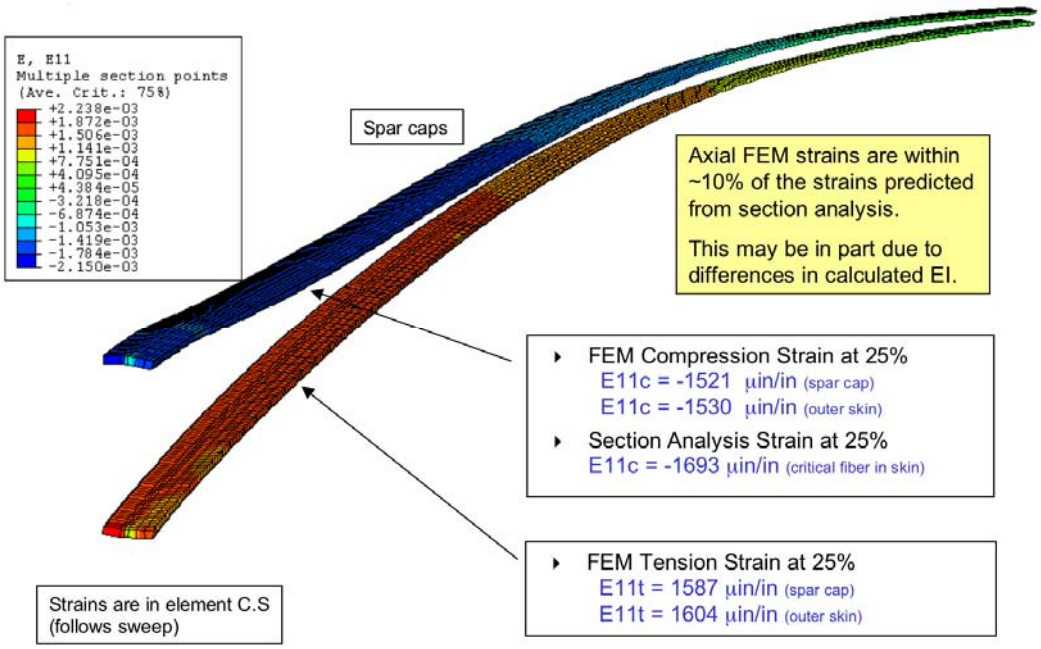

Figure 5.42 Spar cap strain for the extreme wind load case.

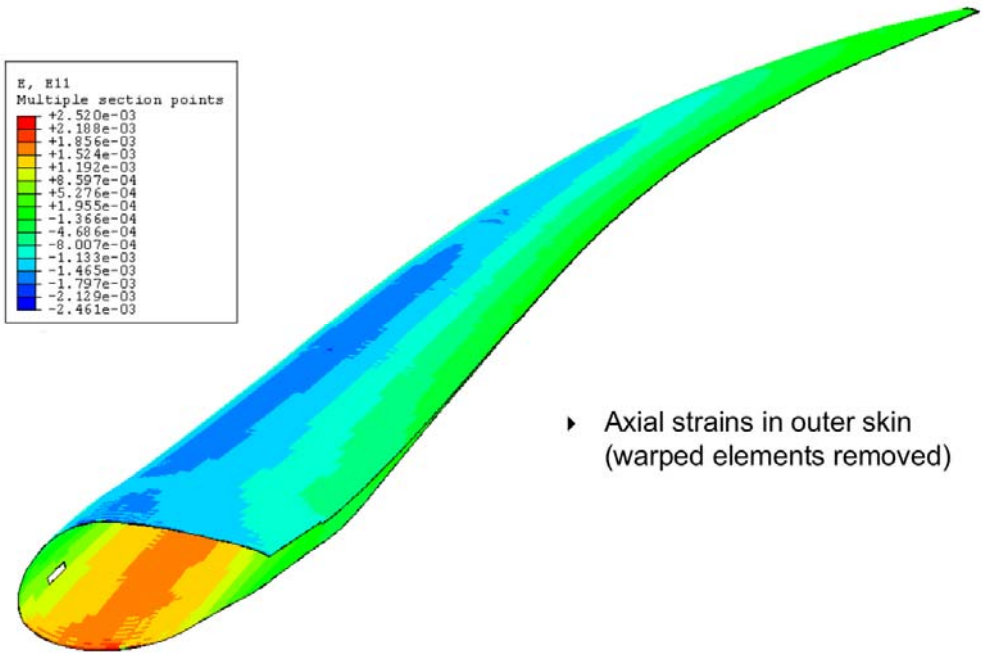

Figure 5.43 Outer skin axial strain for the extreme wind load case.

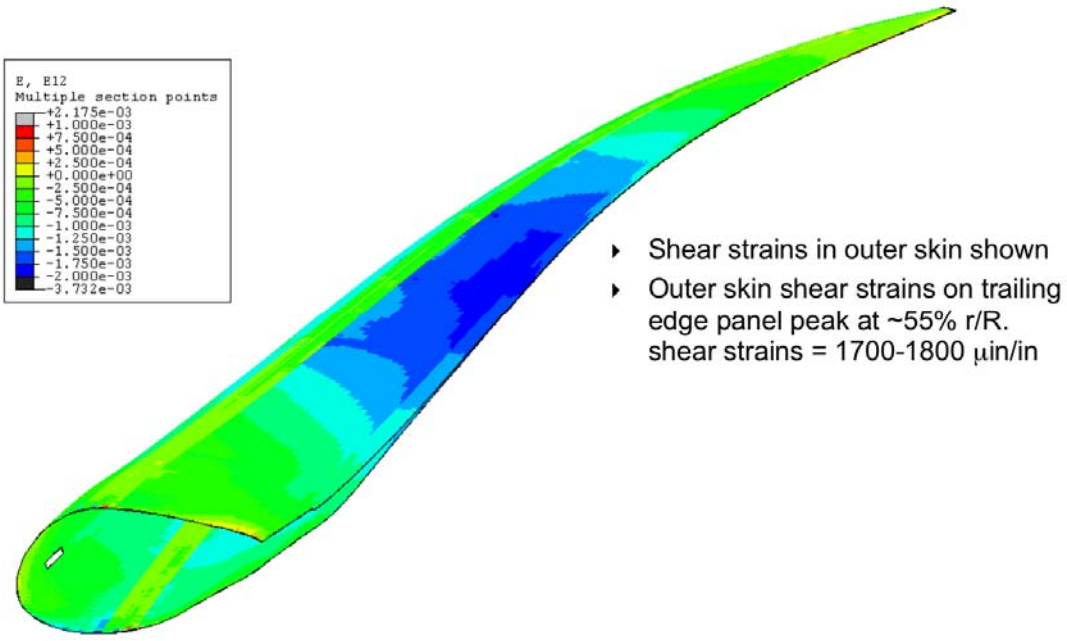

Figure 5.44 Outer skin shear strain for the extreme wind load case.

A wide range of detailed engineering studies were completed on the final STAR 7 blade design. Torsional stiffness and twist angle for the maximum operating case were calculated using both FEM and section analysis. In addition, we conducted an evaluation of the STAR 7 prototype blade design in accordance with IEC blade certification requirements using code specified load and material design factors. This work included strength and fatigue analysis of the blade and the root T-bolt connection. Stability analysis was completed using both a closed form buckling solution and the finite element eigenvalue buckling calculations. The predicted critical buckling strains were 5.7 times the strains from extreme wind conditions.

6 LABORATORY AND FIELD TESTING

6.1 Materials Testing

6.1.1 Fabric Curvature Testing

The curved planform of the STAR blade can create problems during the placement of fabric in the mold. Resin infusion has become the leading method for fabricating wind turbine blades, and a number of unidirectional E-glass fabrics were evaluated to investigate how they responded to curvature. Several different fabrics were subjected to the fiber curvature tests, as summarized in Table 6.1. The fabrics are held together using different approaches, such as cross-stitching or hot melt.

Table 6.1 Summary of unidirectional fabrics evaluated for the STAR blade.

Product ID	Fiber Type	Weave Type	Thickness (mm)	Weight (oz/sq.yd)	Architecture (oz/sq.yd)	
					0 ū	90 ū
SA-120	S-Glass	Uni-directional	0.3400	12.2	11.9	
A-260	E-Glass	Uni-directional	0.9144	25.6	25.3	
XCD-180	E-Glass	Uni-directional	n/a	18	16	2
ELT-2600	E-Glass	Uni-directional	0.762	26.77	21.93	4.16
ELT-5500	E-Glass	Uni-directional	n/a	55.3	50.97	3.36

SA-120 uses hot melt to hold the fibers together and A-260 is a 26 oz. E-glass unidirectional fabric that has been commonly used in wind turbine blades. The glass strands were somewhat less constrained than the SA-120 even though hot melt was also used. XCD-180 is an 18 oz. E-glass stitched fabric, with 16 oz. unidirectional fibers held in place by 2 oz of weft fibers. ELT 2600-7 is a 26 oz. E-glass stitched fabric with about 22 oz. of unidirectional fibers and 4 oz. of weft fibers. Compared to fabrics that use hot melt, the stitched fabrics provided the necessary curvature more readily.

6.1.2 Resin Selection

An epoxy resin system was chosen for infusion of the test materials. The Jeffco 1401-21/ 4101-21 Epoxy System for Infusion was cost competitive with other resin choices, including vinyl ester. This resin system was being used in wind turbine blade construction and was representative of the typical epoxy materials. A vinyl ester resin, RSM 784 7975, was also considered. Compared to vinyl ester the multifunctional epoxy-hardener system for infusion provides better fatigue and inter-laminar shear strength. We ultimately selected an epoxy resin system because the improved physical properties justified the modest additional cost.

A factor to consider using epoxy resin is the fact that it must be post cured to obtain the desired physical characteristics. This requirement drives the manufacturing tooling toward heated molds. We currently expect that production molds will incorporate a water jacket that incorporates several segments, each having separate controls to regulate the temperature. Cooler water can be circulated to control excess heat caused by exotherm in areas that contain thick laminations. For post curing, the entire mold can be heated to desired temperatures.

6.1.3 Core Materials

Core materials are used to stiffen blade skin panels to prevent compression buckling failure. Several types of core materials were evaluated during the course of this study. Core materials are generally made from either balsa wood or poly vinyl chloride (PVC) foam. Balsa is structurally superior to foam, but is subject to moisture damage when improperly protected. Thorough saturation of the balsa end grain with resin prevents the ability of water to migrate through the core material. Supply difficulties are a consideration in the selection of the core materials. Balsa availability has been limited in recent years and long lead times are sometimes required.

Balsa manufacturers have also developed techniques of aiding resin transfer for infusion. Thin slits are cut along the surface of both sides of the core as well as holes drilled through it (Figure 6.1). This allows the resin to move along the surface to wet out the laminate and the holes allow the passage of resin to the opposite side of the core.

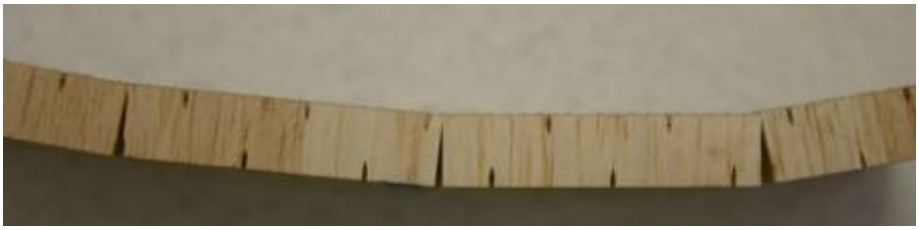

Figure 6.1 Side-view of balsa core material.

Foam core materials are generally more expensive than balsa and can be twice the cost in some cases. Lightweight foams typically have a relatively high resin absorption, which increases resin cost and blade weight. Air bubbles that are broken when cutting the foam into sheets must be filled with resin during infusion. This increases the weight of the foam significantly, especially when using thinner cores.

These problems have been addressed in some newer foams which create smaller bubbles in the lower density cores. It is also possible to obtain perforated foam, which can be used as a means of resin transfer during infusion (Figure 6.2).

Figure 6.2 Side-view of foam core material.

6.1.4 Laminate Property Testing

The stressed-shell construction approach was selected for the STAR blade developed in this project because it provides the lightest weight and cost. Given that basic design approach, it was determined that the structural laminates would be of two main types. We would need a

unidirectional material for the spar cap that would conform to the swept planform and a double bias cloth for the skin. A variety of candidate materials were reviewed. Ultimately, three unidirectional materials and two bi-axial fabrics were chosen to undergo laminate property testing as shown in Table 6.2 to determine strength and structural properties.

Table 6.2 Laminate property test summary.

Manufacturer	Product ID	Weave Type	Dry Thickness (mm)	Total Weight (oz/sq.yd)	Resin System	Tests*	Properties Tested**
Knytex	A-260	Unidirectional	0.91	25.6	Epoxy	Tensile, Compressive	1,2,3
Vectorply	ELT 5500	Unidirectional	1.5	55.3	Epoxy	Tensile, Compressive	1,2,3
Knytex	CD-550-100	Unidirectional	1.27	55.45	Epoxy	Tensile, Compressive	1,2,3
Knytex	DBM 1708	Bi-axial	1.12	25	Epoxy	Tensile, Compressive, Shear	1,2,4
Offshore Brand	BXMC-1708	Bi-axial	1.041	26.32	Epoxy	Tensile, Compressive, Shear	1,2,4

*** TESTS:** **Tensile:** ASTM D3039 **Type of Property:** Tensile Strength
Shear: ASTM D5379 Shear Strength
Compression: SRM 1R-94 Compression Strength, Compression Modulus

**** PROPERTIES** **1.** Tensile Strength **2.** Compression Strength
3. Compression Modulus **4.** Shear Strength

Knytex A-260 was selected as the initial baseline unidirectional fabric for evaluation. Knytex CD-550 and Vectorply ELT-5500 were candidate materials that were previously shown to conform to a curved planform. We also selected two types of double bias materials to test: Knytex DBM-1708 which is a typical blade material and Vectorply EBXMC-1708 which is a competitor.

Five (5) coupons were tested according to the American Society for Testing and Materials (ASTM) and Suppliers of Advanced Composite Materials Association (SACMA) testing standards for each material type. Three testing standards were used in developing the specimens: 1) ASTM D 3039/D 3039M – 00 Standard Test Method for Tensile Properties of Polymer Matrix Composite Materials, 2) ASTM D 5379/D 5379M – 98 Standard Test Method for Shear Properties of Composite Materials by the V-Notched Beam Method and 3) SRM-1R-94 SACMA Recommended Test Method for Compressive Properties of Oriented Fiber-Resin Composites. For each type of test and material a fixed number of coupons were developed as specified in the corresponding test standards summarized in Table 6.3.

Table 6.3 Summary of coupon quantity by test and material type.

EPOXY RESIN		COUPONS			TABS		
Fabric	Test #	Quantity of Coupons	Number of Laminations	Size of coupons	Quantity Tabs	Number of Laminations	Size of Tabs
A-260	ASTM 3039	5	2	15 X 250	20	1	15 X 56
	ASTM 5379	0	NR		0	NR	
	SRM 1R-94	10	2	15 X 80	40	1	15 X 38
ELT-5500	ASTM 3039	5	1	15 X 250	20	1	15 X 56
	ASTM 5379	0	NR		0	NR	
	SRM 1R-94	10	1	15 X 80	40	1	15 X 38
CD-550-100	ASTM 3039	5	1	15 X 250	20	1	15 X 56
	ASTM 5379	0	NR		0	NR	
	SRM 1R-94	10	1	15 X 80	20	1	15 X 38
DBM 1708	ASTM 3039	5	3	15 X 250	0	NR	
	ASTM 5379	5	4	20 X 76	20	1	20 X 32
	SRM 1R-94	5	3	15 X 80	20	1	15 X 38
BXMC1708	ASTM 3039	5	3	15 X 250	0	NR	
	ASTM 5379	5	4	20 X 76	20	1	20 X 32
	SRM 1R-94	5	3	15 X 80	20	1	15 X 38

NR = Not Required
A260/LT5500/CD550 will all have two properties measured during SRM1R-94 Test with 5 coupons allocated to each property testing

For each fiberglass type, unique specimen designs were made and coupons were developed. Six (6) coupons, were originally manufactured according to the dimensional specifications required by the corresponding ASTM and SACMA testing standards. One of the six coupons was used to set-up the test equipment. All test coupons were made for laboratory testing according to the ASTM specifications in the documents. The coupons were fabricated by infusion using an epoxy resin. Enough laminates were infused to produce six coupons for each test. Coupons were machined using a computer controlled milling machine and were post cured at Knight a & Carver to achieve maximum strength.

Coupon and tab size and quantities for each test were determined based on the testing specifications and type of material property that was to be tested. Coupon blanks for all five fabrics were infused with Jeffco 1401-21 resin simultaneously using the approach shown in Figure 6.3.

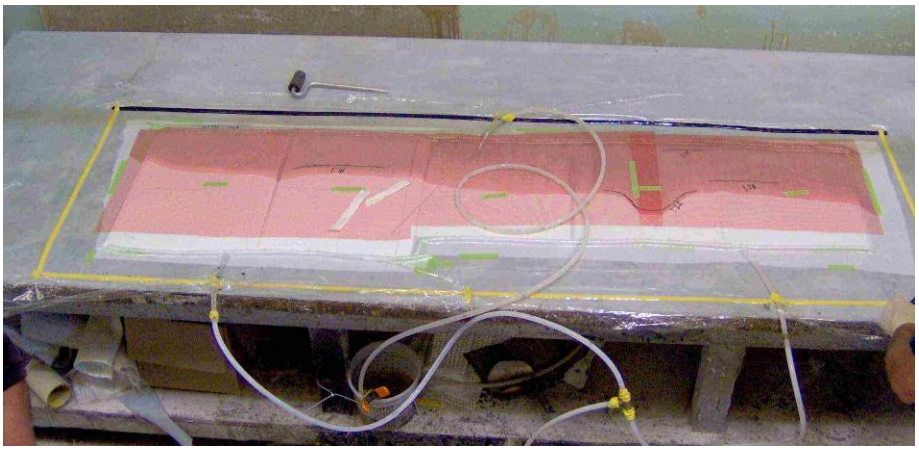

Figure 6.3 Infusion of test coupons.

After tabs were bonded, the blanks were machined with a CNC mill to the exact sizes specified by the test standards as shown in Figure 6.4. After machining, the coupons were inspected, sorted and labeled. All coupons were post cured by increasing the temperature slowly to 150 °F over a period of 10 hours and then maintaining the temperature at 150°F for an additional 12 hours.

Figure 6.4 Example test coupons.

Laminate test results from each coupon were obtained from the testing laboratory. The unidirectional material tests showed some differences between materials, but did not conclusively show one to be the best.

6.1.5 Adhesive Property Testing

ADHESIVE TEST MATERIALS

Testing was conducted to measure the properties of the structural adhesive needed to bond the blade shells and shear webs. Three adhesive types were tested.

PROSET 175/277

Proset adhesive is a pre-formulated epoxy adhesive. It has been proven as a high strength adhesive in past applications. It has a variety of hardeners which allow the gel time to be altered as needed for the temperature at hand. It is the consistency of Vaseline when mixed, but flows under pressure. Cure time was 150 minutes. Its higher cost is a disadvantage.

JEFFCO 1401-21 SA

Jeffco 14-21-SA is a toughened epoxy adhesive formulated with the Jeffco 1401-21 infusion resin. Jeffco formulated this adhesive specifically for the wind blade industry. It is of a consistency that is easy to work with and will not sag. Cure time was 160 minutes.

JEFFCO 1401-21 K & C SPECIAL MIX

Knight and Carver formulated an adhesive using similar components as Jeffco. The same infusion epoxy #1401-21 was used. First, Hycar 32 was added as a toughening agent, then milled fibers and Aerosil were added to thicken and strengthen the adhesive. This mixture was made to form the desired consistency for ease of handling during bonding.

ADHESIVE TEST PREPARATION

Three adhesives were tested to assess suitability for blade shell and shear web bonding as summarized in Table 6.4. Test coupons were prepared for ASTM-D-3165-00 lap shear adhesive testing using 1/8", 1/4" and 3/8" adhesive bond lines. Coupons were fabricated from 1/8" thick fiberglass sheets cut from a pre-made fiberglass panel (Figure 6.5). Square fiberglass pieces (8" x 8") were bonded together using the three test adhesive. Spacers were precisely cut for the three bond line thicknesses. The adhesive was mixed and spread onto one sheet and the second sheet was placed on top, pushing the excess adhesive out the sides. Finally a weight was set on top until partly cured (B-staged). The coupon blanks were then cured at 150° F for 12 hours. The blanks were then machined to ASTM specifications.

Table 6.4 ASTM-D-3165-00 lap shear adhesive test coupon summary.

Adhesive	Part #	Thickness	Quantity of coupons	Size of Coupon	Size of Bond Area
Jeffco wht	1401-21K&C	3/8	5	1"X 7"	.5" x 1"
	1401-21K&C	1/4	5	1"X 7"	.5" x 1"
	1401-21K&C	1/8	5	1"X 7"	.5" x 1"
Jeffco Blk	1401-21-SA	3/8	5	1"X 7"	.5" x 1"
	1401-21-SA	1/4	5	1"X 7"	.5" x 1"
	1401-21-SA	1/8	5	1"X 7"	.5" x 1"
PROSET	175/277	3/8	5	1"X 7"	.5" x 1"
	175/277	1/4	5	1"X 7"	.5" x 1"
	175/277	1/8	5	1"X 7"	.5" x 1"

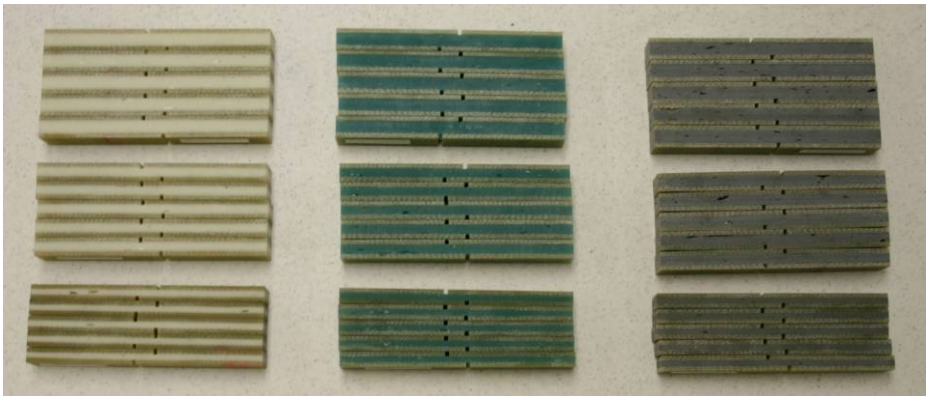

Figure 6.5 Adhesive test coupons.

The adhesive testing effort was superseded by the decision to use the adhesive specified in the Euros 51 design for the STAR blade.

6.2 Prototype Blade Testing

6.2.1 Frequency Test

The first prototype STAR blade was installed in the test stand and its frequency response was measured using an impulsive load (Figure 6.6). Strain gage and accelerometer data were used to calculate the first flatwise and edgewise natural frequencies.

The second laboratory test in the series applied a stepped load to the blade. The first load level simulated an IEC Class III maximum power operating condition, followed by a static proof load. The static proof test provided data for linear and angular deflections, shear and spar cap surface strain, and blade modal frequencies. The measured values were then compared against predictions and used to validate design models.

Two Campbell CR1000 dataloggers were used to store measured data during the test. The CR 1000 can accept up to 8 channels and stores the data to compact flash (CF) cards. Data was sampled at a rate of 20 Hz during the frequency response test and at 2 Hz during the static proof test.

The test data was obtained from an accelerometer and strain gages connected to a pair of Campbell Scientific CR1000 dataloggers. The blade was mounted in the test stand and an impact load was created by releasing a known weight attached near the blade tip. In the flat direction, a 115 pound deadweight was hung by a string from the blade at approximately 75% span. The string was cut to release the weight and introduce the impulse load to the blade. In the edge-wise direction, the blade was attached by a string to a load cell and a hand held winch. The winch was anchored to a vertical beam in the shop near the blade. The string was tensioned and then cut to introduce the impulse load to the blade.

The recorded flat-wise and edge-wise response time series were used for subsequent data processing. The time series was evaluated using a Fast Fourier Transform (FFT) to extract the natural frequencies of the blade.

Figure 6.6 Blade frequency measurement test setup.

The measured flatwise frequency was 1.66 Hz as compared to a predicted value of 1.92 Hz and the measured edgewise frequency was 2.23 Hz as compared to a predicted 2.38 Hz. Table 6.5 provides the predicted values for the STAR 56 meter diameter prototype blade and Figure 6.7 shows the accelerometer response.

Table 6.5 Predicted natural frequencies for the STAR 56 blade.

			RPM =	32.3
	Flatwise	**Edgewise**	**Flatwise**	**Edgewise**
First Frequencies	(Hz)	(Hz)	(p)	(p)
Non-Rotating	1.92	2.38	3.56	4.43
Rotating	2.02	2.46	3.75	4.57
	1.109	1.063	<- Centrifugal Stiffening "k" Ratio	

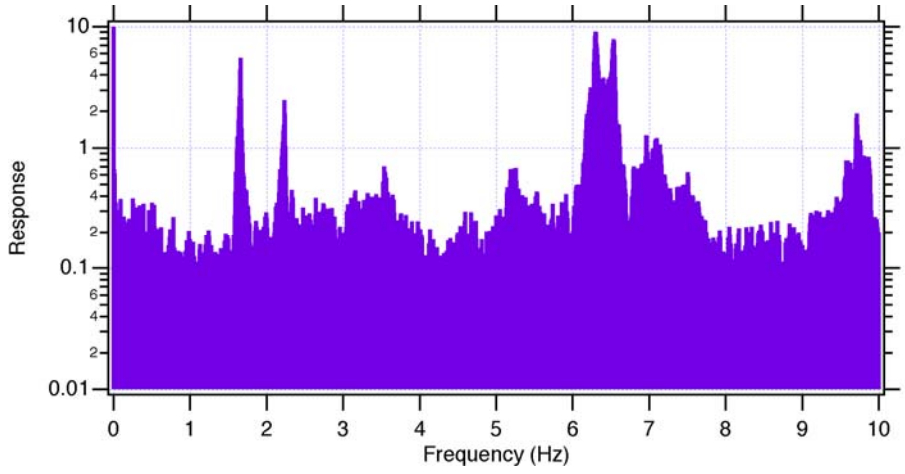

Figure 6.7 Accelerometer frequency response [1.66, 2.23, 3.53, 6.29, 6.53, 9.71 Hz].

6.2.2 Static Twist Measurement Test

Static proof testing was conducted with the STAR prototype blade mounted as shown in Figure 6.8. The test stand had been used previously for testing blades in the 25 meter size range and had the proper mounting dimensions for the STAR blade. The test instrumentation system included 15 data channels and four manually recorded displacements, which are summarized in Table 6.6.

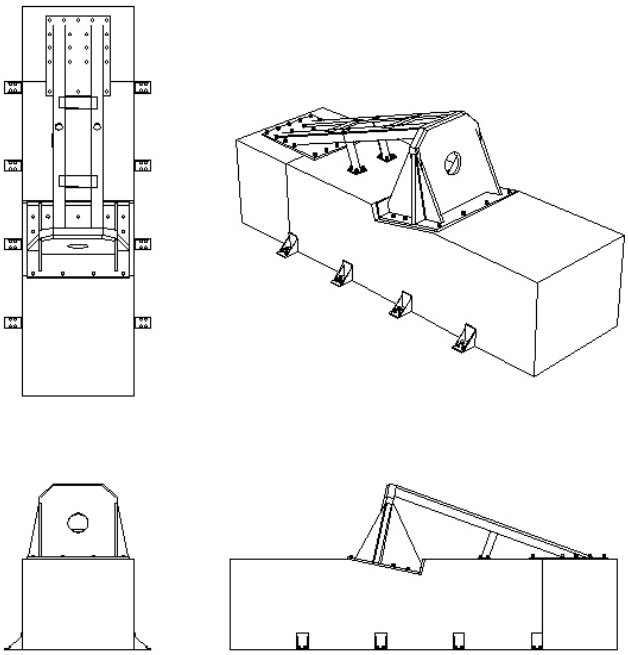

Figure 6.8 Diagram of the Knight & Carver blade test stand.

Table 6.6 Laboratory test sensor list.

Channel Number	Channel Name	Channel Description	Sensor Configuration
1	50_AFT	50% Span Aft Bay Shear	Full Shear Bridge
2	70_AFT	70% Span Aft Bay Shear	Full Shear Bridge
3	90_AFT	90% Span Aft Bay Shear	Full Shear Bridge
4	50_STRAIN	50% Spar Cap Strain	1/4 Bridge
5	70_STRAIN	70% Spar Cap Surface Strain	1/4 Bridge
6	90_STRAIN	90% Spar Cap Surface Strain	1/4 Bridge
7	50_TWIST	50% Span Twist Angle (Degrees)	Inclinomometer
8	70_TWIST	70% Span Twist Angle (Degrees)	Inclinomometer
9	90_TWIST	90% Span Twist Angele (Degrees)	Inclinomometer
10	L_ANGLE	Leading Angle Spar Shear	Full Shear Bridge
11	TR_ANGLE	Trailing Angle Spar Shear	Full Shear Bridge
12	L_DOUBLE	Leading Double Spar Shear	Full Shear Bridge
13	TR_DOUBLE	Trailing Double Spar Shear	Full Shear Bridge
14	TR_SINGLE	Trailing Single Spar Shear	Full Shear Bridge
15	EDGE_ACC	Edgewise Tip Acceleration	+/- 2G VC Accelerometer
16	n/c	n/c	n/c
17*	DEF_50	Deflection 50% Span	Tape Measure
18*	DEF_70	Deflection 70% Span	Tape Measure
19*	DEF_90	Deflection 90% Span	Tape Measure
20*	DEF_100	Deflection 100% Span	Tape Measure

A fiberglass tape measure was laid out span-wise over the center of the high pressure side spar cap to mark the gage and tilt measurement locations. The proof test measurements included spar cap surface strain at 50%, 70%, and 90% of rotor span as shown in Figures 6.9 and 6.10. Strain gages were bonded in a full-bridge shear configuration to the shear web flanges at different locations of the spar joint prior to final assembly. Shear strains on the high pressure side blade skin were measured in the aft panels at 50%, 70%, and 90% span. Blade deflection was measured relative to the floor using custom measuring tapes at approximately 50%, 70%, 90%, and 100% span. The twist angle was measured using high accuracy inclinometers mounted at 50%, 70%, and 90% span.

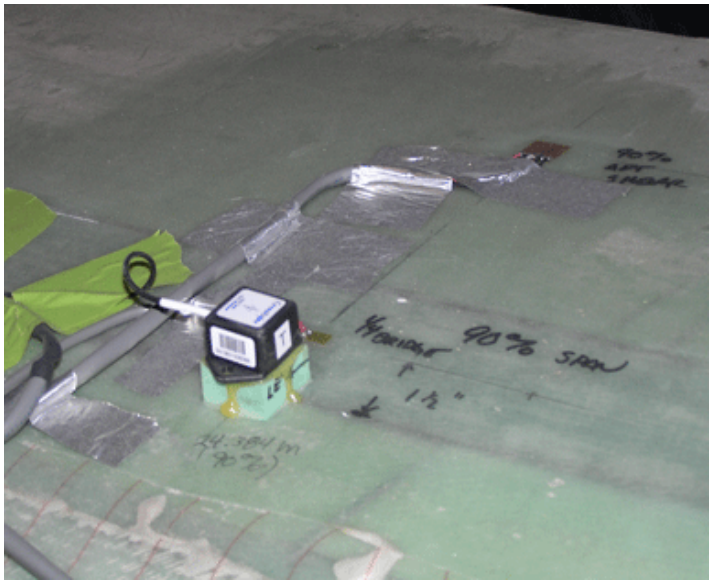

Figure 6.9 90% span location sensor placement with quarter bridge bending gage and tilt sensor.

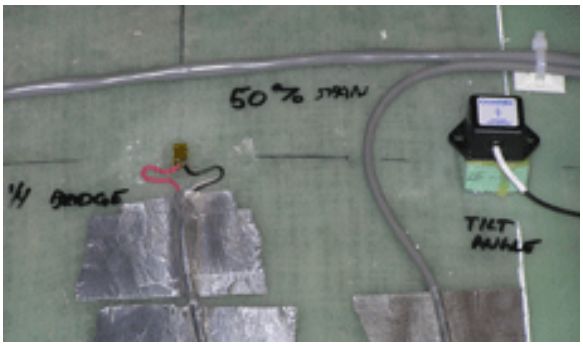

Figure 6.10 50% span location sensor placement with quarter bridge bending gage and tilt sensor.

The test load was applied by hanging 55 gallon drums (barrels) from the blade surface along the spar cap axis (Figures 6.11 and 6.12). The applied test loads closely followed the loading used in the finite element model (Figure 6.13). The loads were applied successively at 50% operating load, 100% operating load, and IEC Class III extreme wind load for the outer portion of the blade. The individual water barrels were attached to the blade surface using steel hangars bonded to the blade surface on 750 mm (3/4 meter) intervals. This spacing

coincides with the input loads applied to the finite element model of the blade. A safety strap attached to the overhead crane was used to support the blade when weights were being mounted.

Figure 6.11 Filling barrels with water.

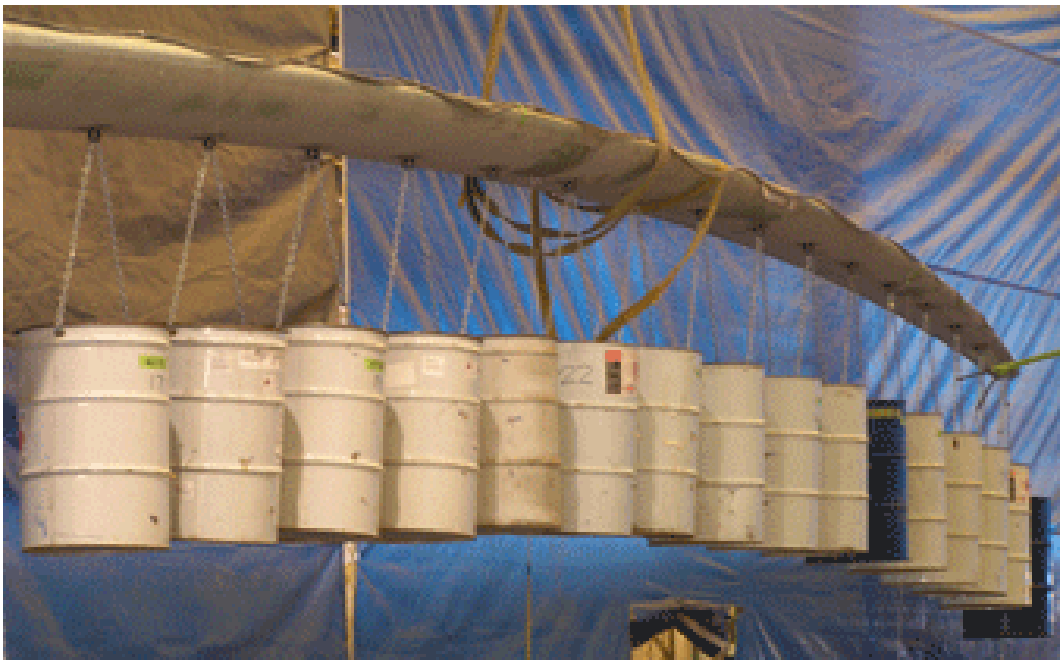

Figure 6.12 Blade loaded with water barrels.

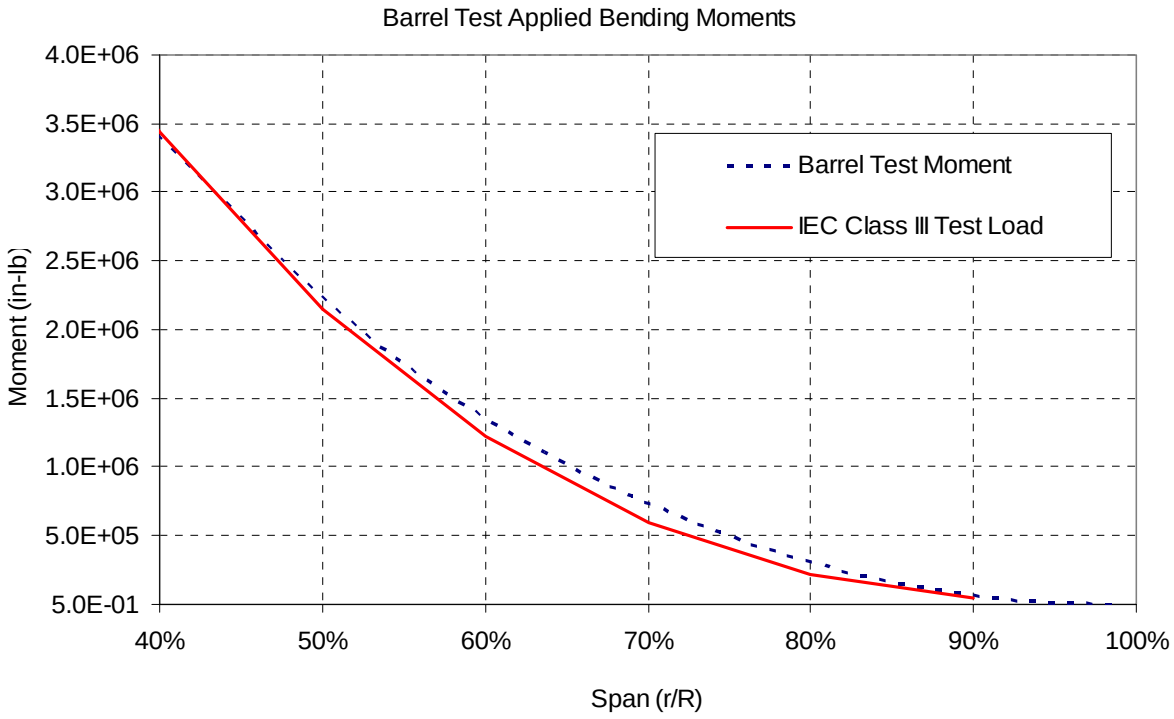

Figure 6.13 Barrel test moment as compared to IEC test requirements.

SPAR CAP SURFACE STRAIN GAGE INSTALLATION

Blade bending creates tension and compression in the span-wise direction. The spar cap surface strain measurements used 1000 Ω strain gages mounted in a single active element 1/4-bridge configuration as shown in Figure 6.14.

The gages were installed on the chord-wise center of the spar cap at the 50%, 70% and 90% span measurement stations. They were aligned with a raised line on the blade surface that indicated the center of the spar. This line was a result of a line scribed in the blade mold. It was created to locate the center of the spar during blade construction.

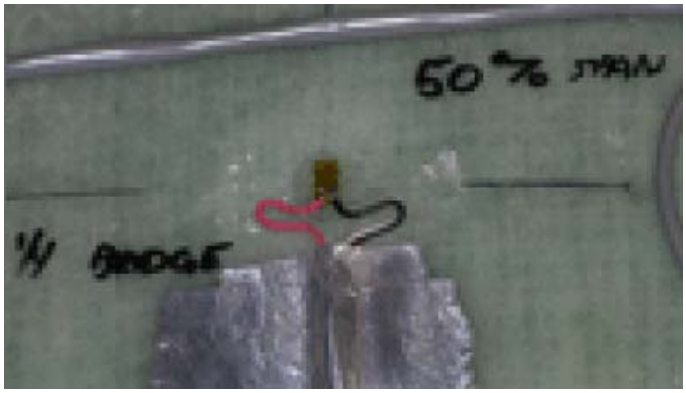

Figure 6.14 Quarter bending bridge configuration at 50% span.

SHEAR GAGE INSTALLATION

Shear in the blade skins was measured at 50%, 70% and 90% span using special purpose 350 Ω shear pattern strain gages. The difference in normal strain sensed by any two arbitrarily oriented strain gages in a uniform strain field is proportional to the shear strain along an axis bisecting the strain gage axes, irrespective of the included angle between the gages. When the two gages are 90 degrees apart the shear strain along the bisector is numerically equal to the difference in normal strains. A full shear-bridge composed of four gages was used, as shown in Figure 6.15.

A line perpendicular to the spar at the measurement location was laid out in a chord wise direction to place the shear gages. The gages were then installed half way between the centerline of the spar cap and the trailing edge of the blade.

Figure 6.15 Full shear bridge configuration.

DEFLECTION MEASUREMENT

Deflection measurements were recorded manually and with video near 50%, 70%, 90%, and 100% span using custom engineering measuring tapes. The stations were chosen to lie about halfway between barrels so there would be no interference between the hanging barrels and the measuring tapes. This resulted in nominal spanwise locations of 12.875m (47.36%), 18.875m (69.43%), 24.125m (88.75%), and 27.184m (100%). Figure 6.16 shows the 89% measuring tape.

The barrel testing provided data necessary for comparison with the computed tip displacement. After correcting the measurements for the geometry of the experimental set-up, the predicted value for tip deflection was compared to the measured value with good results.

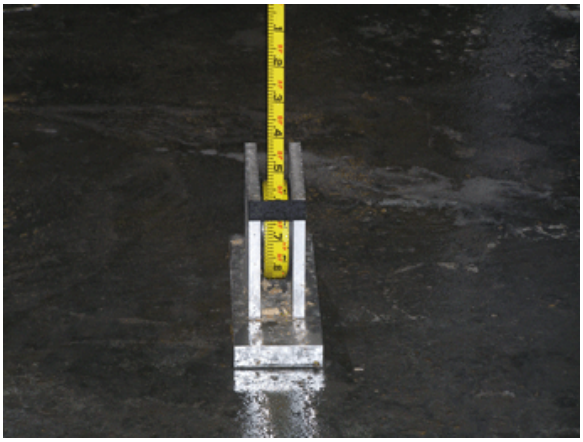

Figure 6.16 Illustration of the blade deflection measurement device.

TWIST MEASUREMENT

Blade twist during the static test was measured using three Crossbow CXTLA01 tilt sensors located at 50%, 70%, and 90% span (Figure 6.17). The CXTLA single- and dual-axis analog tilt sensors offer high-resolution, accuracy, and fast response. The CXTLA series design centers around a highly stable silicon micro-machined capacitive inclination sensor element. The CXTLA series is fully signal conditioned with high level analog output. The CXTLA Series Tilt Sensors use a micro-machined acceleration sensing element with a DC response to measure inclination relative to gravity. The response of the tilt sensor depends on the magnitude of gravity parallel to the sensor element.

Specifications	CXTLA01
Performance	
Angular Range (°)	± 20
Angular Resolution (° rms)	0.03
Sensitivity - small angles (mV/°)	100 ± 10
Sensitivity Drift (%/°C)	0.01
Zero Angle Voltage (Volts)	2.5 ± 0.15

Figure 6.17 Specifications for the blade twist measurement sensor.

Blade twist response is a key to its load shedding ability near and above rated windspeed. Both the 90% inclinometer and tip accelerometer should see similar amounts of loading induced twist according to the design calculations. It is the twist as seen by the incoming airflow that determines how much load the outer blade will shed via reduction of angle of attack and reduction in airfoil lift coefficient. It is therefore twist measured relative to a radius vector to rotor centerline which is relevant in determining aerodynamic unloading.

The inclinometers and tip accelerometer were aligned to the blade geometric axis, as were the strain gauges. As a result of not being directly along the blade elastic axis, the measured

values included angular changes due to blade bending in addition to those derived from blade twist. This bending component reduces the measured twist increment and a correction was needed to determine the aerodynamically active twist component. Results obtained from the barrel test were successfully used to confirm calculated design values. The key result of the twist testing was to confirm that the blade twisted enough to shed load; a crucial finding to have in hand before moving into field testing.

6.3 Fatigue Testing

6.3.1 Test Article

The blade selected for the NREL fatigue test was the first STAR blade produced in Knight & Carver's Howard, South Dakota factory. In large part, the logic for this was that if startup defects might be present, these were better assessed on the test stand, than flown on the field test turbine. This blade was built in October of 2007 and shipped to NREL in January of 2008.

6.3.2 Resonance Test Method

The fatigue test was done with the blade loaded in a primarily flatwise direction, so that both flatwise bending and the adaptive torsional twisting could be simultaneously tested. The first phase of testing was designed to test the outboard portion of the blade where the adaptive twist response is greatest. Figure 6.18 shows the blade in the test stand, with the primary loading and load trimming saddles in position. Loads were introduced by a pair of saddles centered on the 11m station, and the load distribution was adjusted via two additional saddles at the 18m & 23m stations, which were weighted to achieve the desired load profile (see Figure 6.19). This choice placed the loading saddles away from the 12 m – 13 m region where inner skin crazing had been noted in the earlier static test performed at Knight & Carver, and the region near 15 m where peak torsional shears were expected to occur.

Figure 6.18 STAR prototype blade in NREL test stand with loading saddles.

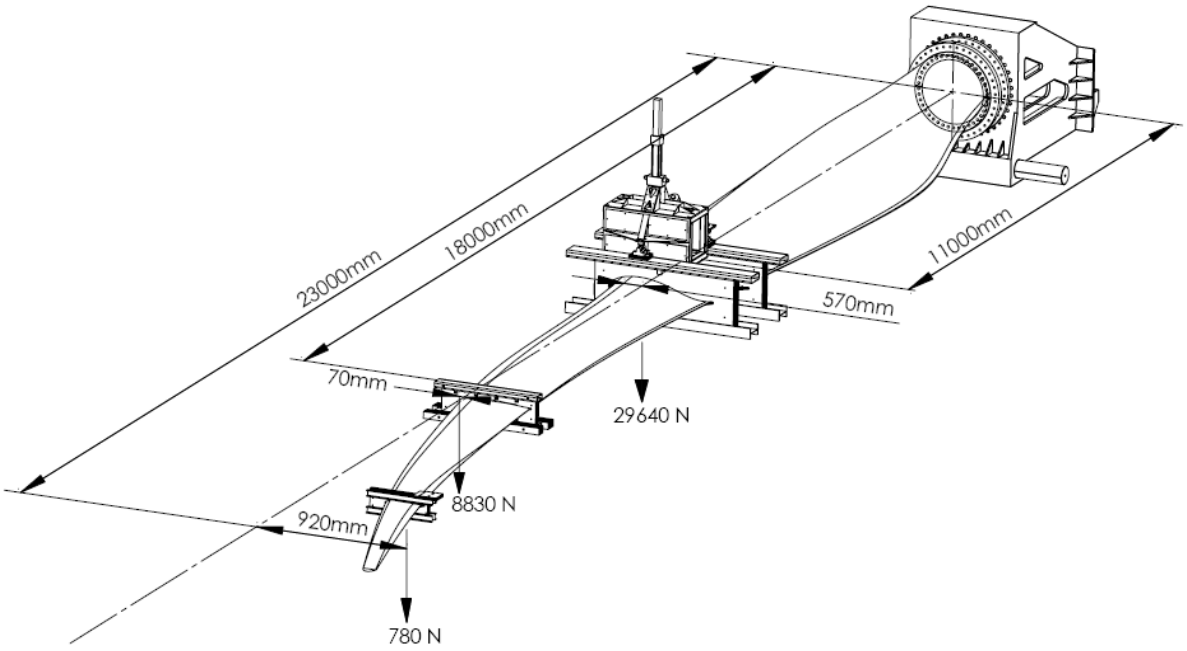

Figure 6.19 Diagram showing the fatigue test stand dimensions and saddle loads.

6.3.3 Outboard Blade Testing

The magnitude of the loads was selected to provide at least an equivalent full 20 year fatigue life in one million actual cycles, for the blade outboard of the 13 m station. The testing started on September 4, 2008 with a calibration pull, and cycling began the next day to begin dialing in the resonant system. Full load testing was underway in October, and some deformation of the LP panel near the max chord location was noted, but was judged to be no cause for undue concern. This proved to be correct, as this panel flex caused no problems during test, which proceeded without incident until 180K full load cycles, when an 11 cm trailing edge separation was noted at the 14.2 m station. After primary review by NREL staff, and full concurrence by the K&C test support team, it was determined that the test could proceed with periodic separation length monitoring. This proved to be a good decision, as the test continued into mid November to the full one million cycle target without difficulty from either of these cited conditions.

6.3.4 Inboard Blade Testing

After the first loading sequence, which tested the blade outboard of the 13 m station to at least a full 20 yr equivalent life, attention shifted to increasing the inner blade loading so that region of the blade could be more thoroughly tested. Cycling resumed and by mid-December a full 20 year lifetime equivalent damage load was achieved for all blade stations outboard of 5m. Strain and stiffness data was essentially unchanged since the test began, but increasing acoustic emissions in the 16m – 18m region indicated that something was beginning to happen. At this point the test had reached its objectives without an obvious failure that would force stopping, but the SNL/NREL/K&C consensus was to press further if more could be

learned. It was decided to increase the loads in 10% increments for 100K cycle blocks to see if a definitive failure could be achieved.

In order to better understand the source of the 16m – 18m acoustic emissions, Darren Rahn of NREL devised a way to get both still photos of the blade interior, and full action video under moderate load cycling. This latter in particular revealed considerable motion and what appeared to be a crack in the aft face of the shear web in the region generating acoustic emissions. Upon further examination and discussion, it was determined that during the first blade fabrication a shear web height adjustment had been made (which included reinforcing material to strengthen the modified area), which had also generated a stress concentration that may have helped initiate the shear web crack. In a collaborative effort that involved NREL, K&C, and Sandia, it was ultimately determined to attempt a novel repair of the shear web, so that higher loads that might uncover another blade weakness could be employed. K&C performed this work by splitting open the trailing edge, and working through the opening to bond additional double bias reinforcing to the back of the web, then rebonding the trailing edge, so no holes were cut in the blade shell structure in performing the reinforcing work.

After a delay attempting to commission upgraded hydraulic controls, the increasing load test sequence began in late January 2009, and proceeded through the 100K block at 130% of baseline load. Due to video observations of web buckling, the test team decided not to elevate the loads beyond 130%, but instead continued to 280K cycles at the 130% load level. Only minor acoustic emissions had been observed in the 5m-6m region, while the region near 18m was becoming quite active again. It was clear the web would again be the limit to further testing, before another failure mechanism could become apparent.

The test was then stopped at this point, with 2,660K cycles, and much of the blade having been exercised to about three times the target 20 year equivalent life.

6.4 Field Testing

6.4.1 Field Test Summary

OBJECTIVE AND APPROACH

- The primary goal of the field testing was to measure the blade loads for the STAR rotor and compare them to the representative loads for the turbine.

- A secondary goal was to compare the performance of the STAR rotor to reference turbines operating under similar conditions.

The field test turbine was a Zond 750 (Z48) turbine whose blades had been destroyed by lightning. This turbine operates with a rated speed of 34.4 rpm and originally had a 48 meter rotor. The STAR field testing used a two channel sensor system, which has proven to be successful on prior projects. Strain gages were used to measure blade root bending moments on a Zond Z48 turbine equipped with the STAR prototype blades using a 54 meter diameter rotor. The team had previously used a similar test approach to measure data on Zond 750 kW turbines with conventional blades at two sites in Iowa and Minnesota. The STAR data sets

are identical in type to those earlier measurement records, which acted as load references. This approach provided a broad comparison of actual operating loads between the STAR rotor and other Z750 turbines in a range of configurations and environments.

TEST SITE DESCRIPTION

The test site was located in the Tehachapi Mountain wind resource area of California. The test turbine is located within an existing wind plant several miles southeast of the town of Tehachapi, California (Figure 6.20). The elevation of the test site is approximately 4920 feet and the hub height is slightly more than 5000 feet above sea level. Wind conditions at the site are within the IEC Class II designation.

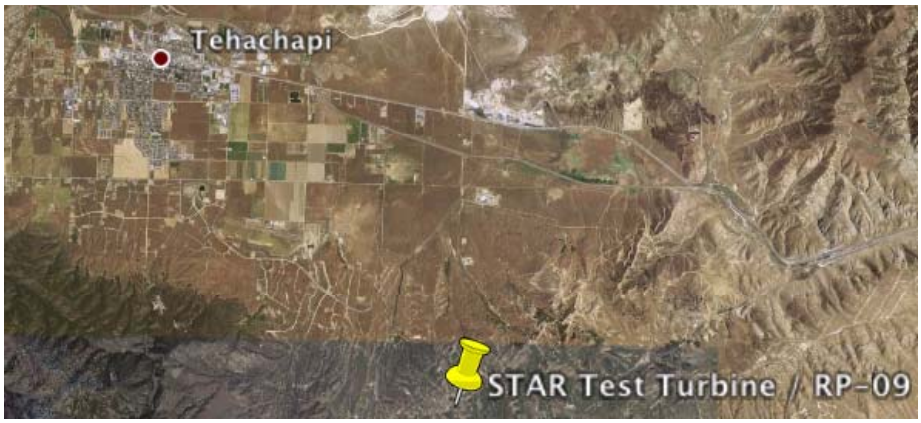

Figure 6.20 General location map showing the STAR rotor test site.

SCADA performance data were recorded for several Zond Z48 turbines, designated as RP-01, RP-02, RP-04, RP-05, RP-06, RP-07, RP-08, and RP-09. The position of Zond 750 turbines that provided measurements for the STAR rotor testing are mapped according to Figure 6.21. The STAR rotor was installed on turbine RP-09, which is the turbine farthest to the south in the grouping.

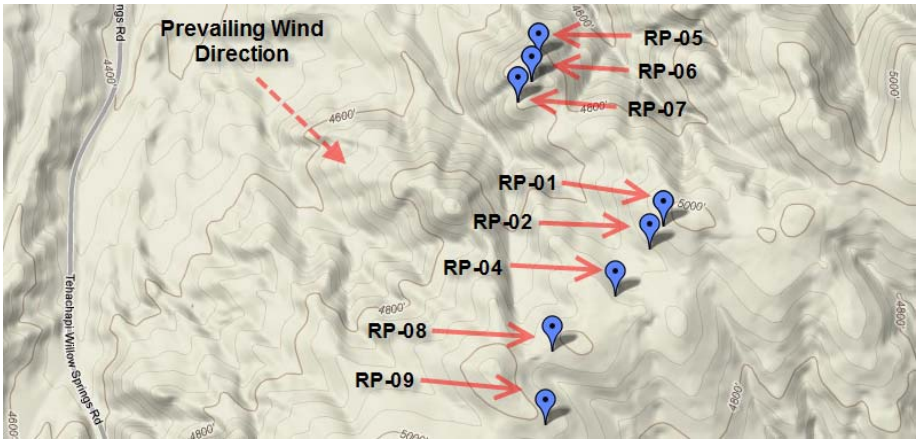

Figure 6.21 Map of test site showing turbine identification with the STAR rotor on turbine RP-09.

The STAR test turbine was located in a region of complex terrain and had numerous turbines of various types and sizes operating nearby, as shown in Figures 6.22 and 6.23. The prevailing winds come from the west and several rows of turbines are installed upwind of the test machine.

Figure 6.22 View of the STAR test site looking north.

Figure 6.23 View of the STAR rotor on turbine RP-09 test site taken from Oak Creek Road looking west.

ROTOR INSTALLATION

The STAR test rotor was installed on 15 February 2008 on turbine RP-09 (Figure 6.24). The rotor was inspected and minor repairs were performed prior to testing. Installation of the blade load instrumentation system and final checkout of the turbine was completed in March of 2008.

Figure 6.24 STAR rotor during installation and inspection on the RP-09 test turbine in Tehachapi.

6.4.2 Field test Data Collection

TEN MINUTE TURBINE AND METEOROLOGICAL DATA

Turbine power, turbine nacelle wind speed, blade pitch position, generator speed, and rotor speed were obtained from the site SCADA (Supervisory Control And Data Acquisition) records. This data was collected by the existing site SCADA hardware and provided as ten (10) minute average values (Table 6.7). SCADA data were available for the STAR prototype test turbine and for seven (7) baseline Z48 turbines operating at the same location.

Table 6.7 SCADA data file format for the STAR and baseline turbines.

Date	YYYY/MM/DD
Time	HH:MM:SS
Nacelle Wind Speed	ft/s
Generator Power	kW
Pitch Angle	deg
Gen Speed	rpm
Hub Speed	rpm

LOAD DATA ACQUISITION SYSTEM

The test effort was organized to gather data using three separate data acquisition systems, each mounted near the measurement location. Each DAS used a Campbell Scientific CR1000 Data Acquisition System (DAS) as shown in Figure 6.25. This compact, rugged system has proven to be effective for harsh field measurement situations such as those encountered in a wind turbine rotor.

Figure 6.25 Photograph of the Campbell Scientific CR1000 data acquisition system.

At the start of testing the turbine had one high speed (50 Hz) data acquisition system operating in the hub to record blade root bending moments. DAS #1 was mounted inside the blade root as shown in Figures 6.26 and 6.27. A 7.5 amp-hour gel-cell battery provided power to the system for about ten days of continuous data collection. The CR1000 , radio telemetry equipment, battery, and other equipment were installed in an industrial junction box.

DAS #1 BLADE ROOT BENDING MOMENT

- Blade root edgewise bending (kNm) strain gage bridge
- Blade root flatwise bending (kNm) strain gage bridge
- 50 Hz sampling frequency
- Online in late February 2008

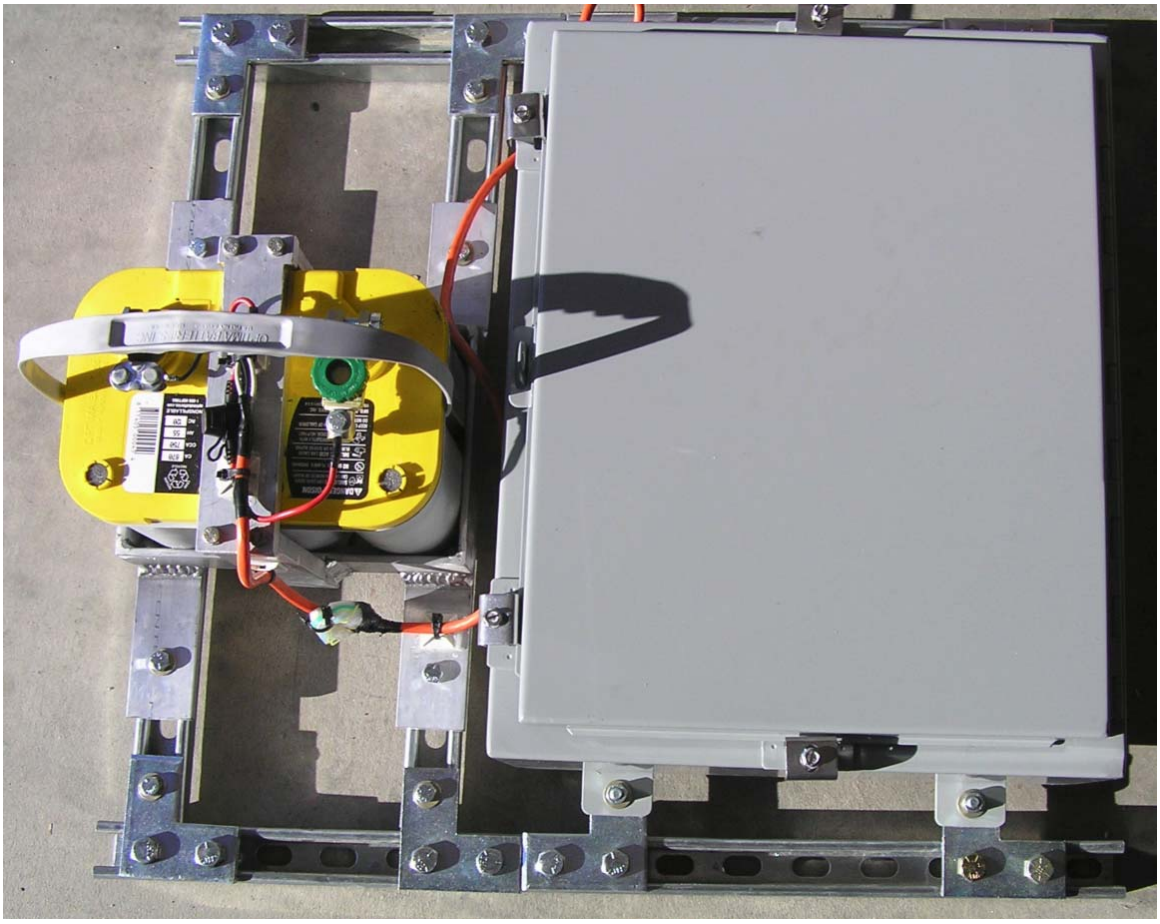

Figure 6.26 Rotor instrumentation box with battery power supply.

The DAS measures the voltage output from each bending bridge at a 50 Hz sample rate. Excitation was set to the system maximum of 2500 mV. No filtering was used on strain gage measurements. A reversed polarity differential measurement scheme was used for the strain gage channels to increase system accuracy and increase common-mode noise rejection. Data is stored on a 2 GB compact flash card. The memory card was large enough to continuously store data for several weeks.

Figure 6.27 Rotor instrumentation box mounted inside the blade root.

Two (2) sets of strain gages were installed on one blade root to provide flatwise and edgewise bending moments. The gages were installed using four (4) active elements in a full bending bridge configuration (Figures 6.28 and 6.29).

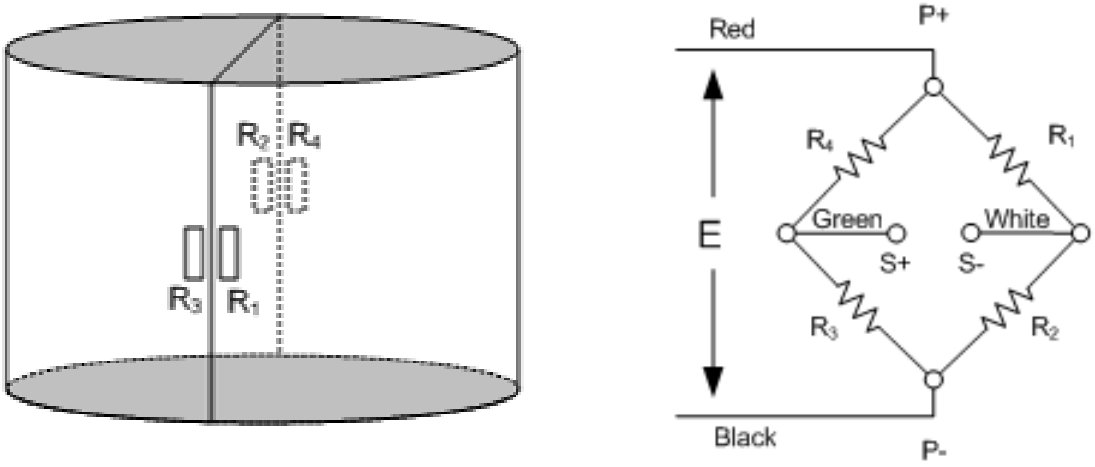

Figure 6.28 Illustration of strain gage placement and Wheatstone bridge.

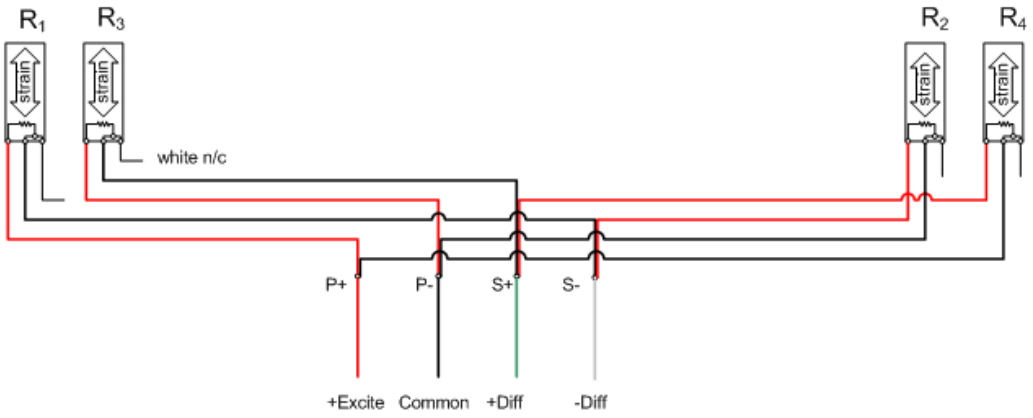

Figure 6.29 Diagram of the strain gage wiring for a single channel.

The strain gage leads were routed into the logger box and connected to the CR1000 wiring panel (Figure 6.30).

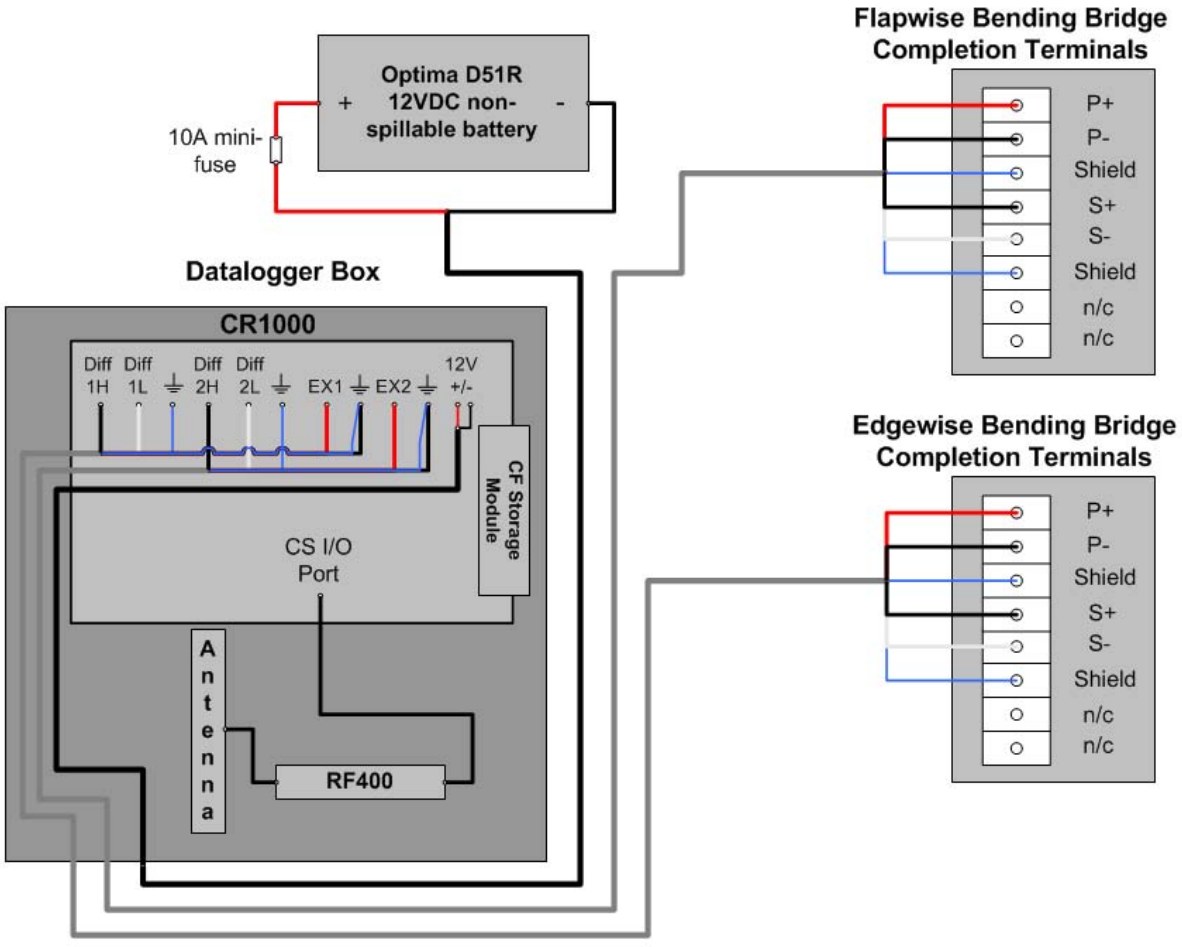

Figure 6.30 Wiring schematic for DAS #1.

A second data logger was installed at the tower base to record power at high speed (50 Hz) in early April 2008. These data allowed evaluation of drive train transient loading and frequency response.

DAS #2 – POWER OUTPUT

- Power Output (kW)
- 50 Hz sampling frequency
- Online in early April 2008

In late May 2008 a third logger was installed in the nacelle to collect low speed (2 Hz) data for wind speed, yaw error, and pitch angle.

DAS #3 – NACELLE

- Nacelle wind speed (m/s)
- Nacelle yaw error (deg)
- Blade pitch angle (deg)
- 2 Hz sampling frequency
- Online in late May 2008

SYSTEM FREQUENCY EVALUATION

The static test prototype (first blade fabricated) was designed to match the Z50 variant of the Zond 750, which rotates at 32.3 rpm. The fatigue test prototype (one blade) and the field test rotor (three blades) were modified to provide a smaller diameter (54 m instead of 56 m), which was necessary to match the Z48 variant of the Zond 750 found at the Tehachapi test site. The Z48 field test turbine operated at a rotor speed of 34.4 rpm.

The natural frequencies of the STAR 54 meter diameter rotor were calculated during the design phase. The calculations showed that both the edgewise and flatwise modes were well located between harmonics as shown in Table 6.8. The design flatwise mode lies between 3.45p and 3.65p and the edgewise is between 4.24p and 4.39p.

Table 6.8 Estimated natural frequencies of the STAR 54 blade.

			RPM =	34.4
	Flatwise	**Edgewise**	**Flatwise**	**Edgewise**
First Frequencies	(Hz)	(Hz)	(p)	(p)
Non-Rotating	1.98	2.43	3.45	4.24
Rotating	2.09	2.52	3.65	4.39
	1.119	1.069	<- Centrifugal Stiffening "k" Ratio	
	updated 7/31/07	for 48m Z750 turbine		

Field test data were collected using natural wind excitation with the turbine not operating. These data were used to determine the natural frequencies of the STAR blade when installed on the test turbine. There were forty-nine (49) hours of data collected with the STAR blades

installed, but the turbine was not operating. The blades were pitched 90° to full-feather during this period. There was some pinwheeling of the rotor in a few of the records.

The time series data were processed using a Fast Fourier Transform (FFT) algorithm to determine the frequency response. The frequency response data for two representative records are presented in Figures 6.31 through 6.33 and are summarized in Table 6.9.

Table 6.9 Measured system modal frequencies from the STAR-2008-0227-1400 data record.

Mode	Flatwise	Edgewise
First tower	0.69 Hz	0.71 Hz
Not identified	1.06 Hz	
Not Identified	1.31 Hz	1.32 Hz
Not Identified	1.74 Hz	
Blade Flatwise	1.83 Hz	1.80 Hz
Blade Edgewise	2.6 Hz	2.63 Hz
Not Identified	3.7 Hz	
Not Identified	4.2 Hz	

The non-rotating frequency of the first blade flatwise mode (1.83 Hz) was slightly lower than the predicted value (1.98 Hz), while the measured blade edgewise frequency (2.6 Hz) was somewhat higher than the calculated value (2.43 Hz). The measured system natural frequencies were well placed between operating harmonics and dynamic amplification through resonance was ruled out as a concern prior to operation of the turbine.

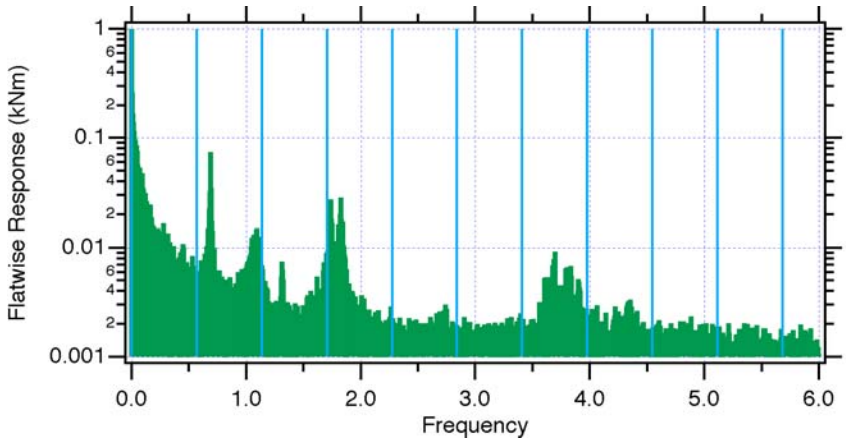

Figure 6.31 Flatwise frequency response for the STAR-2008-0227-1400 data record.

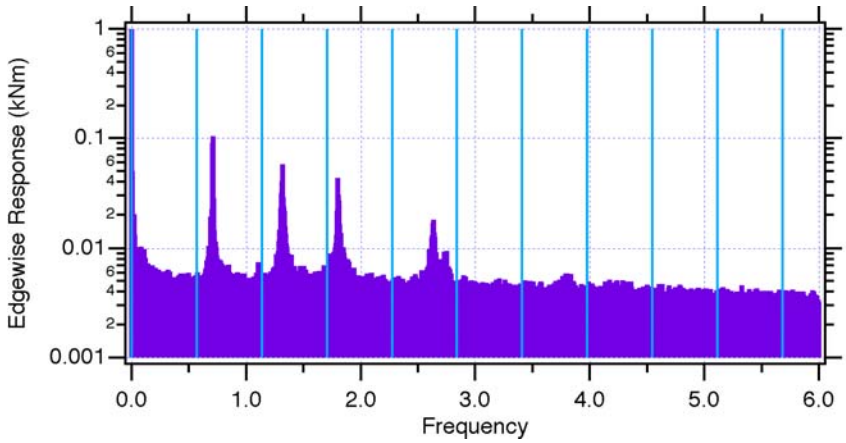

Figure 6.32 Edgewise frequency response for the STAR-2008-0227-1400 data record.

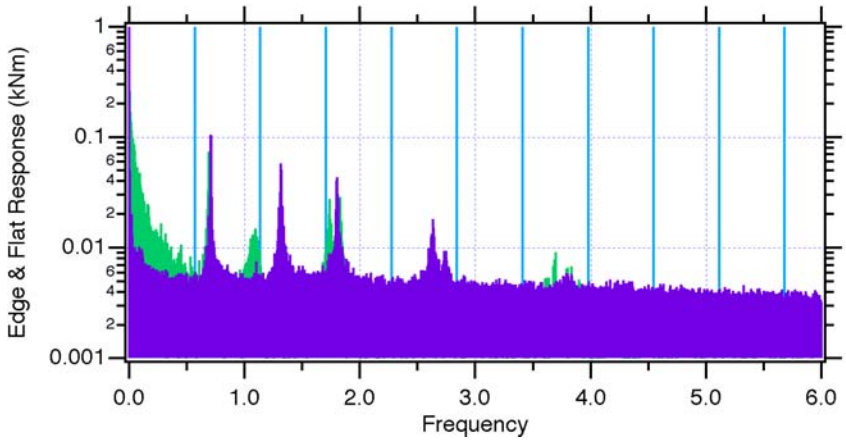

Figure 6.33 Combined edge and flat frequency response for the STAR-2008-0227-1400 data record.

TEST START-UP PROCEDURE

The test turbine began operating at a reduced operating speed in late March 2008. The turbine operated for several weeks at reduced speed, while the operating loads were reviewed. Full-power testing began during the first week of April 2008. During this period the turbine was operated in the normal, full-speed condition when attended by test staff and in the reduced speed condition at night and on weekends. After reviewing the full-speed blade test data, the turbine was released for normal, unattended operation in mid-April 2008.

OPERATING LOAD EVALUATION

The power output and blade root bending moments were evaluated during the test start-up in April 2008. The maximum power output from the turbine during the test period was maintained at at or below the design value of 750 kW, as shown in Figure 6.34. This scatter plot shows 1128 data points that represent values obtained from 10 minute records.

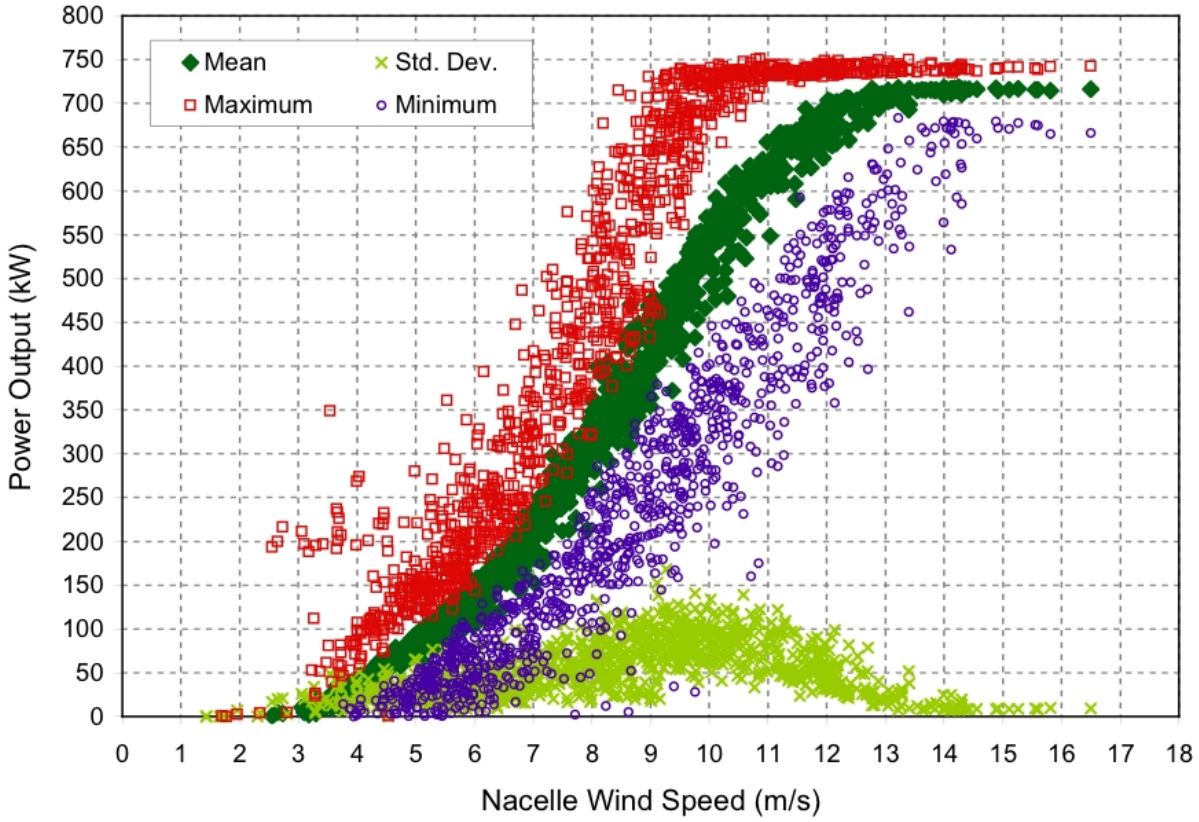

Figure 6.34 Scatter plot of STAR 54 average power data as measured by DAS 2.

The blade flatwise moment was compared to the design loads used to certify the turbine on a regular basis throughout the test period as shown in Figure 6.35, which presents rank ordered data for maximum flatwise bending moment. These data show that the STAR rotor operated safely below the design maximum operating load for the Z750 turbine.

Comparisons between measured loads for the STAR 54 rotor and a baseline Zond 48 rotor are presented in Figures 6.36 and 6.37. A conventional 54 meter diameter rotor would increase blade root bending moment by 80% as compared to the baseline. These results show that measured blade root bending moments for the STAR 54 rotor are comparable to loads measured on the baseline Z48 and no significant increase in loading occurred. The STAR rotor is operating in the field as expected and is successfully shedding high blade root bending loads through dynamically adaptive twisting.

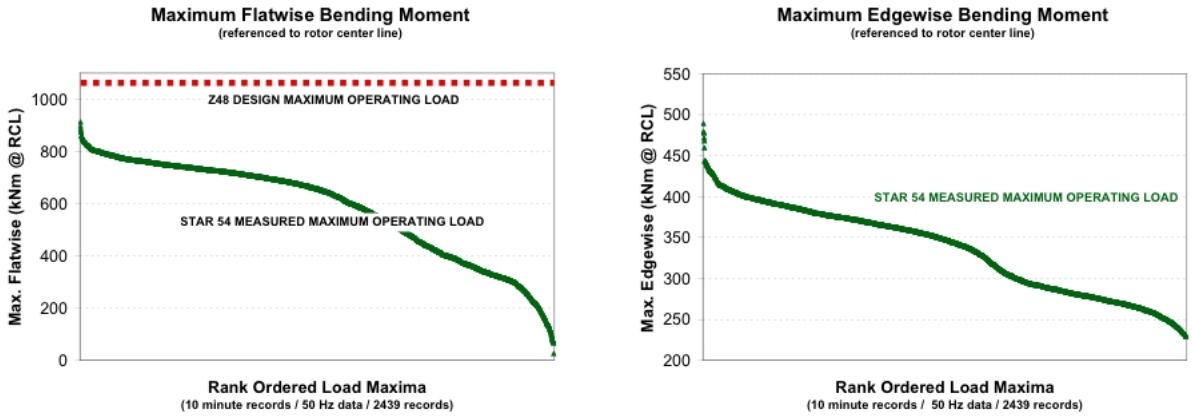

Figure 6.35 Rank ordered STAR 54 root bending moment maxima compared to the Z48 design load.

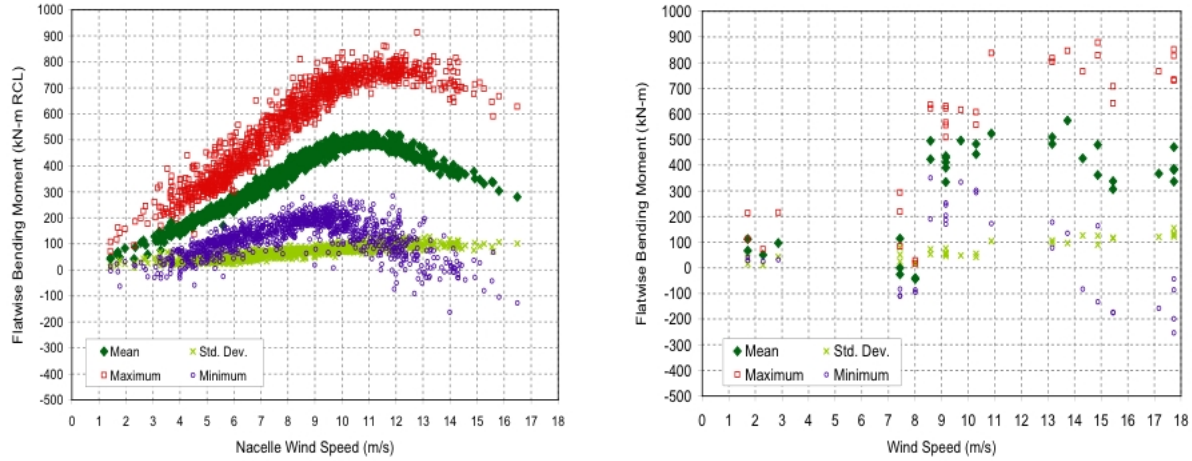

Figure 6.36 Measured STAR 54 flatwise bending moments (left) compared to baseline Z48 loads (right).

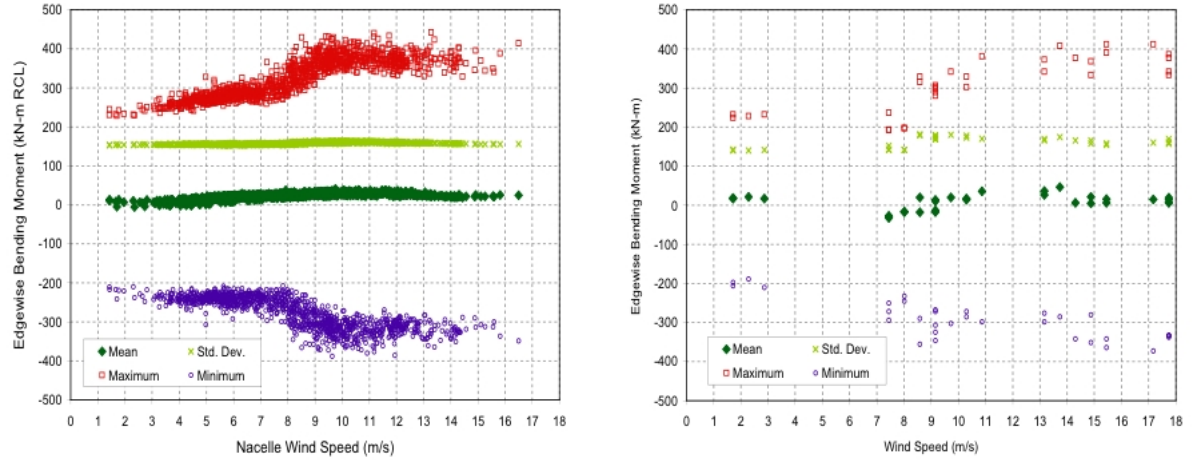

Figure 6.37 Measured STAR 54 edgewise bending moments (left) compared to baseline Z48 loads (right).

6.4.3 Performance Evaluation

JUNE POWER CURVE COMPARISON

Performance measurements were analyzed over a thirty day period from 1 June to 30 June 2008. This period for this data set was selected because the STAR 54 rotor had been operating for an extended period of time and soiling of the blade surfaces would be expected to have occurred. In addition, the month of June is usually a peak production period, when power prices are at the highest rates.

There were strong winds at the site during the month and substantial online performance measurements were obtained over a wide range of operating conditions. The SCADA system recorded the wind speed at discrete values and the data bins (approximately 0.5 m/s in width) were set to match those values. The distribution of wind speeds measured at the STAR nacelle anemometer during the month of June 2008 is shown in Figure 6.38. This data set had a particularly long period of time with wind speeds in the mid-range from 6 to 12 m/s.

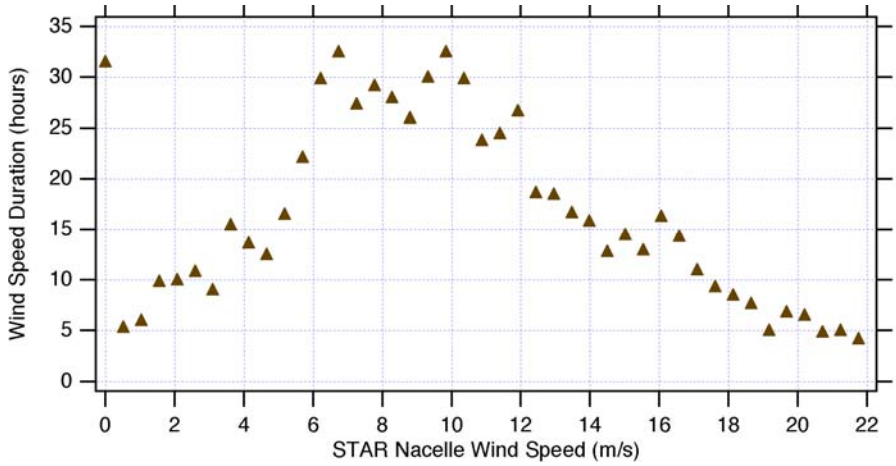

Figure 6.38 STAR binned nacelle measured wind speed during the month of June 2008.

The SCADA data was filtered to remove records when the turbine was not operating so the power curve represents performance during periods when the turbine was producing net power. Figure 6.39 presents a plot of binned online power curves for the STAR 54 rotor, using the test turbine nacelle anemometer for reference.

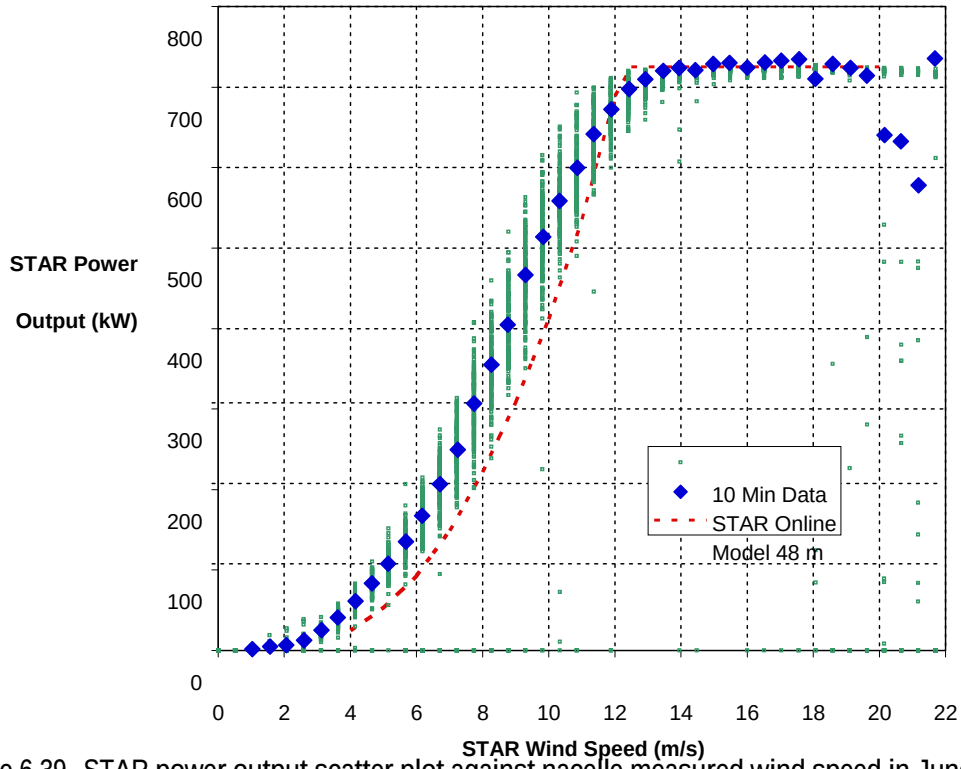

Figure 6.39 STAR power output scatter plot against nacelle measured wind speed in June.

Power curves were prepared for each of the six (6) standard Zond 48 turbines operating at the site. Four of the turbines (RP-01, RP-02, RP-04, RP-08) were located on the ridgeline and have similar behavior to the STAR 54 prototype turbine. These four turbines represented the most productive of the baseline turbines operating at the site and were designated as Group 1. Wind speed data from RP-02 were not considered reliable, so the power curves for that turbine were generated using the RP-04 nacelle wind speed for reference. The other three turbines (RP-05, RP-06, and RP-07) were located at a lower elevation upwind from the main ridgeline and were designated as Group 2. These turbines have a lower energy capture as compared to the first grouping and appear to have lower average wind speed and turbulence.

Lower turbulence levels found at Group 2 turbine site resulted in power curves that had less scatter and were better for comparing with model predictions. Another set of power curves was generated by selecting the best performance from any turbine in the group for each wind bin, as shown in Figure 6.40. This data showed that Group 2 was well matched to the performance model for the 48 meter rotor. Data for the STAR 54 rotor are somewhat less well correlated to the model than Group 2 as a result of the relatively high wind speed and turbulence of the STAR 54 test turbine site. Figure 6.41 compares STAR 54 and the best of the low turbulence (Group 2) turbines to the models, showing good results.

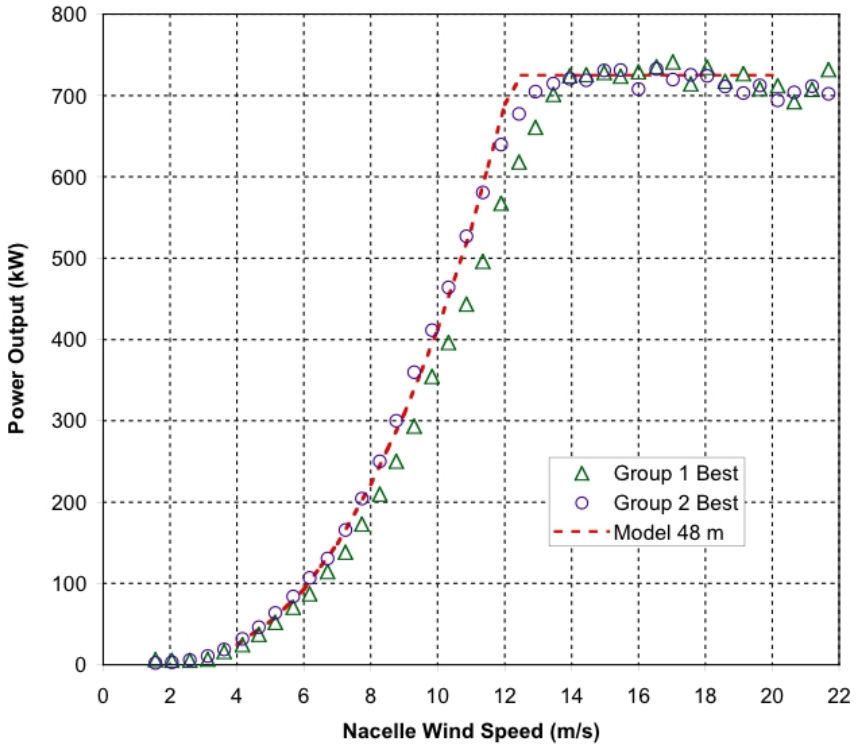

Figure 6.40 Best of group 1 and group 2 power output as a function of nacelle measured wind speed.

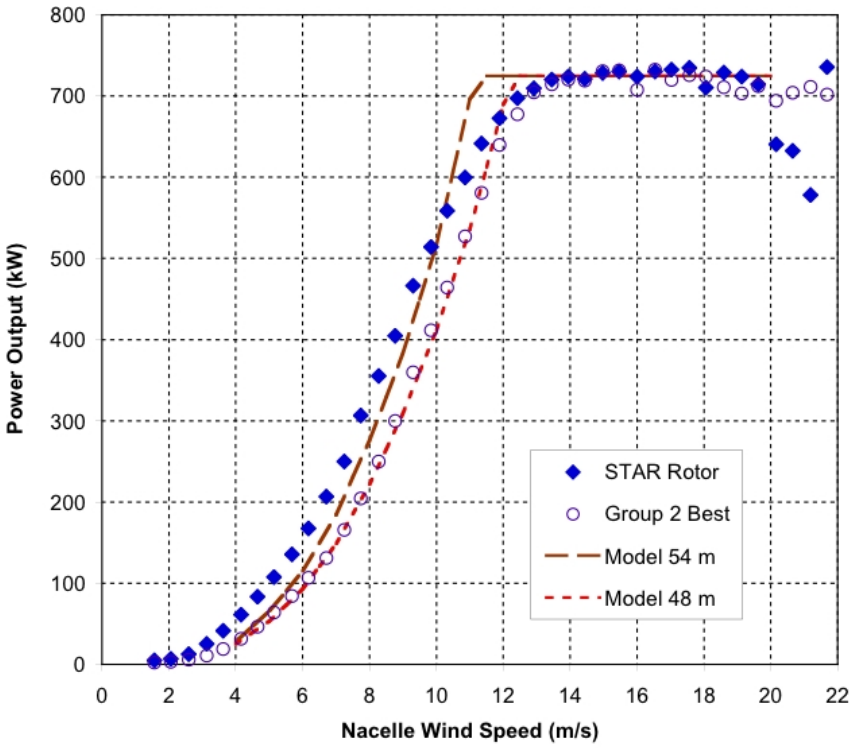

Figure 6.41 STAR and best of group 2 power output as a function of nacelle measured wind speed.

TURBINE-TO-TURBINE PERFORMANCE COMPARISON

A turbine-to-turbine performance comparison between the STAR 54 rotor and each of the turbines was completed using the same data set. This approach does not rely upon wind speed measurements, but instead uses other turbines as the performance reference. The STAR rotor power data was individually matched with the baseline turbines to verify that each had produced power during a given ten minute reference period. These two columns were sorted to eliminate data when one of the two turbines being compared was not producing power. The remaining data points were obtained when both turbines had positive power and were therefore considered to be "online."

The sorted online data were used to calculate the average energy capture for each of the groups over the online period, which is summarized in Table 6.10. Group 1 consisted of 3322 10 minute data points, when all five turbines (STAR 54 , RP-01, RP-02, RP-04, and RP-05) were all simultaneously producing power. Group 2 was based on 2524 data points, because RP-07 had a considerable period of missing data. The group analysis shows that energy capture for the STAR rotor was approximately 12% better than the Group 1 turbines and about 36% better than the Group 2 machines.

Table 6.10 Comparison in energy capture for Group 1 and Group 2 with turbines online.

Turbine Group 1	Energy (kWh)	Compare	Turbine Group 2	Energy (kWh)	Compare
RP-01	243009	101%	RP-05	144456	99%
RP-02	236301	99%	RP-06	145654	100%
RP-04	237148	99%	RP-07	146298	101%
RP-08	242496	101%			
Average	239738	100%	Average	145469	100%
STAR	268711	112%	STAR	197147	136%

For the turbine-to-turbine analysis the online power data from the STAR rotor was plotted against the online data for the comparison turbine If both turbines are performing equally well, the points should fall along the diagonal line. These data show that the STAR turbine performed better than all other turbines at the site. The average data for Group 1 and Group 2 were also evaluated in the same manner, under the requirement that all turbines in the group must be online. Figures 6.42 and 6.43 show that the STAR rotor has significantly improved performance as compared to each of the groups.

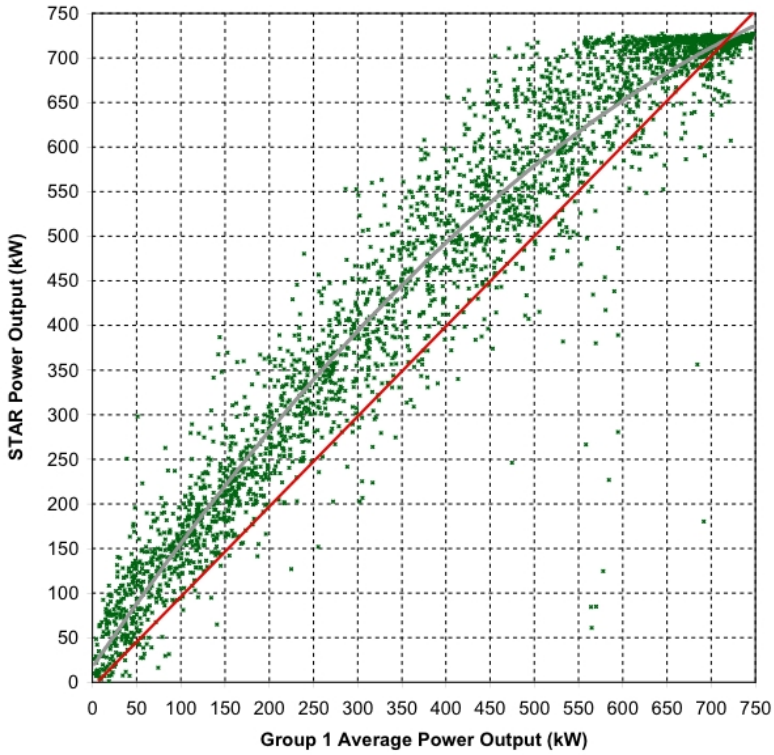

Figure 6.42 STAR 54 power output as compared to Group 1 power output with all turbines online.

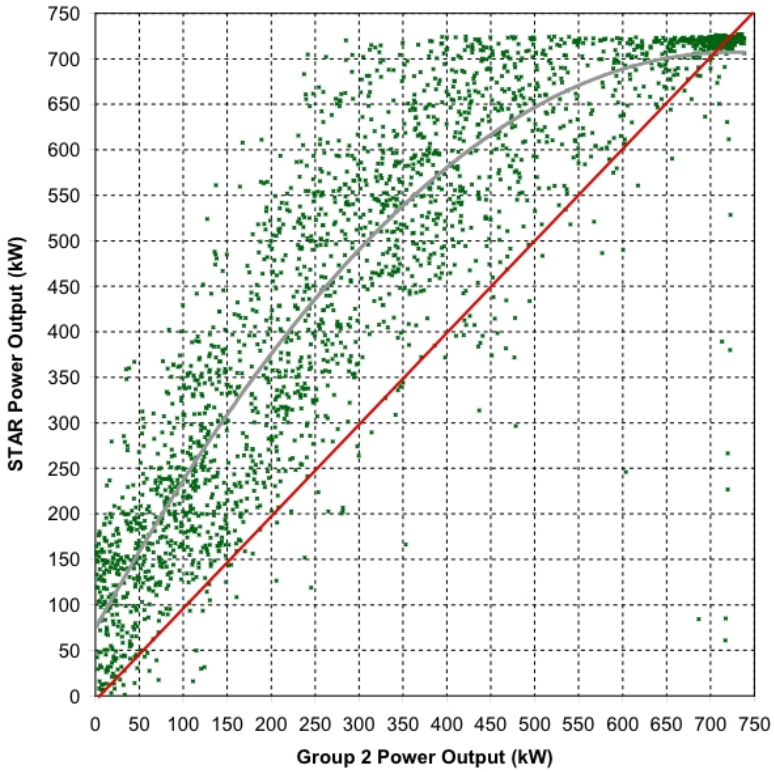

Figure 6.43 STAR 54 power output as compared to Group 2 power output with all turbines online.

FIELD DATA COLLECTION

Raw data from the test turbine was collected by technicians at the site. The data was stored in the DAS using a compact flash memory chip, which was periodically replaced by the test technician. The field staff uploaded the raw data to an internet based server from the test site. This data was then available on the web to the engineering staff, which downloaded the files for processing and evaluation. The raw data from the CF card was stored in a proprietary format. The first step in data processing was to convert the raw file into an ASCII text file. The text files were named according the following convention STAR-yyyy-mmdd-hhmm.dat.

The next step in data processing was to generate hourly voltage files. During this step the continuous 50 Hz data record was parsed into separate one (1) hour voltage files. These files are initially reviewed to identify sequences with slow rotations that can be used to calibrate the voltage signals into engineering units during the next step of data processing.

STRAIN GAGE CALIBRATION

The data records provided a voltage output in each of the two channels (edgewise and flatwise). Slow rotation data records were used to determine strain gage gain values (kNm/mV) using the known deadweight moment for the blade and measuring the change in output under the influence of gravity. Figure 6.44 provides an example data record consisting of slow rotations in light wind with the blades pitched to 60°, 45°, and 30°.

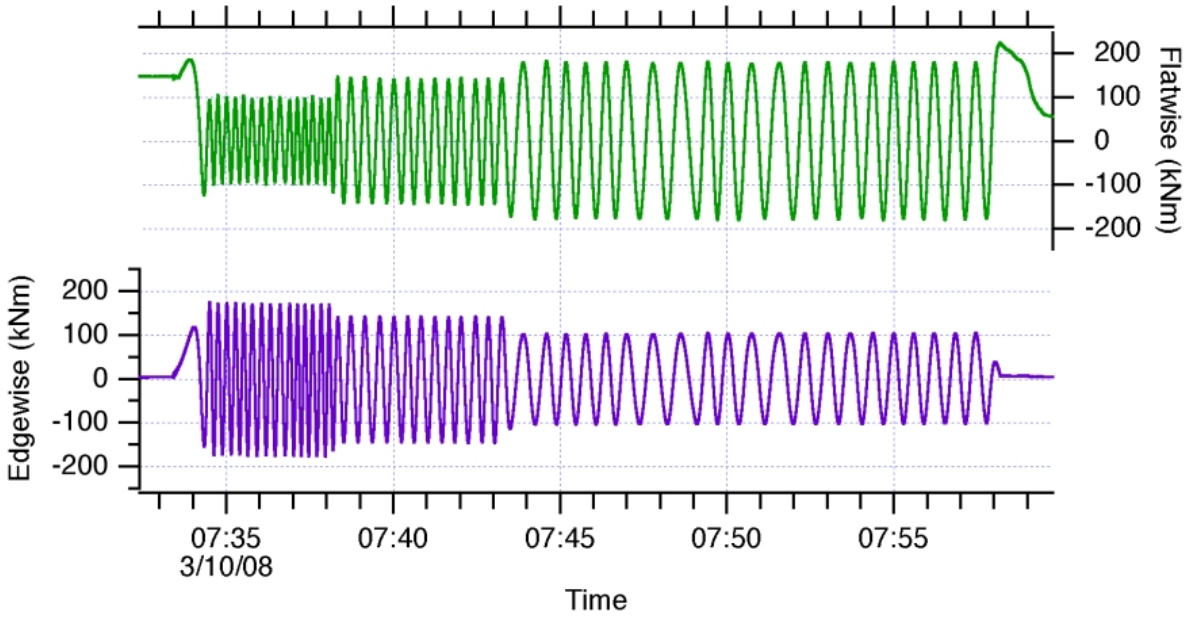

Figure 6.44 Slow rotation data at 60°, 45°, and 30° pitch from record STAR-2008-0310-0700.

The rotor root bending moment is referenced to the rotor center line (RCL). The magnitude of the sine wave produced by gravity during rotation is proportional to the known blade static moment times the sine or cosine of the pitch angle. The static moment of the instrumented test blade was 22,356 kg-m as referenced to the rotor center line. The strain gage gain and offset

values were calculated using a number of different records during the test period as shown in Table 6.11.

Table 6.11 Summary of calibrations used for the blade root strain gages.

Data Record	Strain Gage Channel	Pitch Command (deg)	2.0 Gage (deg)	Factor	Signal Gain No Factor (kNm/mV)	Signal Gain Factored (kNm/mV)	Range	Signal Offset (mV)	Signal Offset (kN-m)	
2008-0227-1800								-0.550	-398	
2008-0227-2100								-0.544	-394	
2008-0227-2200								-0.553	-401	
2008-0228-0100								-0.556	-403	
2008-0228-0200								-0.556	-403	
2008-0229-1000								-0.540	-391	
2008-0229-1100								-0.508	-368	
2008-0310-0700		30	28	0.883	825	728		-0.467	-339	
2008-0310-0700		45	43	0.731	998	730				
2008-0310-0700		60	58	0.530	1381	732				
2008-0413-0100		25	23	0.921	788	725	2.6%	-0.542	-393	
2008-0417-0000		25	23	0.921	793	730		-0.537	-389	
2008-0417-1700		25	23	0.921	775	713		-0.543	-393	
2008-0418-1000		25	23	0.921	778	716		-0.562	-407	
2008-0419-0100		25	23	0.921	789	726		-0.547	-396	
2008-0420-1400								-0.533	-386	
2008-0422-1300								-0.542	-393	
2008-0424-1200								-0.542	-393	
2008-0425-1000		25	23	0.921	783	721		-0.549	-398	
2008-0522-1400								-0.523	-379	
2008-0526-2100								-0.545	-395	
2008-0529-1800								-0.533	-387	
			2.0		Average	725		-0.539	-390	
2008-0227-1800	Flatwise							0.302	209	
2008-0227-2100								0.300	208	
2008-0227-2200								0.304	210	
2008-0228-0100								0.292	203	
2008-0228-0200								0.299	207	
2008-0229-1000		90	88	0.999	703	703		0.307	212	
2008-0229-1100		90	88	0.999	693	693		0.308	213	
2008-0310-0700		30	28	0.469	1493	701		0.268	186	
2008-0310-0700		45	43	0.682	1026	700				
2008-0310-0700		60	58	0.848	810	687				
2008-0413-0100		25	23	0.391	1808	706		0.303	210	
2008-0417-0000		25	23	0.391	1734	677		0.296	205	
2008-0417-1700		25	23	0.391	1750	684		0.364	252	
2008-0418-1000		25	23	0.391	1727	675		0.331	230	
2008-0419-0100		25	23	0.391	1793	701		0.292	202	
2008-0420-1400								0.293	203	
2008-0422-1300								0.290	201	
2008-0424-1200								0.305	212	
2008-0425-1000		25	23	0.391	1780	695		0.328	228	
2008-0522-1400								0.272	189	
2008-0526-2100								0.267	185	
2008-0529-1800								0.224	156	
					Average	693		0.297	206	

DATA SUMMARY REPORTS

The test data were obtained from three different DAS units, each with its own clock time. The individual clock times are accurate to within one minute. Three different types of data summary reports were prepared as outlined below. DAS #1 was located in the rotor hub and measured blade root strains at 50 Hz. There were 799 hours of strain gage measurements from DAS #1. An example of the Type 1 summary (data from DAS #1) is shown in Figure 6.45 below.

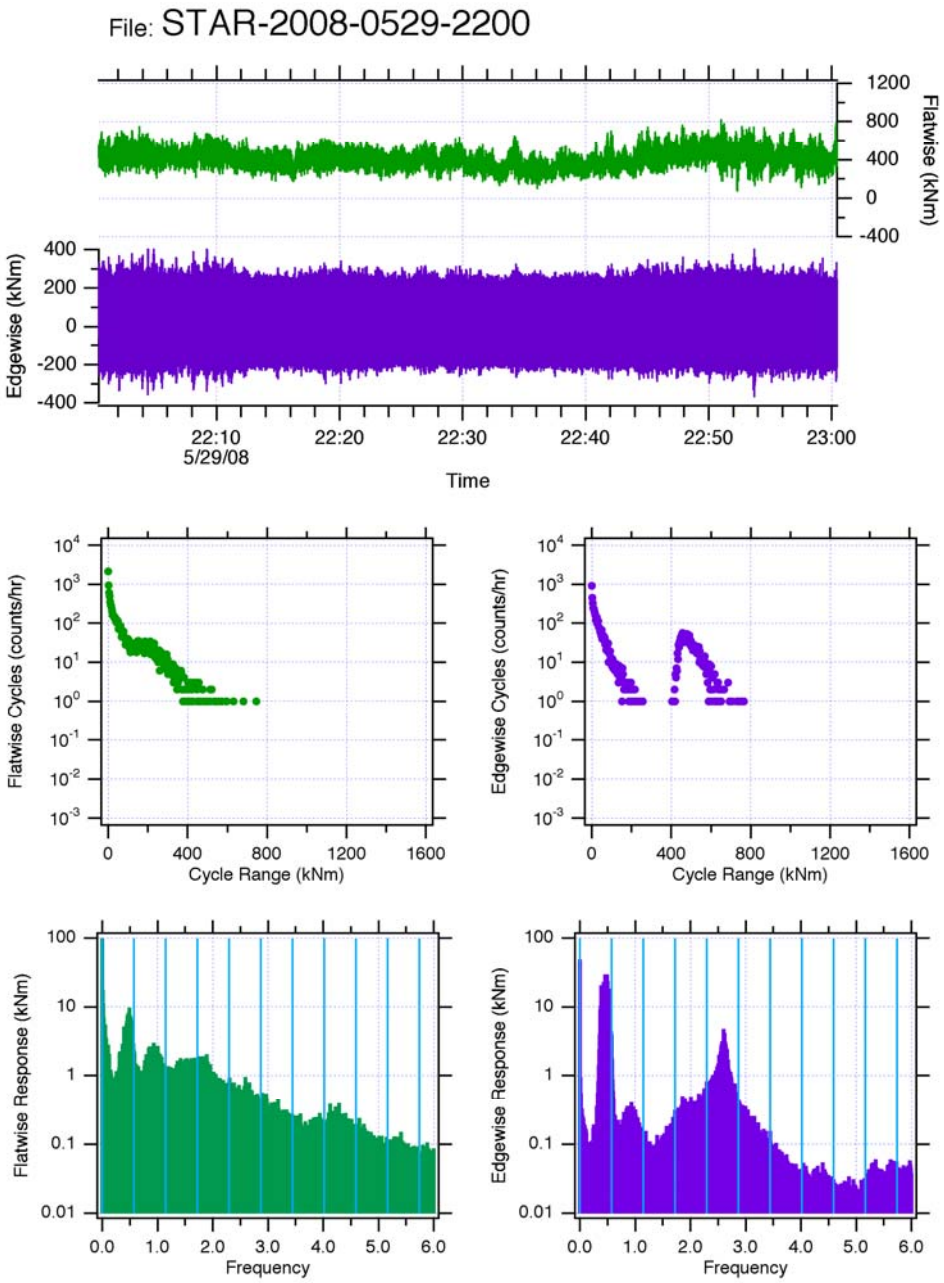

Figure 6.45 Example of a Type 1 summary file for data record STAR-2008-0529-2200.

DAS #2 was located at the tower base and recorded power output at 50 Hz. There were 407 hours with both DAS #1 and DAS #2 operated simultaneously. An example of the Type 2 summary (data from DAS #1 + DAS #2) is shown in Figure 6.46 below.

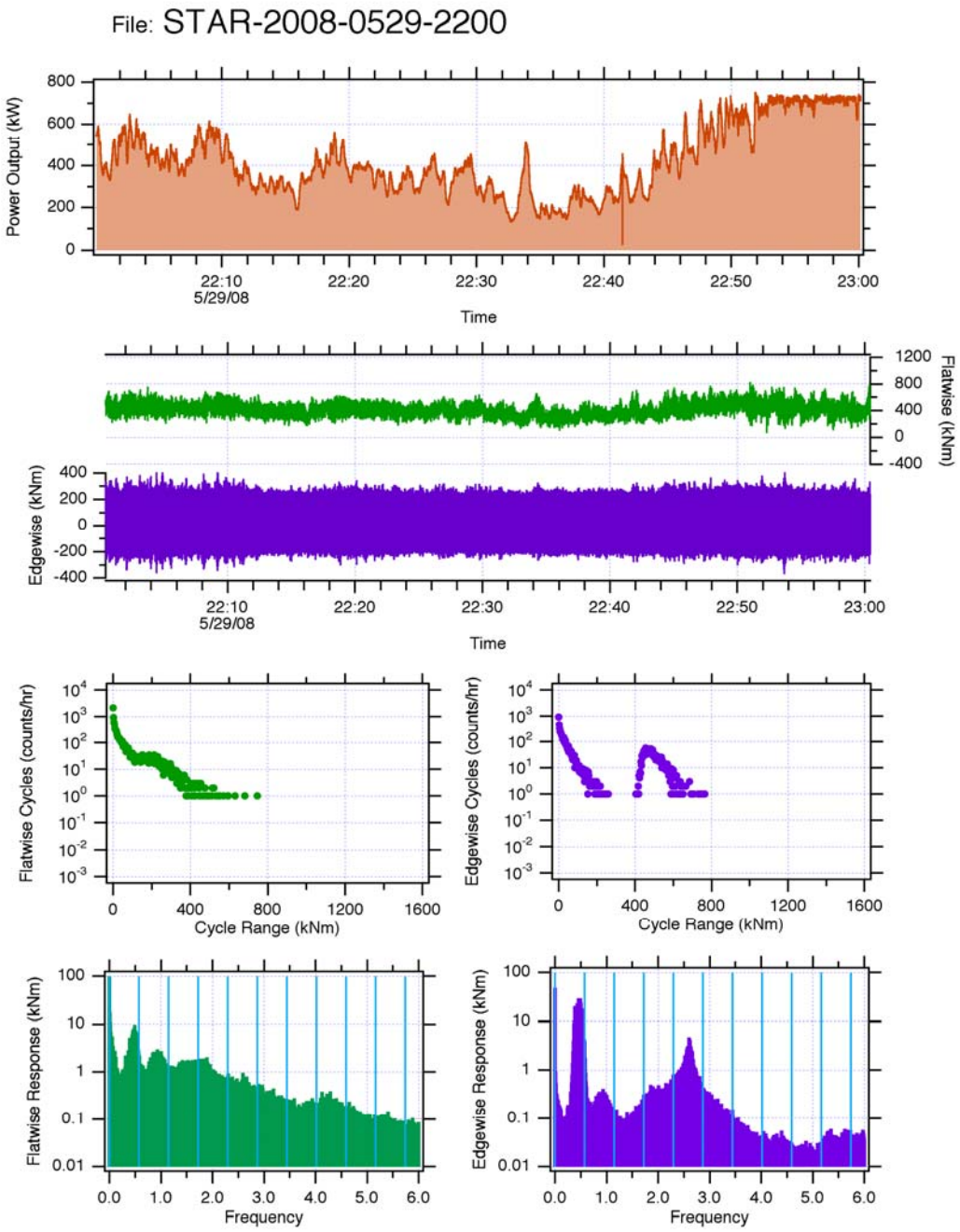

Figure 6.46 Example of a Type 2 summary file for data record STAR-2008-0529-2200.

DAS #3 was located in the nacelle and recorded wind speed, yaw error, and pitch angle at 2 Hz. There were 189 hours with all three DAS operational. These data provide operational detail regarding rotor speed and blade pitch angle that could not be obtained from the 10 minute average SCADA records. An example of the Type 3 summary (data from DAS #1 + DAS #2 + DAS #3) is shown in Figure 6.47 below using one (1) minute averages.

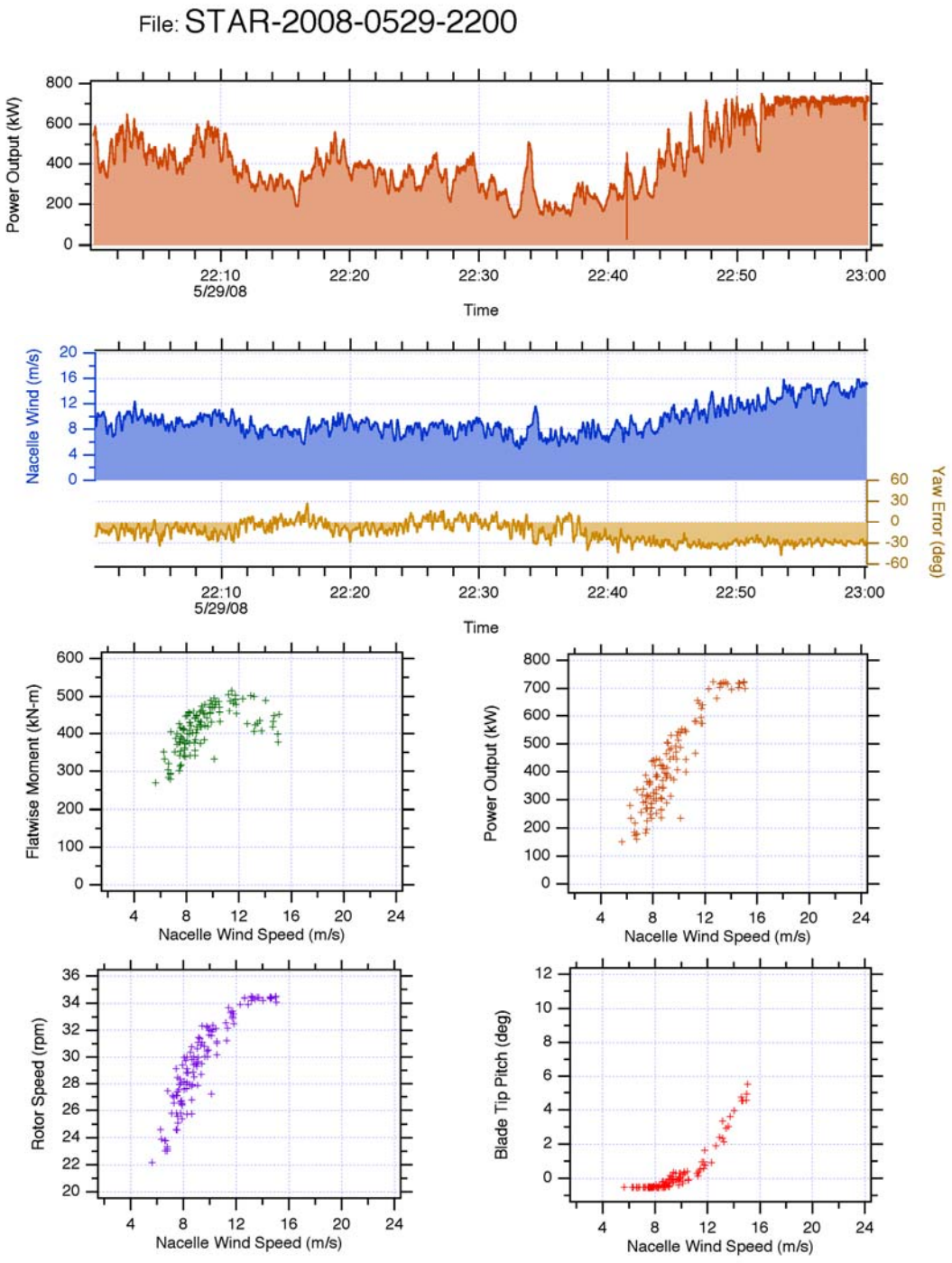

Figure 6.47 Example of a Type 3 summary file for data record STAR-2008-0529-2200.

FATIGUE SPECTRA

The blade root strain gage measurements were processed to determine the fatigue cycles using a rainflow algorithm. The cycle data were converted into counts per hour and an example graph is shown in Figure 6.48.

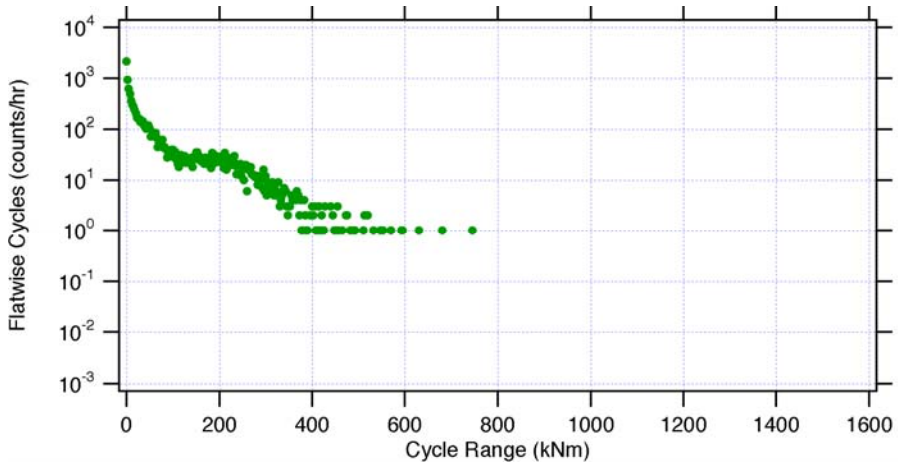

Figure 6.48 Blade flatwise fatigue cycles for data record STAR-2008-0529-2200.

FREQUENCY SPECTRA

The blade root test data were also used to evaluate the frequency response of the rotor during operation. The frequency response data were reviewed for potential resonance conditions that can occur if rotor frequencies coincide with an integral value of the rotational harmonics, as shown in Figure 6.49. The edgewise signal is poorly damped and is the mode of primary concern for resonance. A review of the STAR 54 operating data showed that the rotor edgewise frequency was well placed between the 4p and 5p harmonics.

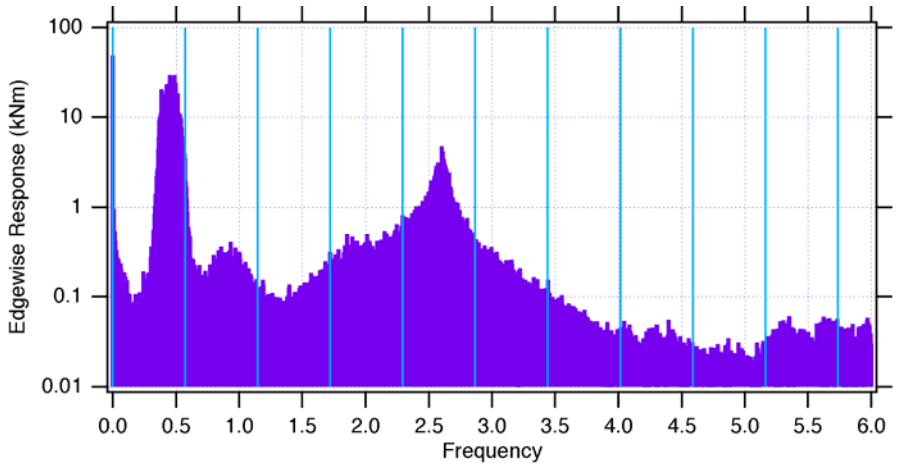

Figure 6.49 Blade edgewise frequency response for data record STAR-2008-0529-2200.

MEASURED LOADS COMPARED TO THE ADAMS MODEL

The measured blade loads at the blade root were compared to predictions from the ADAMS model for the STAR 54 rotor operating on a Z-48 turbine. The air density in the ADAMS model assumed an elevation of 5000 feet above sea level, which matched the turbine site altitude.

The Type 3 data records (DAS #1 + DAS #2 + DAS #3) were used to generate 10 minute statistics for wind speed, power output, and blade root loads. The binned data from 1128 records are summarized and compared against ADAMS predictions. The predicted flatwise loads were in good agreement with the ADAMS model predictions as shown in Figures 6.50 and 6.51. Mean flatwise loads were somewhat higher than predicted, but had similar characteristics. The maximum flatwise loads were somewhat lower than calculated by the ADAMS model.

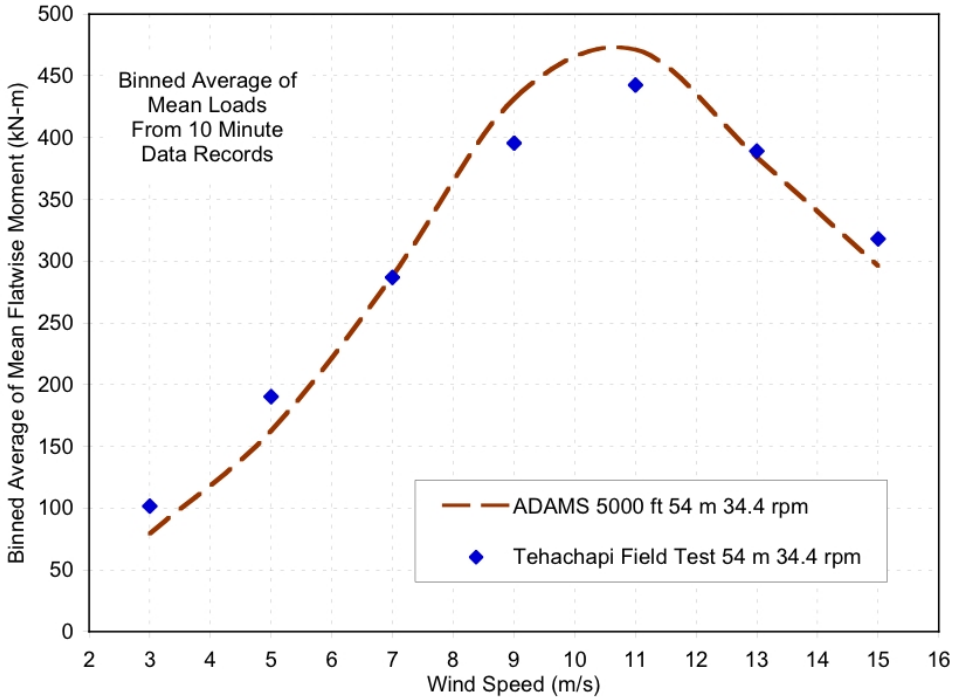

Figure 6.50 Comparison of measured binned average flatwise loads to the ADAMS model.

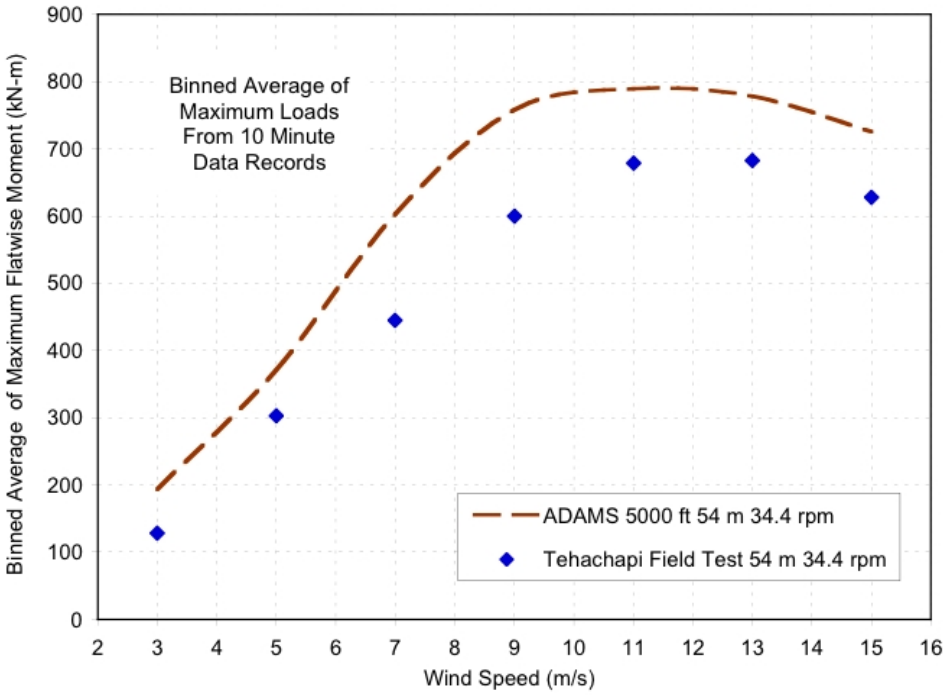

Figure 6.51 Comparison of measured binned maximum flatwise loads to the ADAMS model.

The measured mean edgewise loads were not in as good agreement with the ADAMS predictions. This is most likely due to strain gage thermal drift errors, which have a much increased impact on the relatively low mean edgewise loads. The maximum edgewise loads were somewhat higher than ADAMS calculations, which is probably due to somewhat less edgewise damping in the field as compared to the model.

7 REFERENCES

1. International Electrotechnical Commission, “Wind Turbine Generator Systems - Part 24: Lightning Protection for Wind Turbines”, IEC 88/128/CDV, November 2000.

2 . TPI Composites, “Cost Study for Large Wind Turbine Blades: WindPACT Blade System Design Studies,” Sandia National Laboratories, SAND 2003-1428, May 2003.

3. Althaus, D., *Niedriggeschwindigkeitsprofile*, Vieweg, Braunschweig, Germany, 1986

4. Drela, M., “Newton Solution of Coupled Viscous/Inviscid Multielement AirfoilFlows”, AIAA Paper 90-1470, June 1990.

5. Drela, M., “Integral Boundary Layer Formulation for Blunt Trailing Edges,” AIAA Paper 89-2166, 1989.

6. Brooks, T.F., and Marcolini, M.A., “Airfoil Tip Vortex Formation Noise,” AIAA Journal, Vol. 24, No. 2, Feb. 1986, pp. 246-252.

7. Wagner, S., Bareiß, and Guidati, G., *Wind Turbine Noise*, Springer, 1996.

8. Anon., “Fundamentals of Aeroacoustics with Applications to Wind Turbine Noise,” NREL Workshop, July 2001

9. Choudhari, M.M., et al, “Aeroacoustics Experiments in the Langley Low-Turbulence Pressure Tunnel,” NASA/TM-2002-211432, Feb. 2002.

10. Iida, M., Flieg, O., Arakawa, C., and Shimooka, M., “Wind Turbine Flow and Noise Prediction by Large Eddy Simulation,” AIAA Paper 2005-1188, Jan. 2005.

11. Malcolm, D. and Hansen, A, “WindPACT Turbine Rotor Design Study”, NREL/SR-500-32495, Revised April 2006, www.osti.gov/dublincore/ecd/servlets/purl/.../15000964.pdf.

12. Laird, D.L., Montoya, F.C., and Malcom, D.J., “Finite Element Modeling of Wind Turbine Blades”, American Institute of Aeronautics and Astronautics, AIAA 2005-195.

DISTRIBUTION:

Tom Acker
Northern Arizona University
PO Box 15600
Flagstaff, AZ 86011-5600

James Ahlgrimm c/o Cecelia Sterling
Office of Wind and Hydropower Technologies
EE-2B Forrestal Building, U.S. DOE
1000 Independence Ave. SW
Washington, DC 20585

Warren Ault
LM Glasfiber ND Inc.
117 N. Jefferson Street, Suite 400
Chicago, IL 60661

Ian Baring-Gould
NREL/NWTC
1617 Cole Boulevard MS 3811
Golden, CO 80401

Larry Barr
enXco
17298 West Commerce Way
Tracy, CA 95377

Benjamin Bell
Garrad Hassan America, Inc.
45 Main Street, Suite 302
Peterborough, NH 03458

Keith Bennett
U.S. Department of Energy
Golden Field Office
1617 Cole Boulevard
Golden, CO 80401-3393

Karl Bergey
University of Oklahoma
Aerospace Engineering Dept.
Norman, OK 73069

Mike Bergey
Bergey Wind Power Company
2200 Industrial Blvd.
Norman, OK 73069

Derek Berry
TPI Composites, Inc.
373 Market Street
Warren, RI 02885-0328

Gunjit Bir
NREL/NWTC
1617 Cole Boulevard MS 3811
Golden, CO 80401

Dan Brake
NextEra Energy
PO Box 14000
Juno Beach, FL 33408-0420

Marshall Buhl
NREL/NWTC
1617 Cole Boulevard MS 3811
Golden, CO 80401

C.P. Sandy Butterfield
NREL/NWTC
1617 Cole Boulevard MS 3811
Golden, CO 80401

Garrett Bywaters
Northern Power Systems
182 Mad River Park
Waitsfield, VT 05673

Doug Cairns
Montana State University
Department of Mechanical & Industrial Eng.
College of Engineering
Bozeman, MT 59717-3800

David Calley
Southwest Windpower
1801 West Route 66
Flagstaff, AZ 86001

Stan Calvert c/o Cecelia Sterling
Office of Wind and Hydropower Technologies
EE-2B Forrestal Building, U.S. DOE
1000 Independence Ave. SW
Washington , DC 20585

Larry Carr
NASA Ames Research Center
24285 Summerhill Ave.
Los Altos, CA 94024

Jamie Chapman
Texas Tech University
Wind Science & Engineering Research Center
Box 41023
Lubbock, TX 79409-1023

Joe Cohen
Princeton Economic Research, Inc.
1700 Rockville Pike, Suite 550
Rockville, MD 20852

C. Jito Coleman
Northern Power Systems
182 Mad River Park
Waitsfield, VT 05673

Ken J. Deering
The Wind Turbine Company
PO Box 40569
Bellevue, WA 98015-4569

James Dehlsen
Clipper Windpower Technology, Inc.
6305 Carpinteria Ave. Suite 300
Carpinteria, CA 93013

Frank Epps
EWT
20 Bow Street East
East Greenwich, RI 2818

S. Finn
GE Global Research
One Research Circle, Rm. K1-3C12A
Niskayuna, NY 12309

Peter Finnegan
GE Global Research
One Research Circle
Niskayuna, NY 12309

Trudy Forsyth
NREL/NWTC
1617 Cole Boulevard
Golden, CO 80401

Margaret M. Ganczak
Vestas Americas
1881 SW Naito Parkway, Suite 100
Portland, OR 97201

Brian Glenn
Clipper Windpower Technology, Inc.
6305 Carpinteria Ave. Suite 300
Carpinteria, CA 93013

Dayton Griffin
Global Energy Concepts, LLC
1809 7th Ave., Suite 900
Seattle, WA 98101

Jeffery Hammit
NextEra Energy
PO Box 14000
Juno Beach, FL 33408-0420

Maureen Hand
NREL/NWTC
1617 Cole Boulevard MS 3811
Golden, CO 80401

Ronald L. Harris c/o Cecelia Sterling
Office of Wind and Hydropower Technologies
EE-2B Forrestal Building, U.S. DOE
1000 Independence Ave. SW
Washington, DC 20585

Thomas Hermann
Odonata Research LLC
2813 Wild Plum Ct.
Columbia, MO 65201-3520

Mark A. Higgins c/o Cecelia Sterling
Office of Wind and Hydropower Technologies
EE-2B Forrestal Building, U.S. DOE
1000 Independence Ave. SW
Washington, DC 20585

D. Hodges
Georgia Institute of Technology
270 Ferst Drive
Atlanta, GA 30332

William E. Holley
GE Wind Energy
GTTC, M/D 100D
300 Garlington Rd.
Greenville, SC 29602-0648

Adam Holman
USDA - Agricultural Research Service
PO Drawer 10
Bushland, TX 79012-0010

D.M. Hoyt
NSE Composites
1101 N. Northlake Way, Suite 4
Seattle, WA 98103

Scott Hughes
NREL/NWTC
1617 Cole Boulevard MS 3911
Golden, CO 80401

Kevin Jackson (5)
Dynamic Design Engineering, Inc.
123 C Street
Davis, CA 95616

Jason Jonkman
NREL/NWTC
1617 Cole Boulevard
Golden, CO 80401

Dan Juhl
996 190th Avenue
WoodStock, MN 56186

Gary Kanaby (15)
Knight & Carver Wind Group
2423 Hoover Avenue
National City, CA 91950

Darren Kelly
Terra-Gen Power
565 Fifth Avenue, 29th Floor
New York , NY 10017

David Laino
Windward Engineering
8219 Glen Arbor Dr.
Rosedale, MD 21237-3379

Dean Landon
Terra-Gen Power
103 Oak Creek Road
Mojave, CA 93501

Scott Larwood
1120 N. Stockton St.
Stockton, CA 95203

Peter Levitt
Cal Wind Resources
2659 Townsgate Road Suite 122
Westlake Village, CA 91361-2738

Dennis H. Lin c/o Cecelia Sterling
Office of Wind and Hydropower Technologies
EE-2B Forrestal Building, U.S. DOE
1000 Independence Ave. SW
Washington, DC 20585

Wendy Lin
GE Global Research
One Research Circle
Niskayuna, NY 12309

Steven P. Lindenberg c/o Cecelia Sterling
Office of Wind and Hydropower Technologies
EE-2B Forrestal Building, U.S. DOE
1000 Independence Ave. SW
Washington, DC 20585

Steve Lockard
TPI Composites, Inc.
8501 N. Scottsdale Rd.
Scottsdale, AZ 85253

James Locke
AIRBUS North America Engineering, Inc.
213 Mead Street
Wichita, KS 67202

Bruce Maderos
NextEra Energy
6700 Birds Landing Road
Birds Landing, CA 94512

David Malcolm
Global Energy Concepts, LLC
1809 7th Ave., Suite 900
Seattle, WA 98101

John F. Mandell
Montana State University
302 Cableigh Hall
Bozeman, MT 59717

Megan S. McCluer c/o Cecelia Sterling
Office of Wind and Hydropower Technologies
EE-2B Forrestal Building, U.S. DOE
1000 Independence Ave. SW
Washington, DC 20585

Tim McCoy
Kamzin Technology, Inc.
425 Pontius Ave. N., Suite 150
Seattle, WA 98109

L. McKittrick
Montana State University
Department of Mechanical & Industrial Eng.
220 Roberts Hall
Bozeman, MT 59717

Steve Mikel
Suzlon Wind Energy Corporation
620 3rd Avenue SE
Pipestone, MN 56164

Amir Mikhail
Clipper Windpower Technology, Inc.
6305 Carpinteria Ave. Suite 300
Carpinteria, CA 93013

Francisco Alejandro Moreno c/o Cecelia Sterling
Office of Wind and Hydropower Technologies
EE-2B Forrestal Building, U.S. DOE
1000 Independence Ave. SW
Washington, DC 20585

Patrick Moriarty
NREL/NWTC
1617 Cole Boulevard
Golden, CO 80401

Walt Musial
NREL/NWTC
1617 Cole Boulevard MS 3811
Golden, CO 80401

Library (5) NWTC
NREL/NWTC
1617 Cole Boulevard
Golden, CO 80401

Byron Neal
USDA - Agricultural Research Service
PO Drawer 10
Bushland, TX 79012

Steve Nolet
TPI Composites, Inc.
373 Market Street
Warren, RI 02885-0367

Gerard C. Nostra
NextEra Energy
PO Box 14000
Juno Beach, FL 33408-0420

Energy Research Centre of the Netherlands
T.S. Obdam
PO Box 1
1755 ZG Petten
The Netherlands

Richard Osgood
NREL/NWTC
1617 Cole Boulevard
Golden, CO 80401

Tim Olsen
Tim Olsen Consulting
1428 S. Humboldt St.
Denver, CO 80210

Randy Parry
Rural Learning Center
109 North Main Street
Howard, SD 57349

Robert Z. Poore
Global Energy Concepts, LLC
1809 7th Ave., Suite 900
Seattle, WA 98101

Pep Prats
Ecotecnia
Roc Boronat 78
Barcelona
Spain

Robert Preus
Abundant Renewable Energy
22700 NE Mountain Top Road
Newberg, OR 97132

Ian Prowell
University of California-San Diego
9500 Gilman Drive #0085
San Diego, CA 92093-0085

Mike Reed
Inspired Systems
309 West Pasadena Road
Millersville, MD 21108

Jim Richmond
MDEC
3368 Mountain Trail Ave.
Newberg Park, CA 91320

Michael Robinson
NREL/NWTC
1617 Cole Boulevard
Golden, CO 80401

Paul Roeder
Wind Vision, LLC.
401 8th Street SW
Waukon, IA 52172

Dan Samborsky
Montana State University
302 Cableigh Hall
Bozeman, MT 59717

Dan Sanchez
U.S. Department of Energy
NNSA/SSO
PO Box 5400 MS 0184
Albuquerque, NM 87185-0184

Scott Schreck
NREL/NWTC
1617 Cole Boulevard MS 3811
Golden, CO 80401

David Simms
NREL/NWTC
1617 Cole Boulevard MS 3811
Golden, CO 80401

Brian Smith
NREL/NWTC
1617 Cole Boulevard MS 3811
Golden, CO 80401

J. Sommer
Molded Fieber Glass Companies/West
9400 Holly Road
Adelanto, CA 92301

Ken Starcher
Alternative Energy Institute
West Texas A & M University
Canyon, TX 79016

Cecelia M. Sterling (2)
Office of Wind and Hydropower Technologies
EE-2B Forrestal Building, U.S. DOE
1000 Independence Ave. SW
Washington, DC 20585

Fred Stoll
Webcore Technologies, Inc.
8821 Washington Church Rd.
Miamisburg, OH 45342

Herbert J. Sutherland
HJS Consulting
1700 Camino Gusto NW
Albuquerque, NM 87107-2615

Andrew Swift
Texas Tech University
Wind Science & Engineering Research Center
PO Box 41023
Lubbock, TX 79409-1023

Robert W. Thresher
NREL/NWTC
1617 Cole Boulevard MS 3811
Golden, CO 80401

Neil Mac Tiernan
NordicWindpower
125 University Avenue
Berkeley, CA 94710

Hendrick Tolstrep
enXco
63-665 19th Ave
North Palm Springs, CA 92258

Steve Tsai
Stanford University
Aeronautics & Astronautics
Durand Bldg. Room 381
Stanford, CA 94305-4035

Case P. van Dam (5)
Dept. of Mechanical & Aeronautical Eng.
University of California, Davis
One Shields Avenue
Davis, CA 95616-5294

Jeroen van Dam
Windward Engineering
NREL/NWTC
1617 Cole Boulevard
Golden, CO 80401

Brian Vick
USDA - Agricultural Research Service
PO Drawer 10
Bushland, TX 79012

Carl Weinberg
Weinberg & Associates
42 Green Oaks Court
Walnut Creek, CA 94596-5808

Kyle Wetzel
Wetzel Engineering, Inc.
PO Box 4153
Lawrence, KS 66046-1153

Jim Winsayer
Continental Windpower
402 East Gutierrez #170
Santa Barbara, CA 93101

David M. Wright
168 Thompson Street
Springfield, MA 1109

Mike Zuteck (5)
MDZ Consulting
601 Clear Lake Road
Clear Lake Shores, TX 77565

INTERNAL DISTRIBUTION:

MS 0346 T.J. Baca, 1523
MS 0372 J.M. Redmond, 1525
MS 0557 T.W. Simmermacher, 1523
MS 0557 D.T. Griffith, 1523
MS 1124 J.R. Zayas, 6333
MS 1124 T.D. Ashwill, 6333 (20)
MS 1124 M. Barone, 6333
MS 1124 D.E. Berg, 6333
MS 1124 J. Berg, 6333
S.M. Gershin, 6333 (Electronic)
MS 1124 R.R. Hill, 6333
MS 1124 R. Jepsen, 6333
MS 1124 W. Johnson, 6333
MS 1124 B. Karlson, 6333
MS 1124 D.L. Laird, 6333
MS 1124 B. Lucero, 6333
MS 1124 B. McKenney, 6333
MS 1124 A. Ogilvie, 6333
MS 1124 J. Paquette, 6333
MS 1188 V. Peters, 6345
MS 1124 B. Resor, 6333
MS 1124 J. Roberts, 6333
MS 1124 M.A. Rumsey, 6333
MS 1124 P.S. Veers, 6333
MS 1124 J. White, 6333
MS 1108 D. Wilson, 6333
Technical Library, 9536 (Electronic)
MS 1124 Wind Library, 6333 (20)